Integrated modelling of tokamak core and edge plasma turbulence

Jarrod Brooks Leddy

Doctor of Philosophy

UNIVERSITY OF YORK

PHYSICS

January 2016

"It is not in the nature of things for any one man to make a sudden violent discovery; science goes step by step, and every man depends on the work of his predecessors. When you hear of a sudden unexpected discovery - a bolt from the blue, as it were - you can always be sure that it has grown up by the influence of one man or another, and it is this mutual influence which makes the enormous possibility of scientific advance. Scientists are not dependent on the ideas of a single man, but on the combined wisdom of thousands of men, all thinking of the same problem, and each doing his little bit to add to the great structure of knowledge which is gradually being erected."

Ernest Rutherford as quoted in *The Birth of a New Physics*

Abstract

The accurate prediction of turbulent transport and its effect on tokamak operation is vital for the performance and development of operational scenarios for present and future fusion devices. For problems of this complexity, a common approach is integrated modelling where multiple, well-benchmarked codes are coupled together to form a code that covers a larger domain and range of physics than each of the constituents. The main goal of this work is to develop such a code that integrates core and edge physics for long-time simulation of the tokamak plasma. Three questions are addressed that contribute to the ultimate end goal of this core/edge coupling, each of which spans a chapter. Firstly, the choice of model for edge and core must be fluid for the time scales of interest, but the validity of a common further simplification to the physics models (i.e. the drift-reduction) is explored for regions of interest within a tokamak. Secondly, maintaining a high computational efficiency in such integrated frameworks is challenging, and increasing this while maintaining accurate simulations is important. The use of sub-grid dissipation models is ubiquitous and useful, so the accuracy of such models is explored. Thirdly, the challenging geometry of a tokamak necessitates the use of a field-aligned coordinate system in the edge plasma, which has limitations. A new coordinate system is developed and tested to improve upon the standard system and remove some of its constraints. Finally, the investigation of these topics culminates in the coupling of an edge and core code (BOUT++ and CENTORI, respectively) to produce a novel, three-dimensional, two-fluid plasma turbulence simulation.

Contents

List of Tables

List of Figures

Acknowledgements

Thanks to my wife Gaby, who was as excited as me about an adventure to England for PhD research. She has supported me unwaveringly throughout the entire process. Thanks to my family who supported and encouraged our move abroad. Thanks to my friends, who gave relief to my stress with board games and beer. Thanks to my cat, Fiddle, who kept me sane with cuddles. Finally, thanks to Ben Dudson and Michele Romanelli, my supervisors, for guiding me and fostering my growth as an independent researcher.

Declaration

I declare that the work presented in this thesis, except where it is otherwise stated, is based on my own research and has not been submitted previously for a degree in this or any other university. Parts of the work presented in this thesis have been published in:

- Chapter 3 in [1] Leddy, J *et al* (2015) *Plasma Physics and Controlled Fusion* **57**(12):125016

- Chapter 5 in preparation to submit. [post-viva note: now submitted to *Computer Physics Communications* (April 2016)]

Parts of this work have also been presented as a combination of posters and orals at the following conferences:

- Chapter 4 presented as a poster at European Fusion Theory Conference (2013)

- Chapter 3 presented orally at American Physical Society Division of Plasma Physics conference (2014)

- Chapters 5 and 6 presented as a poster at American Physical Society Division of Plasma Physics conference (2015)

Chapter 1

Introduction

Fossil fuels are currently the world's leading source of energy, providing nearly 80% of the total energy used each year [2]. Unfortunately, these fuels are also a large source of pollution and are limited in supply with much of that supply coming from very specific locations - a source of political conflict [3]. In order to meet the goals of legislation created to stabilise the concentration of greenhouse gases, clean energy sources must make-up a minimum of 40% of the world market by 2035 [4]. Figure 1.1 shows the

World consumption
Million tonnes oil equivalent
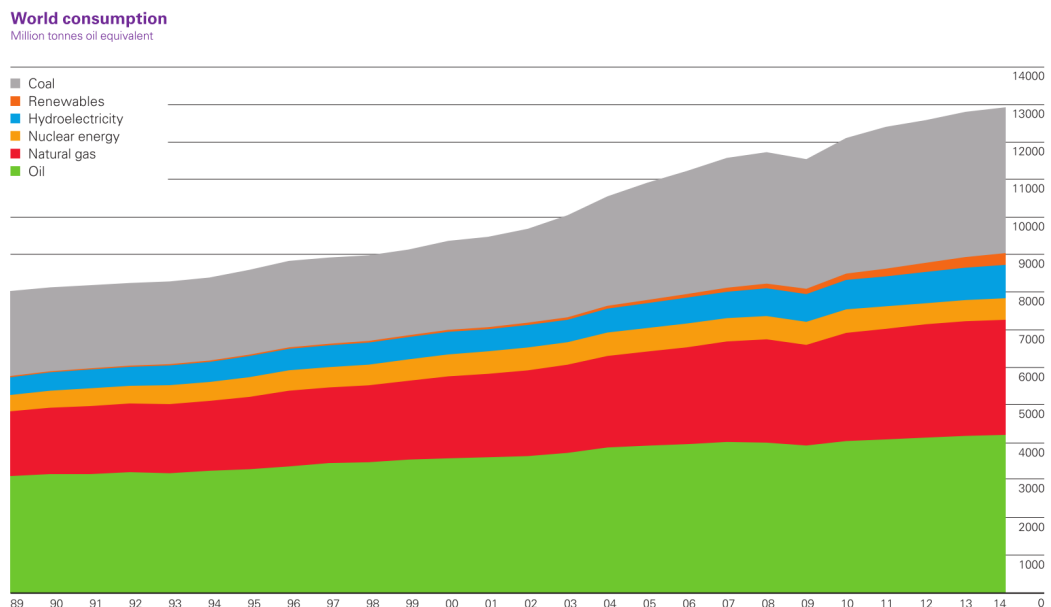
Figure 1.1: The yearly worldwide energy consumption by type in millions of tons of oil equivalent from 1989-2014 according to the British Petroleum statistical report in 2015 [5].

yearly world consumption of various forms of energy in millions of tons of equivalent oil, demonstrating the huge disparity between fossil fuels and clean energy [5]. Coal, oil, and natural gas provide the dominant source for energy in the world, and are steadily growing. Providing only a small percentage are renewable sources, and though they

are growing, it is not at a fast enough rate, nor can they fully supply the required amount of energy across the world [3]. This, in combination with the rising population that is expected to reach 10 billion by 2060 [6], threatens to deplete fossil fuel reserves. Fission as well as renewable energy sources, such as wind and solar, are intending to fill this gap, but a more reliable and cleaner source of energy must be realised in the development of fusion power plants.

Fusion energy does not suffer from many of the problems of fossil fuels - it is clean, renewable, and safe. Unlike nuclear fission, there are no inherent radioactive by-products, only neutrons and helium. High energy neutrons can activate the walls and structure of the reactor, but careful design can mean only a small amount of short-lived nuclear waste (on the order of 10^2 years). The fuel for fusion, tritium, is also radioactive (with a very short half-life of 12.3 years), but the vast majority of it will be used during the lifetime of a reactor so it should not remain upon decommissioning and any that does can be extracted and used in another reactor. Fusion can also provide steady-state energy production unlike many renewable energy sources such as solar and wind [2], which are intermittent and very dependent upon location.

1.1 Fusion power

Fusion generates energy through the nuclear process of combining two smaller atoms into a larger one. The rest mass of the final products are smaller than that of the combined constituents, and this mass deficiency provides a release of energy according to Einstein's famous equation $E = mc^2$ [7]. There are many nuclei that will undergo fusion, but the cross-sections of these reactions, shown in figure 1.2, indicate that D-T (deuterium-tritium) is clearly the easiest reaction to obtain due to the high peak cross-section at a relatively low temperature. The D-T reaction results in the production of a 3.5MeV helium atom and a 14.1MeV neutron [9]:

$$\ _1^2\mathrm{D} + \ _1^3\mathrm{T} \rightarrow \ _2^4\mathrm{He} + \ _0^1\mathrm{n}. \tag{1.1}$$
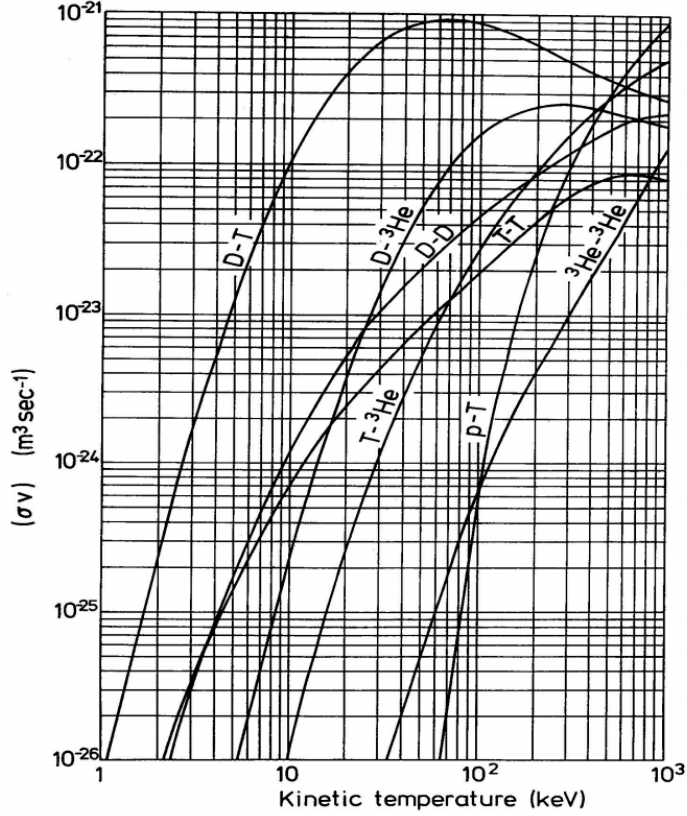
Figure 1.2: The cross-section for various fusion reactions as a function of temperature [8].

The energy released from the fusion reaction can then be harvested through heating a fluid (most likely water) and then using a turbine like with fossil fuels. Though deuterium is very abundant on Earth (1/6400 H_2O molecules contains deuterium) [10], the same cannot be said for tritium, which has a half-life of only 12.3 years. It will be necessary for fusion reactors to breed their own tritium using a lithium breeding blanket to optimise tritium creation through the three following reactions:

$$^9_4\text{Be} + \text{n} \rightarrow 2\left(^4_2\text{He}\right) + 2\text{n}, \tag{1.2a}$$

$$\text{n} +^7_3\text{Li} \rightarrow \text{T} +^3_2\text{He} + \text{n}, \tag{1.2b}$$

$$\text{n} +^6_3\text{Li} \rightarrow \text{T} +^4_2\text{He}. \tag{1.2c}$$

Reaction 1.2a is used to multiply incident neutrons to increase the breeding fraction, which is the amount of Tritium bred per neutron created in the fusion reaction. Reactions 1.2b requires a high-energy incident neutron and releases tritium and a low energy neutron. This low energy neutron can then react with lithium-6 as in reaction 1.2c to also release a tritium atom. Plans for a breeder blanket system [11] have been devised and will be tested in ITER, the next generation tokamak test reactor [12].

1.2   Approaches to fusion

The fusion reaction in equation 1.1 requires the initial deuterium and tritium to be at very high energies equivalent to 100-150 million Kelvin. A gas raised to these temperatures becomes fully ionised resulting in a plasma, which then must be confined to keep the temperature high. In stars this confinement is provided by gravity, but on Earth this must be accomplished using more efficient and scalable methods. Inertial and magnetic are currently the two leading approaches to that confinement, of which magnetic confinement is the most developed.

1.2.1   Inertial confinement fusion

Inertial confinement fusion (ICF) is theoretically achieved by compressing the D-T fuel pellet to densities and temperatures required for fusion to occur. Once the fusion reactions begins in the centre of the pellet, the energetic alpha particles generated are reabsorbed to provide more heating which generates a self-sustaining burn-wave propagating from the centre to the edge of the fuel. At the same time, the edge of the fuel is ablating away with a rarefaction wave propagating inwards. The confinement time for the plasma is then the time from the initial fusion until these two wave fronts meet and the requisite densities and temperatures are lost [13].

Within inertial confinement fusion there are two mainstream approaches - direct and indirect drive. Direct drive involves the lasers directly heating the fuel pellet. This has the advantage of efficiency in laser to pellet energy transfer. The other method, indirect drive, places the fuel pellet inside a hohlraum, or high-Z material case that absorbs the laser energy and re-emits high-energy photons which are then absorbed by the fuel. The advantage of this method over direct drive is that it heats the fuel very evenly, reducing instabilities like Rayleigh-Taylor. Unfortunately, this method reduces the efficiency of laser-fuel coupling and the high-Z material of the hohlraum can be activated by the fusion neutrons.

The largest facility in the world attempting ICF is the National Ignition Facility (NIF) at Lawrence Livermore National Labs (LLNL) in the USA, and the experiments are

wholly based on indirect drive as it is thought to be the most likely to initially succeed [14]. Recent progress has been made where more energy has been released from the fuel capsule than was absorbed, meaning a net gain in energy [15]. However, due to the inefficiencies in both laser-capsule coupling and in the laser itself, fusion energy output must still be increased by multiple orders of magnitude to achieve overall net energy gain.

1.2.2   Magnetic confinement fusion

Magnetic confinement fusion (MCF) is a method of using magnetic fields to confine a plasma by taking advantage of the fact that charged particles experience a force when moving near magnetic field lines according to

$$\frac{\partial \vec{v}}{\partial t} = \frac{q}{m} \left(\vec{E} + \vec{v} \times \vec{B} \right) \tag{1.3}$$

where $\vec{v}$ is the velocity vector, $\vec{E}$ is the electric field, $\vec{B}$ is the magnetic field, q is the particle charge, and m is the particle mass. Particles governed by this equation gyrate in a helical motion around magnetic field lines with a radius of ρ_i, called the Larmor radius. Parallel motion is unaffected by the magnetic field. The electric field has a more complex impact on the motion due to drifts, and will be discussed in section 1.3.3.1.

MCF was first attempted using cylindrical magnetic mirrors, which implement a high magnetic field on either end of the cylinder with a low field in the center [16]. This field orientation creates a point of reflection on either end for a subset of the particles with low enough parallel velocity ($v_\parallel$), confining them in the cylinder. This, theoretically, means an initial loss of particles with large $v_\parallel$, but should confine the rest. Unfortunately, even particles with low $v_\parallel$ undergo collisions that re-establish a Maxwellian velocity distribution, ultimately giving them a high enough $v_\parallel$ to escape out the ends of the magnetic mirror. The confinement of this device degrades over a very short period of time, so other approaches had to be developed.

By wrapping the cylinder into a torus, particles that would have previously escaped

would simply be injected back into the other side of the mirror - this is how the tokamak was first envisioned, though now it has changed significantly [17]. A tokamak is a toroidal plasma confinement device that uses magnetic fields to confine the charge particles of the plasma through Lorentz forces, as in equation 1.3, which constrains their motion perpendicular to the field but allows nearly free flowing plasma along the field. These magnetic fields are created using a series of toroidal field coils (like a cylindrical solenoid wrapped into a torus). Due to particle drifts within a tokamak, a toroidal field is not enough to confine the plasma [18]. It is necessary to have a poloidal field as well (discussed in section 1.3.3.1), which is created by driving a toroidal current through the plasma with a central solenoid. Other means of driving this current are also in development and use such as electron cyclotron current drive (ECCD), lower hybrid current drive (LHCD), radio frequency (RF) current drive, and even the bootstrap current in advanced tokamak operational regimes [19]. Figure 1.3 shows the helical twist of the magnetic field that is used to confine the plasma.
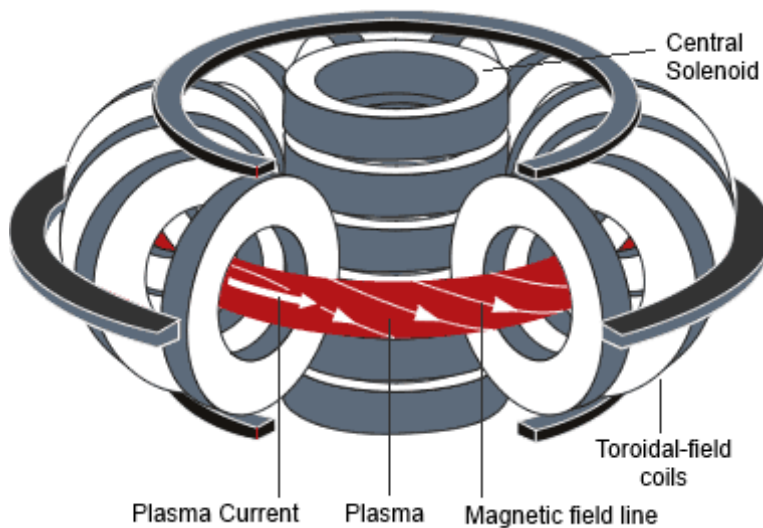
Figure 1.3: Basic schematic of a tokamak - a toroidal plasma confinement device. The field lines wind helically around the device, generated partly by the toroidal field coils and partly by the central solenoid driving a current through the plasma [20].

It is practical to define a new coordinate system (ψ, θ, ϕ) for use in tokamak geometry. This is similar to normal toroidal coordinates, except the radial coordinate is replaced with ψ, the poloidal magnetic flux, as illustrated in figure 1.4. This is especially useful when the plasma is shaped (ie. the poloidal cross-section is not circular).
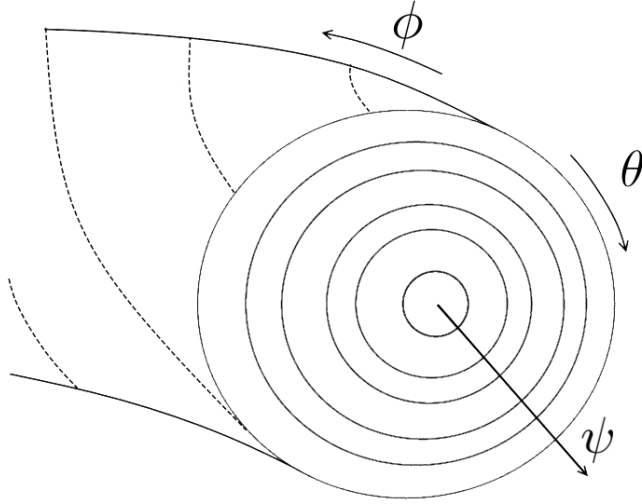
Figure 1.4: This schematic shows the standard tokamak flux coordinates (ψ, θ, ϕ). The flux coordinate, ψ, indicates the flux surface and is similar to a minor radial coordinate. The poloidal and toroidal coordinates, θ and ϕ respectively, indicate position along the surface of the torus.

1.3 MCF plasma theory

The field of plasma physics theory is extensive, so only the most relevant topics are discussed in this section. There is a focus on treating plasma as a fluid for simulation and analytic understanding, as well as a discussion of the perpendicular (to the magnetic field) transport of energy and particles and its effect on plasma confinement and tokamak performance.

1.3.1 Plasma as a fluid

The full accurate description of a plasma is kinetic, following the position and velocity of each particle using the Klimontovich equation [21]. This is often reduced to include only pair collisions resulting in the Vlasov-Fokker-Planck (VFP) equation [22], based on equation 1.3, written as

$$\frac{\partial f}{\partial t} + \vec{v} \cdot \nabla f + \frac{e_j}{m_j} \left(\vec{E} + \vec{v} \times \vec{B} \right) \cdot \frac{\partial f}{\partial \vec{v}} = \left(\frac{\partial f}{\partial t} \right)_c \tag{1.4}$$

where f is the 7-D particle distribution function $f(x, y, z, v_x, v_y, v_z, t)$, the subscript j indicates the species, and $\left(\frac{\partial f}{\partial t} \right)_c$ is the collision operator that can be calculated based on multiple small angle collisions, called Coulomb collisions [23]. Evolving this model via simulation requires tracking the 7-dimensional distribution function, which is very computationally expensive. It is for this reason that the plasma is often treated as a

fluid, and the moments of this kinetic equation are taken to describe its behaviour [24]. Similar to the non-plasma fluid description, the moments are never a closed system, as one more moment is always required for closure. So to close the system, an equation of state or some other form of closure must be utilised [25]. The plasma fluid equations are similar to the Navier-Stokes equations but also include $\vec{E} \times \vec{B}$ behaviour, which dominates plasma motion perpendicular to the magnetic field. Fluid models have an implicit assumption that the Larmor radius is small and the ion cyclotron frequency is the largest frequency in the system. The first moment of the VFP is the continuity equation [24]

$$\frac{\partial n}{\partial t} = -\vec{\nabla} \cdot (n\vec{v}) \tag{1.5}$$

which describes the conservation of density, n, for a fluid moving at some velocity, $\vec{v}$. The time derivative here is actually a convective derivative defined as $\frac{\mathrm{d}}{\mathrm{d}t} = \frac{\partial}{\partial t} + \vec{v} \cdot \nabla$, which has contributions both from a field changing in time and also varying in space while moving. The second moment gives the momentum equation

$$m_j n_j \frac{\mathrm{d}\vec{v}_j}{\mathrm{d}t} + \nabla p_j + \vec{\nabla} \cdot \boldsymbol{\pi}_s - e_j n_j \left(\vec{E} + \vec{v}_j \times \vec{B}\right) = \vec{F}_j \tag{1.6}$$

where p is the pressure, $\boldsymbol{\pi}_s$ is the viscous stress tensor, and $\vec{F}$ describes the forces between each species within the plasma. The third moment of the VFP equation is the energy equation given by

$$\frac{3}{2}\frac{\mathrm{d}p_j}{\mathrm{d}t} + \frac{5}{2}p_j\vec{\nabla} \cdot \vec{v}_j + \boldsymbol{\pi}_s : \nabla\vec{v}_j + \vec{\nabla} \cdot \vec{q}_j = W_j \tag{1.7}$$

where $\boldsymbol{q}$ is the heat flux density, and W encompasses the energy transfer between species. Usually, the first three moments of the VFP equation are used along with Maxwell's equations and Ohm's law; however, an assumption about the form of W, $\vec{q}$, $\boldsymbol{\pi}$, and $\vec{F}$ must be made to fully close the system. A common closure is based on the work of Braginskii [24, 26] that utilises an asymptotic expansion about the small ratio of the mean-free-path to the macroscopic length scale of the plasma. This is specifically applicable to collisional plasmas where the mean-free-path is very small due to a high collision frequency. The resulting equations are based on the electron and ion collision

times given by

$$\tau_e = \frac{6\sqrt{2}\pi^{3/2}\epsilon_0^2\sqrt{m_e}T_e^{3/2}}{e^4 n \ln \Lambda}$$

$$\tau_i = \frac{12\pi^{3/2}\epsilon_0^2\sqrt{m_i}T_i^{3/2}}{e^4 n \ln \Lambda}$$

(1.8)

where ϵ_0 is the vacuum permittivity, m_e and m_i are the electron and ion masses respectively, T_e and T_i are the electron and ion temperatures respectively, e is the electron charge, and $\ln \Lambda$ is the Coulomb logarithm often calculated as

$$\ln \Lambda \approx 6.6 - 0.5 \ln n + 1.5 \ln T_e$$

(1.9)

with the density, n, in units of 10^{20}m^{-3} and the electron temperature, T_e, in units of electron volts. The Coulomb logarithm is defined as the natural log of the ratio of the maximum and minimum impact distances for small Coulomb collisions. The maximum distance is the Debye length since this is the length below which the potential is no longer screened, and the minimum distance is the distance of closest approach between the colliding particles.

Using the standard two-Laguerre-polynomial Chapman-Enskog closure scheme [27], the expressions for W_j and $\vec{F}_j$ in equations 1.6 & 1.7 are obtained in the magnetised limit $\Omega_i\tau_i, \Omega_e\tau_e \gg 1$,

$$\vec{F} = ne\left(\frac{\vec{J}_\parallel}{\sigma_\parallel} + \frac{\vec{J}_\perp}{\sigma_\perp}\right) - 0.71n\nabla_\parallel T_e - \frac{3n}{2|\Omega_e|\tau_e}\left(\hat{b} \times \nabla_\perp T_e\right)$$

$$W_i = \frac{3m_e n\left(T_e - T_i\right)}{m_i\tau_e}$$

$$W_e = -W_i + \frac{\vec{J}\cdot\vec{F}}{ne} = -W_i + ne\left(\frac{J_\parallel^2}{\sigma_\parallel} + \frac{J_\perp^2}{\sigma_\perp}\right) - 0.71nJ_\parallel\nabla_\parallel T_e - \frac{3n}{2|\Omega_e|\tau_e}\left(\vec{J}_\perp \cdot \nabla_\perp T_e\right)$$

(1.10)

where $\vec{J} = en(\vec{v}_i - \vec{v}_e)$ is the current density, σ is the conductivity, and $\Omega_{i/e}$ is the cyclotron frequency for each species. There are two separate conductivities for the parallel and perpendicular direction due to the magnetic fields limiting motion in the perpendicular direction, and each of these affects the corresponding direction of the current density. Defining $\vec{J}_\parallel = \hat{b} \cdot \vec{J}$ and $\vec{J}_\perp = \vec{J} - \vec{J}_\parallel$ is useful for the formalism. The

conductivities are calculated by

$$\sigma_\perp = 0.51\sigma_\parallel = \frac{ne^2\tau_e}{m_e} \tag{1.11}$$

noting that the parallel conductivity is nearly twice as large as the perpendicular conductivity. The first term in the force equation in 1.10 describes the friction due to electrons and ions moving in opposite directions when current flows creating a 'drag' that slows the motion and lowers the current. The second term of the force equation is called the thermal force and describes the average friction due to a gradient in thermal velocities when there is a parallel temperature gradient. The last term is also a thermal force term, but perpendicular to the field. Particles on neighbouring field lines gyrate, and there is a friction between them proportional to the temperature for each particle. Any difference in the temperature then produces a force imbalance and a net frictional force contributes to the overall force.

In equation 1.10, W_i is the rate that energy is transferred from the electrons to the ions through collisions. The direction of this transfer is easily seen to be positive if the electrons are hotter than the ions, as expected. Note, though, that this term is very small due to the relative mass imbalance between the species. W_e is the energy gained by the electrons from the ions, so it of course includes the negative of the energy transferred to the ions. The second term $\vec{J} \cdot \vec{F}$ includes multiple effects when expanded. Firstly, Ohmic heating is included as the J^2 terms, and can only add heat to the system since this term is always positive. The two remaining terms describe the work done by the thermal force (both parallel and perpendicular) and can add or remove heat depending on the direction of the temperature gradient relative to the current density.

To fully close the system, $\boldsymbol{q}_j$ and $\boldsymbol{\pi}_j$ must also be defined. The heat flux densities for ions and electrons are given by

$$\boldsymbol{q}_e = -\kappa_\parallel^e \nabla_\parallel T_e - \kappa_\perp^e \nabla_\perp T_e - \kappa_\times^e \hat{b} \times \nabla T_e - 0.71\frac{T_e J_\parallel}{e} - \frac{3T_e}{2\left|\Omega\right|_e \tau_e e}\hat{b} \times J_\perp$$

$$\boldsymbol{q}_i = -\kappa_\parallel^i \nabla_\parallel T_i - \kappa_\perp^i \nabla_\perp T_i + \kappa_\times^i \hat{b} \times \nabla_\perp T_i \tag{1.12}$$

where κ is the thermal conductivity. The perpendicular heat conductivities are defined as

$$\kappa_\perp^e = 4.7 \frac{nT_e}{m_e \Omega_e^2 \tau_e} \qquad\qquad \kappa_\perp^i = 2 \frac{nT_i}{m_i \Omega_i^2 \tau_i} \tag{1.13}$$

The parallel heat conductivity is given by

$$\kappa_\parallel^e = 3.2 \frac{nT_e \tau_e}{m_e} \qquad\qquad \kappa_\parallel^i = 3.9 \frac{nT_i \tau_i}{m_i} \tag{1.14}$$

Finally, then cross thermal conductivity, that is in the direction of $\hat{b} \times \vec{\nabla}_\perp T$ are

$$\kappa_\times^e = 2.5 \frac{nT_e}{m_e |\Omega_e|} \qquad\qquad \kappa_\times^i = 2.5 \frac{nT_i}{m_i |\Omega_i|} \tag{1.15}$$

The first three terms of equations 1.12 for ions and electrons simply account for the heat flux due to the thermal conduction and diffusion in each direction, but must be separated due to different levels of conductivity as a consequence of the magnetic topology. The fourth and fifth terms in the electron equation describe the heat flux due to thermal convection, and only appear in the electron equation due to the relative mobility of the electrons compared to the ions.

In order to define the stress tensor, it is convenient to first define the rate-of-strain tensor

$$\mathbf{S}_{\alpha\beta} = \frac{\partial v_\alpha}{\partial r_\beta} + \frac{\partial v_\beta}{\partial r_\alpha} - \frac{2}{3} \vec{\nabla} \cdot \vec{v} \delta_{\alpha\beta} \tag{1.16}$$

where α and β are Cartesian coordinates orthogonal to the magnetic field. Then the stress tensor, $\boldsymbol{\pi}_j$, is defined as the sum of multiple components

$$\boldsymbol{\pi}_s = \boldsymbol{\pi}_0 + \boldsymbol{\pi}_1 + \boldsymbol{\pi}_2 + \boldsymbol{\pi}_3 + \boldsymbol{\pi}_4 \tag{1.17}$$

where

$$\boldsymbol{\pi}_0 = -3\eta_0 \left(\mathbf{bb} - \frac{1}{3}\mathbf{I}\right)\left(\mathbf{bb} - \frac{1}{3}\mathbf{I}\right) : \nabla \vec{v}$$

$$\boldsymbol{\pi}_1 = \eta_1 \left(\mathbf{I}_\perp \cdot \mathbf{S}_{\alpha\beta} \cdot \mathbf{I}_\perp + \frac{1}{2}\mathbf{I}_\perp \left[\vec{b} \cdot \mathbf{S}_{\alpha\beta} \cdot \vec{b}\right]\right)$$

$$\boldsymbol{\pi}_2 = 4\eta_1 \left(\mathbf{I}_\perp \cdot \mathbf{S}_{\alpha\beta} \cdot \mathbf{bb} + \mathbf{bb} \cdot \mathbf{S}_{\alpha\beta} \cdot \mathbf{I}_\perp\right) \qquad (1.18)$$

$$\boldsymbol{\pi}_3 = \frac{\eta_3}{3} \left(\vec{b} \times \cdot \mathbf{S}_{\alpha\beta} \cdot \mathbf{I}_\perp - \mathbf{I}_\perp \cdot \mathbf{S}_{\alpha\beta} \times \vec{b}\right)$$

$$\boldsymbol{\pi}_4 = 2\eta_3 \left(\vec{b} \times \cdot \mathbf{S}_{\alpha\beta} \cdot \mathbf{bb} - \mathbf{bb} \cdot \mathbf{S}_{\alpha\beta} \times \vec{b}\right)$$

where $\mathbf{I}$ is the identity tensor, $\mathbf{I}_\perp = \mathbf{I} - \mathbf{bb}$ is the perpendicular identity tensor, $\mathbf{bb}$ is the unit tensor indicating the direction of the magnetic field, and the η terms are viscosity coefficients given by

$$\eta_0^e = 0.73 n \tau_e T_e \qquad\qquad \eta_0^i = 0.96 n \tau_i T_i$$

$$\eta_1^e = 0.51 \frac{n T_e}{\Omega_e^2 \tau_e} \qquad\qquad \eta_1^i = 0.3 \frac{n T_i}{\Omega_i^2 \tau_i} \qquad (1.19)$$

$$\eta_3^e = -0.5 \frac{n T_e}{|\Omega_e|} \qquad\qquad \eta_3^i = 0.5 \frac{n T_i}{\Omega_i}$$

The $\boldsymbol{\pi}_0$ term equation in 1.18 is the parallel stress tensor which determines the viscosity along the field lines. The next two terms, $\boldsymbol{\pi}_1$ and $\boldsymbol{\pi}_2$, describe the perpendicular viscosity, which is significantly smaller than the parallel viscosity. Finally, $\boldsymbol{\pi}_3$ and $\boldsymbol{\pi}_4$ are the gyroviscosity terms; however, the stresses are always perpendicular to the velocity gradient, so no energy is dissipated [25].

The full Braginskii system is now closed, so it is possible to simulate such a set of equations. However, they are obviously complex and the computation required is excessive since further simplifications can be made to reduce the system for particular regimes.

1.3.1.1 Drift-reduced fluid models

It is common practice, made popular by Mikhailovskii and Tyspin [28], especially for the edge plasma (ie. plasma located outside the separatrix), to perform a drift-reduction on the momentum equation. This assumes that the perpendicular motion is dominated by the $\vec{E} \times \vec{B}$ drift (to be discussed in section 1.3.3.1). These assumptions are thought

to be reasonable in the edge due to the low collisionality and temperatures; however the validity of this assumption is discussed in significant detail in chapter 3.

The drift-reduction involves taking the curl of the momentum equation which results in an equation for the vorticity. The parallel component of this vorticity equation is then used in conjunction with the parallel momentum equation and the other moments of the VFP equation to represent the system. Done in this way, the parallel vorticity equation actually describes the divergence-free current in the system.

$$\underbrace{\frac{\partial \varpi}{\partial t}}_{} = -\vec{\nabla} \cdot \left(\varpi \hat{b} \times \frac{\nabla \phi}{|B|} \right) - \underbrace{\vec{\nabla} \cdot \left(n \left[v_{e\parallel} - v_{i\parallel} \right] \right)}_{\text{parallel current}} - \underbrace{\vec{\nabla} \cdot \left(-p_e \vec{\nabla} \times \frac{\hat{b}}{B} \right)}_{\text{diamagnetic current}} \qquad (1.20)$$

$$\underbrace{\phantom{\frac{\partial \varpi}{\partial t} = -\vec{\nabla} \cdot \left(\varpi \hat{b} \times \frac{\nabla \phi}{|B|} \right)}}_{\text{polarisation current}}$$

where $\varpi = \vec{\nabla} \cdot \left(\frac{n}{B^2} \nabla_\perp \phi \right)$ is the parallel vorticity, and ϕ is the electric potential. This governs the perpendicular motion of the ions, while the electron dynamics are then determined by evolving the vector potential and relating the parallel current back to the electric potential.

$$\frac{m_e}{m_i} \frac{\partial v_{e\psi}}{\partial t} = \frac{\eta}{n} \left(J_\parallel - J_{\parallel 0} \right) + \nabla_\parallel \phi - \frac{1}{n} \nabla_\parallel p_e - 0.71 \nabla_\parallel T_e \qquad (1.21)$$

where $v_{e\psi} = v_{e\parallel} + \frac{1}{2} \frac{m_i}{m_e} \beta_e \psi$, β_e is the ratio of magnetic to plasma pressure, η is the parallel resistivity, $J_{\parallel 0}$ is the equilibrium current density, and ψ is the poloidal flux which is proportional to the parallel vector potential. The parallel current density is then related back to the poloidal flux, $J_\parallel = \nabla_\perp^2 \psi$. This is much more efficient than directly evolving the electron momentum equation.

A drift-reduced system like this is commonly used for simulation since it reduces the time-scales of importance by assuming $\omega \ll \Omega_i$, which increases the minimum time-step allowed in simulation to still satisfy the Courant-Friedrichs-Lewy (CFL) condition [29]. The simplicity of the system can also make it more amenable to analytic work.

1.3.2 MHD and Equilibria

The MHD equations are a combination of the first two moments of the VFP equation, Maxwell's equations, and a closure based on the heat capacity ratio for a monatomic gas. This is a very simple model for looking at the stability of a plasma, yet many complex behaviours observed in experiment can be explained using MHD. The MHD equations are similar to the fluid equations presented in the previous section, with some important simplifications. Ideal MHD is a single fluid description of the plasma that assumes zero resistivity.

$$
\begin{aligned}
\frac{\mathrm{d}n}{\mathrm{d}t} + n\vec{\nabla} \cdot (\vec{v}) &= 0 \\
m_i n \frac{\mathrm{d}\vec{v}}{\mathrm{d}t} - \vec{J} \times \vec{B} + \nabla p &= 0 \\
\frac{\mathrm{d}}{\mathrm{d}t}\left(\frac{p}{n^{5/3}}\right) &= 0 \\
\vec{E} + \vec{v} \times \vec{B} &= 0
\end{aligned}
\tag{1.22}
$$

1.3.2.1 Grad-Shafranov equation

An equilibrium equation can be derived from MHD, equations 1.22, by assuming the plasma is in steady state ($\frac{\partial}{\partial t} = 0$), stationary ($\vec{v} = 0$), and is axisymmetric (ie. no toroidal variation). This often-used solution is called the Grad-Shafranov equation [23], given by

$$
R\frac{\partial}{\partial R}\left(\frac{1}{R}\frac{\partial \psi}{\partial R}\right) + \frac{\partial^2 \psi}{\partial Z^2} = -\mu_0 R^2 \frac{\mathrm{d}p}{\mathrm{d}\psi} - \frac{1}{2}\frac{\mathrm{d}F^2}{\mathrm{d}\psi}
\tag{1.23}
$$

where μ_0 is the magnetic permeability, ψ is the poloidal magnetic flux (which acts as a pseudo-radial coordinate), $F(\psi) = RB_\phi$, and $p(\psi)$ is the pressure. It is from this equation that the standard tokamak flux surface equilibrium is obtained. Figure 1.5 shows these flux surface contours, which are a solution to the Grad-Shafranov equation.

The equilibrium contours traced out by these surfaces of constant poloidal flux are appropriately called flux surfaces and are important in understanding the stability at various points in the plasma. From equation 1.23, the plasma pressure must be constant on a given flux surface, which makes the poloidal flux and ideal coordinate to
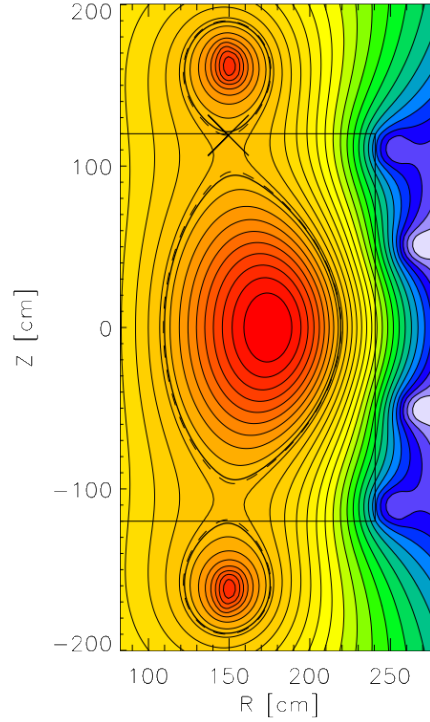
Figure 1.5: The solution for ψ to the Grad-Shafranov equation is the equilibrium poloidal magnetic flux given a pressure profile and magnetic field. This figure shows an example equilibrium for the Mega Ampere Spherical Tokamak (MAST) coils without the central solenoid as produced from GRASS (a Grad-Shafranov iterative solver developed at CCFE [30]).

use for the radial direction, as was indicated in figure 1.4.

1.3.3 Transport

The transport of heat and particles within a tokamak is divided into two categories - perpendicular and parallel to the magnetic field lines. This is due to the significant difference in time scales between these transport processes. The Lorentz force, shown in equation 1.3, dictates that the magnetic field constrains the perpendicular motion to be a gyration around the field line, while the parallel motion is unaffected by the magnetic field. This asymmetry is seen, for example, in the parallel and perpendicular heat conductivities given in equations 1.13 & 1.14. Perpendicular transport sets the limit on the confinement time for energy and density in a tokamak, and it is this confinement time that determines the effectiveness of a tokamak at generating fusion energy. For this reason, understanding and predicting transport is essential in producing a working fusion reactor. Theoretical understanding of the important perpendicular transport is broken into three categories: classical, neoclassical, and anomalous, which are outlined in the next few subsections.

1.3.3.1   Classical

Classical transport includes the effects of simple diffusion as well as particle drifts due to the magnetic topology. There is an intrinsic energy diffusion perpendicular to field lines due to collisions, which was defined mathematically in section 1.3.1. The diffusion of heat is described by $\vec{\nabla} \cdot \mathbf{q_j}$, where $\mathbf{q_j}$ is defined, as in equation 1.12, as the heat conductivity multiplied with ∇T. This results in a standard diffusion term $\vec{\nabla} \cdot (\kappa \nabla T)$.

The dominant drift mechanism is $\vec{E} \times \vec{B}$ drift, which is a result of ∇B and curvature drifts [31]. In a tokamak, there is a gradient in the total magnetic field that points inward along the major radius, and the magnetic field itself points mostly toroidally with a small poloidal component. In this scenario, particles move not only in their cyclotron orbits, but also drift vertically with a velocity

$$\vec{v}_{\nabla B} = \frac{mv_\perp^2}{2e\,|B|}\frac{\vec{B} \times \nabla B}{B^2} \tag{1.24}$$

where $v_\perp$ is the perpendicular velocity, e is the charge, m is the mass of the species, and $\vec{B}$ is the magnetic field. This drift is perpendicular to both the magnetic field and the gradient of the magnetic field, making it nearly vertical in a tokamak. Along with the ∇B drift, there is also a perpendicular drift due to the curvature of the device. This velocity is given by

$$\vec{v}_R = \frac{mv_\parallel^2}{eR^2B^2}\vec{R} \times \vec{B} \tag{1.25}$$

where $v_\parallel$ is the parallel velocity and $\vec{R}$ is the radius of curvature pointing outward. Importantly, both of these drifts depend on the particle's charge and will therefore be in opposite directions for ions and electrons. This causes a charge separation to develop generating a vertical electric field. The electric field then forces both species to drift radially outward regardless of charge via the $\vec{E} \times \vec{B}$ drift,

$$\vec{v}_{E\times B} = \frac{\vec{E} \times \vec{B}}{B^2} \tag{1.26}$$

where $\vec{E}$ is the electric field. Since the electric field here points in the direction of the curvature drift, it can easily be seen that the $\vec{E} \times \vec{B}$ drift will force particles to drift along positive $\vec{R}$, or outward from the centre of the torus. This outward drift is one of the dominant mechanisms for perpendicular density transport in neoclassical theory. It is actually due to this drift that a tokamak has both a toroidal and poloidal field - the poloidal field causes the vertical curvature and grad-B drifts to cancel in a single poloidal orbit, as shown in figure 1.6, preventing the charge separation and thus reducing the perpendicular transport to only collisional levels.
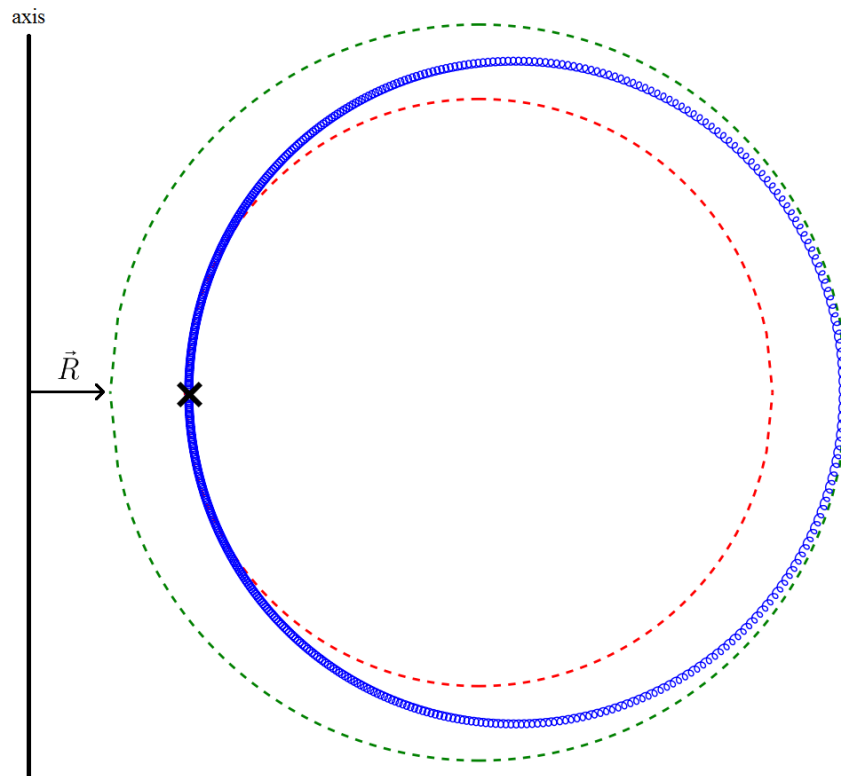
Figure 1.6: The poloidal projection of a particle moving around a circular cross-section tokamak, blue, shows the cancellation of the vertical grad-B and curvature drifts. The particle starts at the black "X" on the inner flux surface, shown as a red dotted line, and moving clockwise drifts upwards continually causing it to move to a flux surface further out, shown as the green dotted line, by the time it has reached to the outer mid-plane. The upward drift continues, however, as it moves downward from the outboard mid-plane resulting in the particle returning to the flux surface on which it originated.

The collisional, or diffusive, density transport is described by the $\vec{\nabla} \cdot \pi_{\mathbf{s}}$ term in equation 1.6, the momentum equation, and the stress tensor is given by equation 1.18. As momentum diffuses across the field lines the density does as well due to conservation of energy. The classical level of velocity and density diffusion expected due to ion/electron collisions is described in equations 1.17-1.19, and specifically the $\pi_{\mathbf{1}}$ and $\pi_{\mathbf{2}}$ components

of the stress tensor.

The collisional transport of heat and density is very small, so the typical classical transport length scale is limited by the Larmor radius (the radius of perpendicular gyration around magnetic field lines), which would lead to very compact tokamak devices [17]. Unfortunately, this is not the entire picture as there are drift and kinetic effects, deemed neoclassical, that provide a larger lower limit on the perpendicular transport.

1.3.3.2 Neoclassical

In addition to particle drifts, the perpendicular transport can also be strongly affected by kinetic effects. A particle moving in a spatially varying magnetic field will conserve energy and magnetic moment, which necessarily results in a parallel acceleration. If the particle moves from an area of low magnetic field to high magnetic field, it will slow down and in some cases, reverse direction if the ratio of the original to destination magnetic fields is large enough. In a tokamak this can happen if a particle is moving along a field line on the outboard, or low-field, side of the machine. As it moves toroidally and poloidally it sees an increasing magnetic field from the toroidal field coils and is reflected if it satisfies the condition

$$\frac{v_\perp}{v} > \sqrt{\frac{B_{\min}}{B_{\max}}} \tag{1.27}$$

which is to say it must have a large enough fraction of its velocity in the perpendicular direction. If a particle is reflected in a tokamak, the vertical drifts described in the previous section no longer cancel because the particle does not traverse the full poloidal angle [32]. This leads to a particle with an orbit whose poloidal projection resembles a banana, as shown in figure 1.7, hence the term banana orbit. These trapped particles increase the transport significantly because they connect flux surfaces across a radius of δ_B, the width of the banana orbit, given by

$$\delta_B \simeq \frac{\pi \rho_i q}{\sqrt{2\epsilon}} \tag{1.28}$$
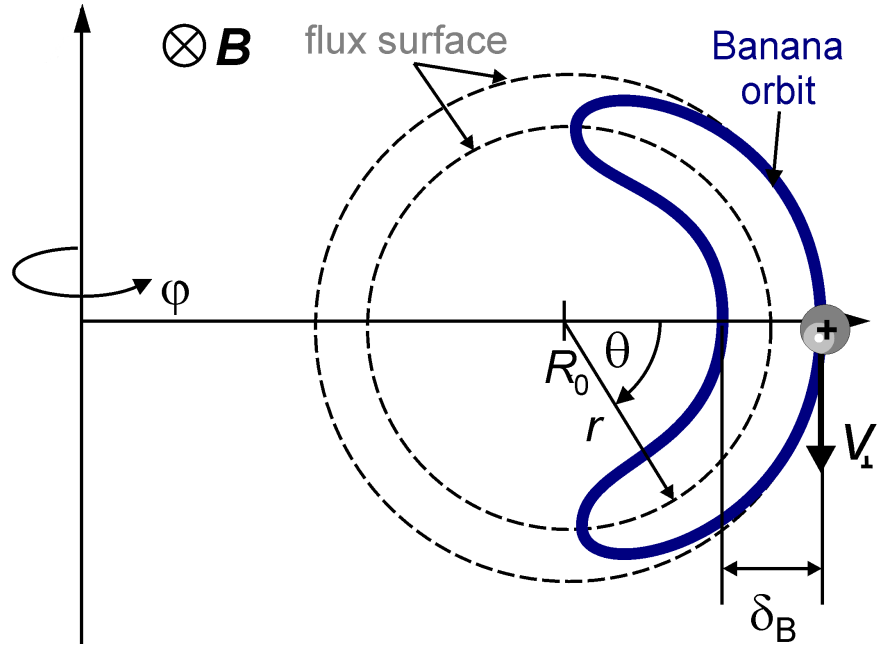
Figure 1.7: A schematic of poloidal projection of a trapped particle in a tokamak. The banana width, δ_B, is the limiting factor for the perpendicular transport as it connects flux surfaces and flattens profiles.

where $q = \dfrac{rB_\phi}{RB_\theta}$ is the safety factor and $\epsilon = \dfrac{r_0}{R_0}$ is the inverse aspect ratio of the tokamak defined as the ratio of minor to major radius. Since $\epsilon < 1$ and to avoid instability $q > 1$, the banana width will always be greater than the Larmor radius, which is the classical transport scale length. Typically, neoclassical transport is an order of magnitude greater than classical, increasing the minimum requirement for machine size to maintain the necessary confinement time. If this were the only limiting factor, however, fusion devices could still be very small - on the order of a metre or two. Transport measured in experiment is unfortunately another order of magnitude greater than the predictions of neoclassical theory [33, 34], therefore is dubbed "anomalous." It is this that truly limits tokamak performance, and is discussed in the next section.

1.3.3.3 Anomalous

Anomalous transport refers to the approximately order of magnitude difference between the perpendicular transport measured in experiment and the transport expected from neoclassical theory [35]. Much research has been done in this area, but the exact source of this anomalous transport remains unknown, but the most common theory is that turbulence driven by micro-instabilities (including drift-wave, ion-temperature gradient (ITG), electron-temperature gradient (ETG), trapped electron modes (TEM), the drift micro-tearing mode, *et al.*) is responsible [36–38]. Details of the electron drift-wave

instability will be discussed in the next section, but the other micro-instabilities are outside the scope of this work.

1.3.4 Turbulence

Not just limited to plasma physics, turbulence is a fluid dynamical phenomenon that dictates the behaviour of a fluid. The characteristics of turbulence are not perfectly defined, but usually include a sensitivity to initial conditions (chaotic yet deterministic), diffusivity, irregularity (in space and time), rotation (i.e. the formation of eddy structures), and dissipation (internal conversion of kinetic to thermal energy). In plasmas, turbulence is caused by micro-instabilities, of which drift-waves are the most universal, so they are discussed in detail in the next section.

1.3.4.1 Drift-wave instability

Drift-waves are not innately unstable, but are instead a propagating perturbation in plasma density. Figure 1.8 shows the geometry of a simple ion drift-wave, which only requires a ion density gradient at an angle to the magnetic field and an ion density perturbation to begin propagation. The perturbation perpendicular to the density
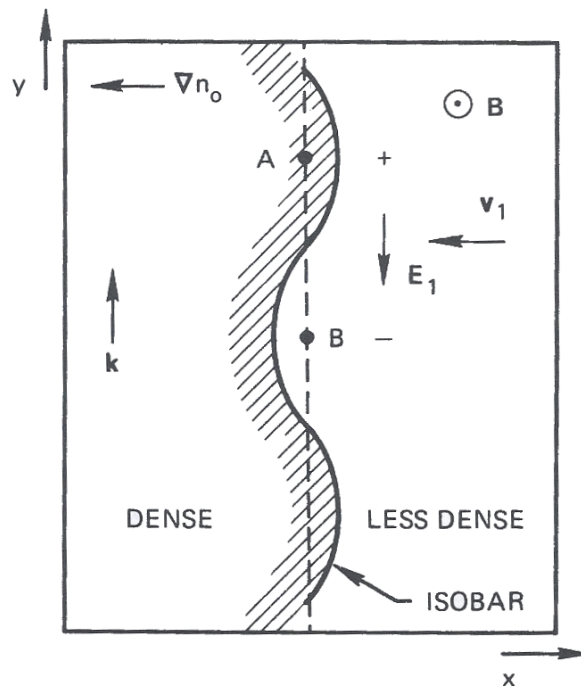
Figure 1.8: The diagram shows the required elements for a drift-wave to develop and propagate. It is called the universal instability because these requirements are ubiquitous in a tokamak - all that is required is a density gradient at an angle to the magnetic field [18]. Here, the density gradient is in the negative x-direction and the magnetic field is out of the page in the z-direction.

gradient creates regions of higher and lower density near each other, and the electrons stream along the field line (into/out of the page) to maintain force balance (i.e. $\hat{b} \cdot \nabla p = e n_e \hat{b} \cdot \nabla \phi$) and satisfy the Boltzmann relation [39]. The Boltzmann relation is an equilibrium assumption that is valid for electrons parallel to the magnetic field due to the small mass, thus very fast response to forces. Starting with the momentum equation (eqn. 1.6) it is assumed that the electrons are in equilibrium ($\frac{\mathrm{d}v_\parallel}{\mathrm{d}t} = 0$), the stress/friction is zero, and the parallel behaviour is isolated resulting in the equation $ne\nabla_\parallel \phi + \nabla_\parallel p_e = 0$. This can then be linearised with temperature variations neglected (so that $\nabla T_e = 0$), yielding the Boltzmann relation, $\delta\phi = \frac{T_0}{e} \frac{\delta n}{n_0}$, where T_0 and n_0 are the background temperature and density, respectively. This potential perturbation results in an electric field, E_1 that alternates between positive and negative in the $\hat{b} \times \nabla n$, or y-direction. In combination with the magnetic field, the electric field causes an $\vec{E} \times \vec{B}$ drift, v_1, that is 90 degrees out of phase with the density perturbation. As long as the electric field stays exactly 90 degrees out of phase, the wave is stable and simply propagates. If resistivity is included in the system, the electrons are retarded in their motion along the field line, shifting the phase of the potential perturbation causing the wave to become unstable and grow. As described in equation 1.11, the parallel resistivity (i.e. $\eta_\parallel = \sigma_\parallel^{-1}$) is non-zero due to collisions that disrupt the flow of electrons, but is often very small. The electrons can also be slowed through dissipative processes that cause them to lose energy, such as viscosity, which also destabilise the drift-wave.

The dispersion relation for the drift-wave can be derived using eqn. 1.5, the ion continuity equation

$$\frac{\partial \delta n_i}{\partial t} = -\vec{\nabla} \cdot \left(\left[n_0 + \delta n_i \right] \delta \vec{v} \right) \tag{1.29}$$

A sinusoidal form for the density perturbation is assumed, $\delta n_i \propto \exp(-i\omega t)$, so that $\frac{\partial \delta n_i}{\partial t} = -i\omega \delta n_i$, where ω is the frequency of the drift-wave oscillation. If the dominant perpendicular motion is assumed to be due to the $\vec{E} \times B$ drift, then equation 1.29 can be linearised to obtain

$$-i\omega \delta n_i = v_{E \times B} \frac{\mathrm{d}n_0}{\mathrm{d}x} \tag{1.30}$$

From equation 1.26, an expression for the perturbed $\vec{E} \times \vec{B}$ drift is obtained

$$v_{E \times B} = \frac{1}{B} \frac{\partial \delta \phi}{\partial y} = \frac{i k_y \delta \phi}{B} \tag{1.31}$$

where $\delta \phi \propto \exp(i k_y y)$ has been given the form of an oscillatory perturbation in space with wave number, k_y. Substituting this into equation 1.30 results in an expression for the density

$$n_i = \frac{k_y \delta \phi}{\omega |B|} \frac{\mathrm{d} n_0}{\mathrm{d} x} \tag{1.32}$$

This can then be equated to the electron density through the Boltzmann relation and, then assuming quasi-neutrality, which implies $n_i \simeq n_e$), a dispersion relation is found

$$\omega_* = \frac{k_y T_0}{e B n_0} \frac{\mathrm{d} n_0}{\mathrm{d} x} \tag{1.33}$$

where ω_* is the standard symbol for the drift-wave frequency. This will be used again in chapter 3 where the stability of drift-waves are explored using two different fluid models.

1.3.4.2 Drift-wave turbulence

Turbulence requires an energy source to feed the large scale structures continually, as it also provides a sink for energy in the small scales. This is the basis for the so-called cascade [40] that describes turbulent behaviour and is shown in figure 1.9. Energy from the background density or pressure gradient drives the drift-wave instability, which then feeds energy to the turbulent eddies (i.e. coherent structures of vorticity) at large scales (low-k). This energy is then transferred to smaller and smaller scales until the critical scale, called the Kolmogorov micro-scale, where the Reynolds number $Re = uL/\nu \approx 1$, and the energy is finally dissipated through viscosity as heat. In the Reynolds number definition, u is the fluid flow velocity, L is the system scale length, and ν is the viscosity. Viscosity is the resistance of a fluid to deformation through shear, and is described in the stress tensors in equation 1.18. In a more colloquial sense, viscosity describes the thickness of a fluid.
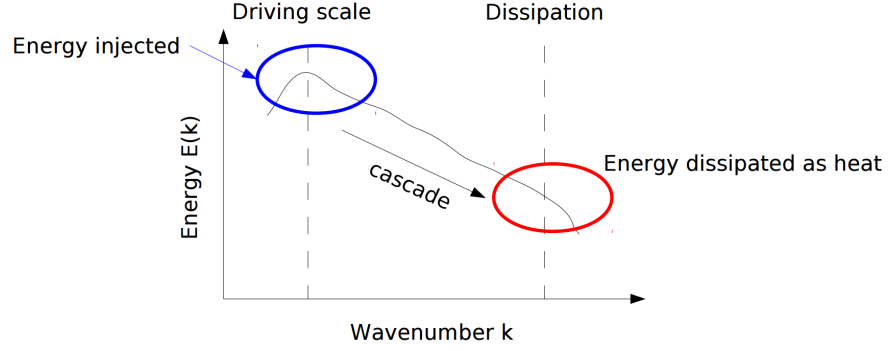
Figure 1.9: In the turbulence cascade, energy is injected into the system at large scales, generally from background free-energy sources, and is then transferred to smaller and smaller scales until it is dissipated at some critical size [17].

Interestingly, the slope of this cascade is well-defined experimentally and was calculated by Kolmogorov and reviewed by Hunt [41], through a startling simple dimensional analysis. By recognising that eddies in the mid-k range, or what is called the inertial sub-range, are too small to feel the effect of large scale structures but too big to be affected by viscosity, an assumption can be made that the energy in each scale is described by a function of only the energy dissipation rate and the local scale

$$E = f\left(\varepsilon, k\right) \tag{1.34}$$

where E is the energy at each scale with units L^2/t^2, ε is the energy dissipation rate with units L^2/t^3, and k is the wave number with units L^{-1}. A self-similar system, which is one where the dynamics of each scale is the same, can be described by

$$E = \varepsilon^{\alpha} k^{\beta} \implies \left[\frac{L^2}{t^2}\right] = \left[\frac{L^2}{t^3}\right]^{\alpha} \left[\frac{1}{L}\right]^{\beta} \tag{1.35}$$

Then, with dimensional analysis, the exponents are uniquely determined to be $\alpha = 2/3$ and $\beta = -2/3$. This result is one of the most celebrated laws of fluid dynamics as it is seen to fit experimental observations and is one of the few obtainable analytic results. Note that drift-wave turbulence, unlike standard fluid turbulence, can produce cascades with different slopes depending on the collisionality [42], due to the longer range of the collisions. Most other turbulence analysis is best done through simulation of the fluid equations described in section 1.3.1. Simulating plasma turbulence has benefits over regular fluid turbulence due to the constraints the magnetic field provides, allowing a quasi-2D description since structures are elongated along the field lines. However,

simulating turbulence can still prove difficult because such a large range of length scales must be resolved - a problem that is addressed in chapter 4.

1.3.4.3 Turbulence and confinement

As mentioned earlier, turbulence increases the transport from neoclassical theory by an order of magnitude. This is due to the formation of eddies, which have a radial extent that spans multiple Larmor radii and rotate, interacting and exchanging energy with other eddies further out. The resulting transport decreases the energy and particle confinement time from neoclassical levels. However, drift-wave turbulence has an interesting and crucial feature that gives hope to fusion still. Low-k flows spontaneously develop that can shear the plasma turbulence and lower transport. These zonal flows are constant in the toroidal and poloidal direction, but have a finite radial wave number. Many theories have been introduced in an attempt to explain this behaviour, though there is no certain description. Originally, these were thought to be due to an inverse cascade, which allows energy to flow from small structures back into large, self-organised structures [43–45]. This, however, has not been observed in gyrokinetic simulations, so the question of the cause of these zonal flows remains.

The standard regime in which tokamaks are operated to maximise confinement is the high confinement mode (H-mode) [46]. In this regime, the turbulence at the edge is suppressed, reducing perpendicular transport. This then shifts the entire density and temperature profiles upwards and allows the core to reach fusion relevant pressures. The reduction in turbulent transport is thought to be due to sheared flows tearing the eddies and reducing the transport length scales [47]. The explanation for these sheared flows is not known, but there are many suggested mechanisms including zonal flows [43], generation of a radial electric field [48], and geodesic acoustic modes [49].

1.3.4.4 L-H transition

The bifurcation in plasma behaviour from L-mode (low-confinement mode) to H-mode is called the L-H transition and is an area of much study. Experimentally, it has been determined that a minimum power threshold must be reached by the external heating (usually neutral beam injection, NBI) for the L-H transition to occur. Using

global minimisation techniques, scaling laws have been developed to describe the power thresholds observed across many experiments, as shown in figure 1.10.
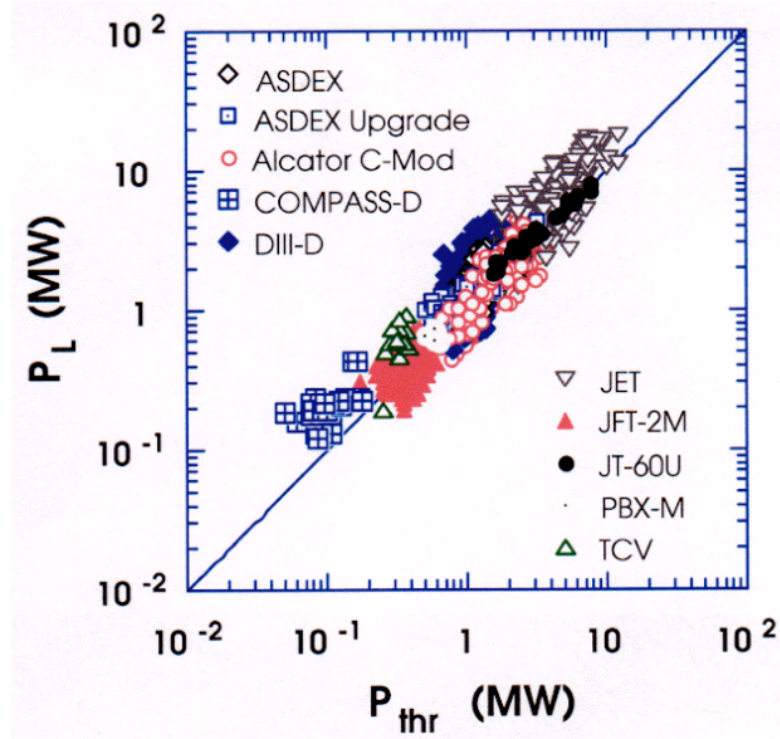
Figure 1.10: The power threshold for L-H transition scales as $P_{thr} = 0.45Bn^{0.75}R^2$ (SI units with n measured in $\times 10^{20} \mathrm{m}^{-3}$) as determined by fitting data from 10 tokamaks [50]. P_L is the input power for the experiments using NBI. Both P_{thr} and P_L are measured in MW.

Though the exact underlying mechanisms are unknown, it is believed that the transition involves either the stabilisation of a particular mode or a reduction of turbulent flux as some parameter passes a critical value. The potential modes stabilised at the edge of the core are peeling, ballooning (resistive and ideal), tearing, and drift-waves. In the scrape-off-layer, the potential responsible modes are resistive interchange, electron temperature gradient (ETG), and drift-waves. It is also possible that it is a combination of these modes that is suppressed reducing transport. The proposed specific models for the L-H transition involve both the core and edge, since the NBI power is deposited in the core, raises the profiles, and effects the edge pedestal [46, 51]. Current core and edge simulations have been unable to spontaneously develop an H-mode, but integrated simulations include the core-edge interaction that may allow for such a transition to occur.

1.3.5 Handling the power

Interestingly, H-mode is much easier to access in tokamaks with diverted plasmas [46], which is a plasma where there is a purposeful transition from closed field lines in the core to open field lines in the edge that terminate on a high heat-load handling material in the divertor. Not only does this give access to H-mode, it also provides a convenient way to exhaust heat from the system to a specific region. This is a working solution for current tokamaks, but will actually prove difficult in ITER, the next generation tokamak under construction in Cadarache, France, due to the high heat loads generated by a device of its size ($R_0 = 6.21$m) [52, 53].

1.3.5.1 Divertors

Figure 1.11 shows an example of a diverted plasma equilibrium. The last closed flux surface (LCFS), or separatrix, is shown to separate the core and scrape-off layer plasmas. Inside the LCFS the flux surfaces are closed, while outside the field lines terminate onto the divertor plates at the strike points.
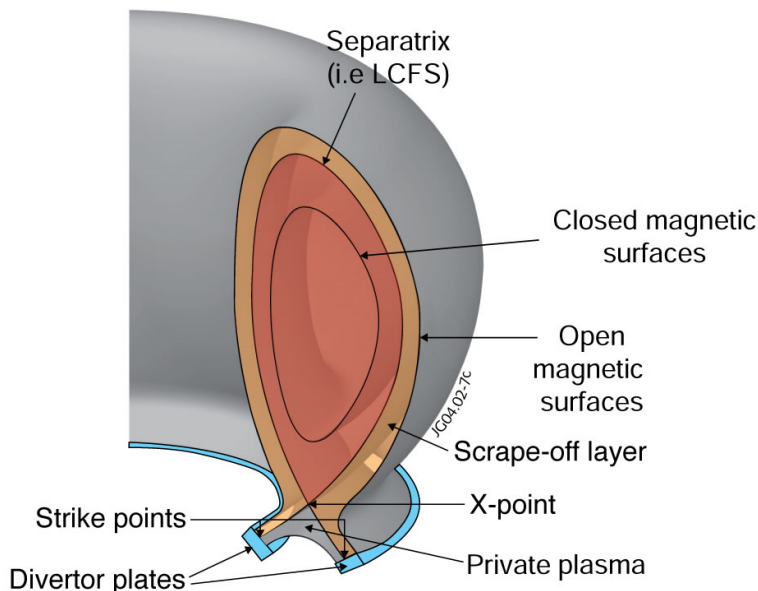
Figure 1.11: In this schematic of a diverted plasma, the core plasma is shown to have closed flux surfaces and the edge has open flux surfaces that terminate on the divertor plates at the strike points. The separatrix, or last closed flux surface (LCFS), contains an x-point where the field is purely toroidal. The scrape-off layer is the edge plasma outside of the LCFS [54].

In a diverted plasma, the behaviour of the density and temperature along the field line can be approximated by assuming the total pressure (thermal and dynamic) on a

given flux surface is constant, $p_{\mathrm{midplane}} = p_{\mathrm{divertor}}$ [55]. The Bohm sheath condition that describes plasma interaction with a surface indicates that the flow of the ions will be the sound speed at the divertor plate. If flows are assumed to be zero at the mid-plane, the pressure balance equation can be written

$$n_m T_m = \frac{m_i c_s^2}{2} + n_t T_t \tag{1.36}$$

where c_s is the sound speed, and the subscripts m and t indicate mid-plane and target, respectively. This equation says that the thermal pressure at the mid-plane is equivalent to the thermal pressure plus the ram pressure at the target. To solve for the temperature at the target, two more equations must be used to close the system. Firstly, the electron heat conductivity equation is [56]

$$q = -\kappa_0 T^{5/2} \frac{\partial T}{\partial y} \tag{1.37}$$

where q is the heat flux, y is the direction of the magnetic field, and κ_0 is the thermal conductivity given by $\kappa_0 = \kappa_{\parallel}^e T^{-5/2}$ from equation 1.14. To make this equation more useful, it can be integrated along the field line resulting in

$$T_m^{7/2} \approx T_t^{7/2} + \frac{7qL}{2\kappa_0} \tag{1.38}$$

where L is the connection length from mid-plane to target. The final required equation is for the heat flux at the divertor plate, and it describes the kinetic enthalpy of the flux of charged particles that make it to the surface

$$q = n_t c_s \gamma T_t \tag{1.39}$$

where γ is the heat transmission coefficient, normally $\gamma \approx 7$. This system can be solved to investigate the theoretical behaviour of the T_m/T_t as a function of mid-plane density, n_m, as shown in figure 1.12. This approximation is called the two-point model and is commonly used for analysis of the divertor performance because upstream density is one of the key plasma parameters that can be adjusted to obtain detachment [55, 57], a state of operation discussed in the next section.

45
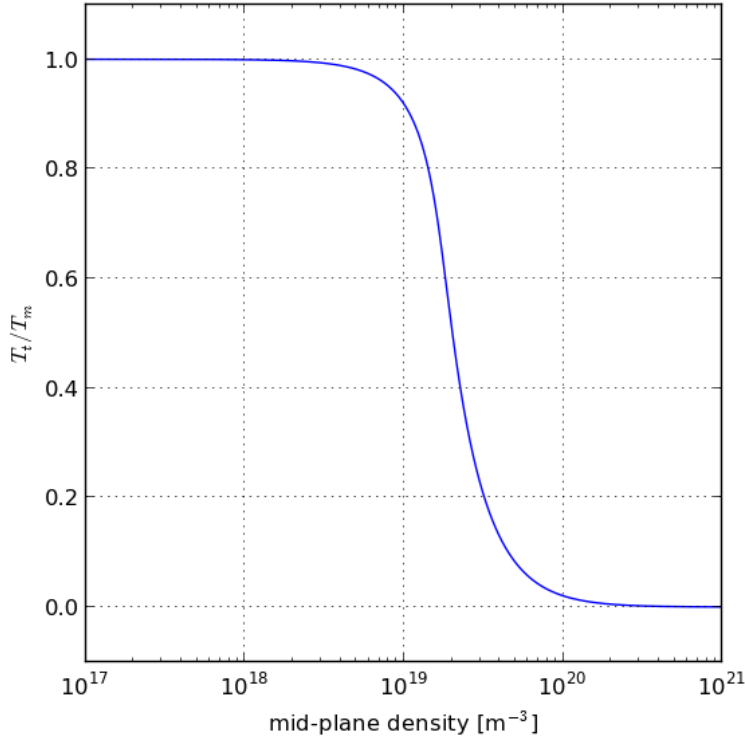
Figure 1.12: The two point model indicates that the ratio of temperature at the target to upstream (mid-plane) temperature decreases as a function of mid-plane density. For this plot $\gamma = 7$, $\kappa_0 = 2000$ [57], $T_m = 25$eV, and $L = 9$m.

1.3.5.2 Detachment

When plasma is incident on the divertor plates, neutrals are knocked off the surface and ionised, which serves as a plasma density source. A cloud of neutrals also begins to form as plasma in this region recombines, radiates, and undergoes charge exchange. If this recycling of plasma and the resulting neutral density is high enough, the plasma can reach a state of detachment where the energy of the plasma is fully radiated away before reaching the divertor plate. This serves to volumetrically disperse the large amount of energy instead of allowing it to be focused onto a small layer on the divertor plate, which can result in melting.

A cartoon of the density and temperature profiles along the field line for a detached plasma are shown in figure 1.13. Approaching the divertor plate, the temperature decreases as the plasma radiates and loses energy to the neutrals. The plasma density, however, increases due to force balance and the strong source of ions coming from the recycling. In the recycling region between L_r and L, the density falls back down to zero at the plate and the temperature remains constant. Detachment enables the

46

temperature to fall below 1eV at the divertor plate preventing damage, but also makes the plasma difficult to control. An experimentally important parameter, called the
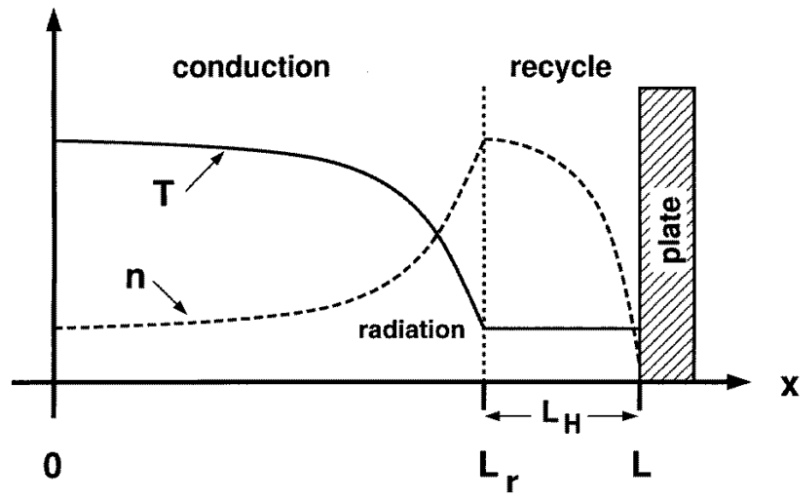
Figure 1.13: This cartoon describes the density and temperature profiles along the field line for a detached plasma [57].

degree of detachment (DoD) is based on the ratio of measured temperature at the plate compared to the analytic two-point value [58,59]. In chapter 5, edge and divertor simulations are performed, and the results are compared to two-point model.

1.3.6   Need for simulation

JET, the joint European torus at the Culham Centre for Fusion Energy (CCFE) is currently the largest tokamak in the world and has been since it began operation in 1983 [60]. However, ITER is current being built in southern France, and will be a large step on the roadmap to fusion as an energy source. After ITER, a demonstration fusion power plant, DEMO, will be built, though the plans are still in the very initial phases of design [61]. The steps from JET to ITER and then to DEMO are significant and can be seen in table 1.1. Such a large upgrade in operational parameters, such as plasma duration, magnetic field, and power gain Q, will take the plasma to regimes that have never been observed in experiment. The divertor for ITER is currently designed to operate in a partially detached regime, reducing the heat load to just under the material tolerance at 10MWm^{-2}. Yet, for DEMO a new solution must be found either in the plasma physics or in the materials. An important parameter that determines the heat load is the exhausted power divided by the major radius, since the wetted area of the divertor is defined as $A = 2\pi R \lambda / \sin(\alpha)$ where R is the

Table 1.1: Here the size and power of JET is compared with the upcoming ITER and DEMO tokamaks [61, 62]. The values used for DEMO are based on the European Power Plant Conceptual Study (PPCS) reactor design A.

	JET	ITER	DEMO
major radius (m)	3	6.2	9.55
minor radius (m)	1.25	2	3.2
volume (m^3)	90	840	1900
plasma current (MA)	6	15	30.5
axis magnetic field (T)	3.4	5.3	7.0
power gain Q	0.65	10	20
fusion power (MW)	16.1	500	5000
plasma duration (s)	10	300	10^7

major radius, λ is the SOL width, and α is the angle of the magnetic field to the divertor. Currently, there are predictions that λ does not scale with R [63] or even scales as R^{-1} [64]. This implies the area either scales weakly or not at all with major radius. This is a problem because power scales roughly as R^3, meaning ITER and DEMO, which have progressively larger major radii, should see a non-linear increase in power density on the divertor. The true scaling of the SOL width is not known or understood, so more analytic and computational work is required. It is for these reason that simulation is a major strategic research pathway for the ITER project and the International Tokamak Physics Activity (ITPA) committee [65]. This includes a wide variety of simulations ranging from exploration of fundamental plasma physics to optimisation of operational scenarios. The ITPA committee has divided up the areas of research that are emphasised to realise a working ITER and they are

- diagnostics

- energetic particle physics

- integrated operations scenarios

- MHD, disruptions, and control

- pedestal and edge physics

- scrape-off-layer and divertor

- transport and confinement

Each of these topics has key issues must be addressed, and simulation done in cooperation with experiment can provide answers to these. Integrated modelling of core and edge, which is the ultimate purpose of the research in this thesis, is directly applicable to the goals set forth by the ITPA "to improve understanding of pedestal and edge physics and the interplay between core, SOL and pedestal, including the impact of pedestal phenomena (pedestal structure, ELMs, etc) on the core and SOL (core confinement, heat and particle flows, etc)." There is a disparity between the optimal regimes for the edge and the core. To minimise the heat load on the divertor low upstream temperatures and high upstream densities are desirable; however, for the core fusion, high temperature is needed and high densities can hit intrinsic limits, such as the Greenwald limit [66]. Integrated simulations are ideal for research into resolving the discrepancy between these edge and core regimes because many regions of parameter space can be investigated, beyond what may be possible in current tokamaks.

This work also fits into the scrape-off-layer and divertor group's task to "participate in developing and validating divertor physics (including detachment, impurity transport and pumping) of ITER on the basis of experimental, theoretical, and modelling results." In the next chapter, an introduction to integrated modelling is given as well as an outline and motivation for the remaining chapters in the thesis.

Chapter 2

Integrated Modelling

2.1 Introduction

The behaviour of plasmas within tokamaks is very complex due to the many temperature and density regimes, plasma-wall interactions, effects of impurities, etc. Many codes have been written to analyse each of these effects independently, such as edge simulations with EDGE2D [67] and BOUT++ [68], core simulations with GYRO [69] and CENTORI [30], and neutral transport with EIRENE [70]. Each of these, and many other codes, are benchmarked and verified to accurately simulate a specific region or element of a fusion plasma. In reality, however, these processes are not independent but influence and interact with each other in a complex and non-linear way. This is the goal of integrated modelling - to couple existing, well-behaved, and benchmarked codes as to simulate the full tokamak plasma.

This is especially important leading up to the operation of ITER. A large focus is put on the development of integrated models that can accurately predict the performance for a given set of plasma parameters, so as to avoid disruption and other large instabilities that might damage the machine. EUROfusion, a cooperative organisation between 26 European countries, created a committee to address this specifically called the Integrated Tokamak Modelling (ITM) task-force [71], with goals to guide the community towards specific integrated modelling developments. One of the key areas of interest is the interaction between the core and the edge as this has seen experimentally to affect the transition to H-mode, the confinement quality, and pressure pedestal and

profiles [65].

2.2 Current codes

There have been integrated models developed previously with wide ranging levels of success. Some of the more notable codes are discussed in the following sections to give an indication of the current state of the field. Many of these seek to use simplified version of core and edge, while including more physics for neutrals, plasma-surface interaction, heating sources, etc.

2.2.1 JINTRAC

Developed at JET, JINTRAC is a suite of 25 individual codes that are integrated to simulate full plasma shot time scales (10 seconds) on the Joint European Torus, JET [72]. Though it is complex as a whole, the individual parts are simplified to include only the most necessary physics, which increases the running efficiency of the overall program. The core consists of a one-dimensional transport solver JETTO [73] coupled to an impurity transport code SANCO. Also in the core are auxiliary heating sources consisting of neutral-beam injection (NBI) by ASCOT and radio frequency heating by PION. The edge plasma is simulated as a 2-dimensional fluid with EDGE2D [67], along with three-dimensional kinetic neutral transport by EIRENE [70]. Though the core is approximated as one-dimensional and the edge as two-dimensional, the JINTRAC suite is still able to reproduce the density, temperature, and power for an entire JET shot (10s). This does, however, involve some heuristic adjustments to the perpendicular transport coefficients to replicate the L-H transition and H-mode [72].

2.2.2 SOLPS

SOLPS is an integrated simulation code that describes the edge plasma and neutral transport. It is made of two individual codes that are coupled. B2 is a two-dimensional fluid code capable of treating species with varying ionisation levels [74]. This is coupled to EIRENE [70], a three-dimensional, Monte-Carlo, kinetic neutral transport code, also used in JINTRAC. Despite this coupling, B2 also has the ability to simulate neu-

tral transport as a fluid interacting with the plasma instead of the kinetic treatment from EIRENE. For the interaction between EIRENE and B2 (i.e. the neutrals and the plasma) many atomic processes are simulated including ionisation, recombination, charge exchange, and radiation. Recently, B2 has been extended to also include radiation enhanced sublimation, thermal evaporation, and impinging particle backscattering for the interaction with the plasma facing surfaces [75]. SOLPS has been used to simulate detachment [76, 77], H-mode plasmas [78], Ohmic plasmas [79], and for the development of ITER design and scenario development [80]. Despite the usefulness of SOLPS in edge modelling, it does not include any contribution that the core may have on edge dynamics - a possible extension for SOLPS.

2.2.3 FACETS

FACETS was proposed in 2007 by John Cary at Tech-X Corporation and later developed in collaboration with Argonne National Labs, Lawrence Livermore National Labs, General Atomics, *et al* [81]. Originally the design was for a full fusion simulation project (FSP) to incorporate all dominant physics in a tokamak. It provides common data structures and interfaces that can be used by existing codes to communicate the state of the plasma in various regions. The plan of FACETS includes modules for core transport (custom 1D transport solver, ASTRA), neutral beam injection (NUBEAM), embedded turbulence (GYRO), and edge transport (UEDGE), with plans to incorporate plasma wall interaction (WALLPSI) and radio frequency sources (TORIC). All communication is handled through memory as the program is consolidated into a single executable file. Though developed in 2010, there have been no follow-up publications to the original computationally focused article [81], which demonstrated reasonable qualitative ion temperature profile evolution from core to edge. This is because the project was discontinued due to the extreme difficulty in compiling such a complicated executable.

2.3 Developing an integrated framework for coupled core/edge 3D turbulence simulations

The existing codes discussed in the previous section approximate the turbulence in edge and core through convective-diffusive transport instead of fully simulating it. It is the goal of this work to develop an integrated simulation that does resolve the turbulence and the transport it generates in the core and edge in full 3D geometry. This is an improvement from the previous attempts, which have made approximations in geometry and physics, with the hopes of higher levels of accuracy for both reproduction and prediction of plasma behaviour. In preparation for developing an integrated simulation of core-edge tokamak turbulence, a core and edge code were selected. The edge code chosen is BOUT++, developed by Ben Dudson at the University of York [68], which has been shown to very effectively simulate the turbulence and instabilities in the edge plasma. This was chosen over SOLPS for the edge due to the flexibility that is discussed in more detail in the next section. The core code chosen is CENTORI, a 2-fluid 3D electromagnetic turbulence code developed at CCFE by Peter Knight, *et al* [30]. A fluid code was chosen for its ability to simulate full shot time scales, unlike gyrofluid and gyrokinetic codes which are constrained to very small time scales due to the computational cost.

2.3.1 BOUT++

BOUT, a boundary turbulence code, was originally developed at Lawrence Livermore National Laboratories in 2001 [82] by Xu Xue-qiao. It was later upgraded in both functionality and efficiency by Ben Dudson at the University of York in 2009 [68] and renamed BOUT++. Currently, BOUT++ is an open source suite for solving differential equations with in-built tools specifically designed to benefit plasma physics simulation.

BOUT++ is flexible, allowing for the simulation of a wide range of user-defined systems of differential equations. It consolidates and provides convenient access to multiple time integrators (both implicit and explicit) and various orders and methods for spacial dif-

ferentiation, as well as Laplacian inversion. By default, BOUT++ uses the PVODE implicit time stepper [83], which is useful for both stiff and non-stiff systems. The geometry in which BOUT++ operates is also flexible spanning a wide range of relevant systems - slab, cylindrical, toroidal, field-aligned, flux-tube, and more. All that is required is a grid file that contains the location of the grid points and the metric tensors (both co- and contravariant) for the coordinate system. The code allows for parallelisation of two dimensions: the radial and poloidal directions.

Though BOUT++ itself does not have a fixed physics model that it solves, implementations of MHD equations within BOUT++ have been benchmarked rigorously for linear instabilities, such as ballooning, drift-waves, Kelvin-Helmholtz, and more for the tokamak edge plasma and linear devices [84, 85]. Non-linear studies have been benchmarked for turbulence [86–88], edge blobs [89–91], and the peeling-ballooning mode [92–94], and edge localised modes [95]. The numerical methods within BOUT++ have been verified using the method of manufactured solutions [96] (described in more detail in chapter 5).

BOUT++ is an ideal code for the edge simulation for two reasons. Firstly, it is well benchmarked and can be trusted in the simulation of edge turbulence. Secondly, the flexibility allows relatively easy development and verification of the coupling techniques for interpolation and communication between the core and edge (as described in detail in chapter 6).

2.3.2   CENTORI

CENTORI is a three-dimensional, two-fluid electromagnetic core turbulence code developed by Peter Knight *et al* at CCFE in 2012 [30]. It solves a single set of equations (described in detail in section 6.3), though terms can be enabled/disabled to simplify the system to electrostatic, single species, etc. The system solved by CENTORI is a full-velocity model (i.e. not drift-reduced) as described in section 1.3.1 that evolves density, temperature, velocity, and vector potential. As a fluid model, CENTORI does quickly what would be expensive to do with gyrokinetics in simulating turbulent trans-
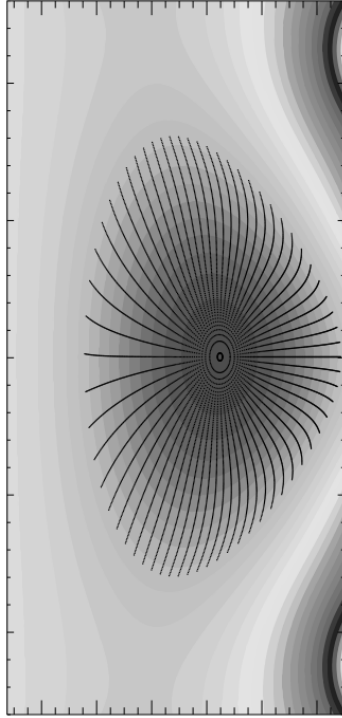
Figure 2.1: An example of a CENTORI grid shows a single poloidal plane with grid points in ψ and θ.

port on confinement and diffusive time scales in realistic tokamak geometries.

A unique feature of CENTORI to other core turbulence codes is its in-built Grad-Shafranov solver (GRASS). This allows the equilibrium to be recalculated intermittently so that it can evolve with the system instead of remaining a constant background. This is achieved by inputting the poloidal field coil locations and currents for the desired tokamak, and then using the on axis toroidal magnetic field, the plasma pressure, and the current density to calculate the new equilibrium.

CENTORI uses a slightly modified version of the standard tokamak coordinate system (ψ, θ, ϕ) such that arc lengths in the poloidal direction are equal. This comprises a series of toroidally spaced poloidal planes of grid points, as shown in figure 2.1. The simulations are parallelised in all three dimensions, leading to an excellent scaling of performance with number of processors [30, 97].

The initial paper introducing CENTORI is computationally focused and, though some 3D turbulence simulation results are presented, no benchmarking is included [30]. Because CENTORI has not existed for many years, there has been little else published

in the validation excepting for a paper by Robinson [98] in which CENTORI is seen to reproduce accurately the behaviour of geodesic acoustic modes (GAMs) according to the theoretical predictions.

However, CENTORI does have limitations. Fluid simulations are unable to accurately describe turbulence below the mean free path scale length. For collisional plasmas, the mean free path is very short ($\lambda_{mfp} \ll L$, where L is the system scale length), so fluid codes provide a sufficient description. When a plasma is collisionless like in the core of a tokamak, the mean free path, which scales strongly with the temperature, becomes larger than the size of the device making fluid simulations inaccurate. CENTORI, as a fluid code, lacks kinetic effects such as Landau damping, trapped particle effects, and banana and bootstrap currents. These can play an important role when collisional damping is low. CENTORI is chosen for the coupling work in this thesis because it runs quickly for long plasma simulation times, so it works well for proof-of-concept simulations. It is therefore an ideal choice as the core code to be integrated with BOUT++ in the edge due to its ability to simulate on the order of the confinement time as well as the self-consistent evolution of the plasma equilibrium. When paired with an edge code, interesting phenomena such as the L-H transition, which requires a bifurcation of the equilibrium, become possibilities and ultimate goals for the integrated simulation.

2.4 Outstanding challenges and thesis outline

There are four significant issues that will be addressed in this thesis on the route to developing an integrated tokamak core and edge fluid simulation. They are outlined in the following sections, each of which corresponds to a chapter.

2.4.1 Choosing a model

Though the code for the core is determined in CENTORI, the model for use in the edge is flexible due to the nature of BOUT++. For this reason, it is necessary to carefully identify and choose a model that is accurate for the particular low density and temperature, collisional regime in the edge plasma. Due to the desired long simulations,

it is necessary to choose a fluid model over gyrokinetic for computational feasibility. Within the category of fluid models there are still a variety of simplifications that can be made and these must be assessed for accuracy in the edge. The most common of these, the drift-reduction, is analysed for its suitability in chapter 3.

2.4.2   Efficiency

Due to the nature of the turbulent cascade, a wide range of lengths scales must be resolved in simulations to see the full tokamak edge but also see the dissipation that occurs at small scales. This often requires orders of magnitude in lengths, which is not computationally tractable. A method of addressing this issue, called large eddy simulation, has been developed where the small scales are not resolved; instead, extra dissipation is added to the system in an attempt to replicate the missing turbulent dissipation that is unresolved. Multiple methods that accomplish this have been developed, however, their suitability has not been explicitly explored. In chapter 4, four specific large eddy simulation dissipation models are tested and compared.

2.4.3   Accurate boundaries

Initial value partial differential equations are often sensitive to boundary conditions, and plasma equations are no exception. A core simulation in isolation must impose artificial boundary conditions at the edge that determine flux, flows, and have a significant impact on the entire core. An isolated edge simulation is similarly subject to its boundary conditions which exist on both radial edges. Though these boundary conditions are usually theoretically motivated and are as accurate as possible they are inherently linear in nature. This is the main benefit integrated modelling offers - providing actual boundary data for both simulations such that the system evolves as one.

There are a second set of boundaries in the edge that must also be addressed in the open flux-surface region where field lines terminate on a divertor plate. Here sheath conditions are used, but the current field-aligned coordinate system used for BOUT++ edge simulations limits the freedom of the poloidal geometry, which in turn decreases the accuracy of the boundary conditions. In chapter 5 an innovative coordinate sys-

tem that relaxes this limitation and maintains field-alignment is developed, tested, and used for novel plasma divertor simulations.

2.4.4 Coupling two simulations

In chapter 6, the results from all the previous chapters culminate in the coupling of the edge and core plasma simulations. Numerical problems are addressed as complexity is incrementally increased. The fully complex, integrated code is then utilised to explore the nature of turbulent transport from core to edge. Reasonable steady state behaviour is seen to develop in the core and edge, with fluctuations moving from core to edge. This proof-of-concept simulation opens the door for in-depth investigations of core-edge interaction in tokamaks.

Chapter 3

Validity of drift-reduced plasma models

3.1 Introduction

Fluid models are often used to describe plasma behaviour in a magnetic field, especially utilising the closure developed by Braginskii [24] that is valid for highly collisional plasmas, such as linear devices and in the tokamak edge, where collisional damping is the dominate damping mechanism. It is often asserted that only kinetics and gyrokinetics can truly describe plasma dynamics in collisionless regimes, such as the core of tokamaks [99]. This is because collisional damping plays a strong role in the formation of turbulence, but in its absence in collisionless plasmas, kinetic and finite Larmor radius effects such as Landau damping and neoclassical transport and currents dominate instead. These effects are analytically present only in gyrokinetic [100] and sometimes gyrofluid models [101, 102]. Fluid models are, however, still useful because of their simplicity and computational tractability compared to gyrokinetic models.

There has been a large effort to derive fluid models that provide both corrections and simplifications to the original Braginskii system [28, 103]. One such simplification, the so-called drift-reduction (or high-flow ordering), was originally derived by Mikhailovskii and Tsypin [28] and is a slow ordering that assumes $\omega < \omega_{ci}$, $\rho_i = 0$, and that the perpendicular velocities are domianted by the $\vec{E} \times \vec{B}$ drift, which relates the parallel vorticity to the potential: $\varpi_\parallel = \nabla_\perp^2 \phi$. This then involves reducing the momen-

tum equation by taking its curl resulting in an equation for the evolution of parallel vorticity, $\vec{\varpi} = \vec{\nabla} \times \vec{v}$.

The drift-reduction is often used when the plasma velocity is subsonic, where the inertia term is much smaller than the $\vec{J} \times \vec{B}$ and ∇p terms in the momentum equation. Taking the curl of the momentum equation removes these two terms, resulting in an equation that can more easily be evolved numerically. To close the system, the perpendicular velocity is related to the electric potential via the $\vec{E} \times \vec{B}$ drift velocity - $v_\perp \sim \dfrac{-\nabla \phi}{B}$. It is this assumption that is the key difference between a full velocity model (one that evolves all three components of the momentum equation) and a drift-reduced model (one that evolves the parallel velocity and parallel vorticity). This is discussed in detail in section 3.3.

By using linearisation techniques, the behaviour of these models can be compared to determine in which cases the drift-reduction is acceptable. The systems are simplified to the incompressible limit (such that $\vec{\nabla} \cdot \vec{v} = 0$) to look at the most basic case that still produces drift-waves. Any differences for this case, then, are fundamental and will carry on into more complex scenarios. Tokamaks are operated in well-defined yet broad parameter spaces, so the application of drift-reduced plasma fluid models for tokamak modelling can be explicitly explored.

The most universal drive mechanism for tokamak plasma turbulence is the drift-wave instability, which requires only a pressure or density gradient and non-zero resistivity to provide the free-energy drive [18]. Though turbulence is a thoroughly non-linear phenomenon, the linear growth rate of the drive instability indicates stability and determines the non-linear saturation time scale making linear analysis of these instabilities both relevant and essential. For this chapter, cgs Gaussian units are used for the analytics, and SI units appear in some of the analysis - both are clearly marked when used.

3.1.1 Full velocity model

The full fluid system that is investigated within this chapter consists of the first two moments of the kinetic equation, as described in section 1.3.1. This consolidated model is shown below:

$$\frac{\partial p_e}{\partial t} + \vec{\nabla} \cdot (n_e \vec{v}) = 0$$

$$n_e m_i \left(\frac{\partial \vec{v}}{\partial t} + \vec{\omega} \times \vec{v} \right) - \frac{\vec{J} \times \vec{B}}{c} + \nabla p_e + n_e m_i \nabla (\vec{v} \cdot \vec{v}) = 0$$

$$\frac{1}{c} \frac{\partial \vec{A}}{\partial t} + \nabla \phi - \frac{\vec{v} \times \vec{B}}{c} + \frac{\vec{J} \times \vec{B}}{en_e c} + \eta \vec{J} - \frac{\nabla p_e}{en_e} = 0 \tag{3.1}$$

$$\vec{J} - \frac{c}{4\pi} \left(\vec{\nabla} \times \left(\vec{\nabla} \times \vec{A} \right) \right) = 0$$

$$\vec{\nabla} \cdot \vec{J} = 0$$

where the vorticity $\vec{\omega} = \vec{\nabla} \times \vec{v}$, $\vec{J}$ is the current density, $\vec{B}$ is the magnetic field, $\vec{v}$ is the ion velocity, n_e is the plasma density, $\vec{A}$ is the vector potential, ϕ is the electric potential, p_e is the electron pressure, m_i is the ion mass, and c is the speed of light [30]. A full-velocity model is one that evolves all three components of the ion momentum equation, which is the second equation in 3.1.
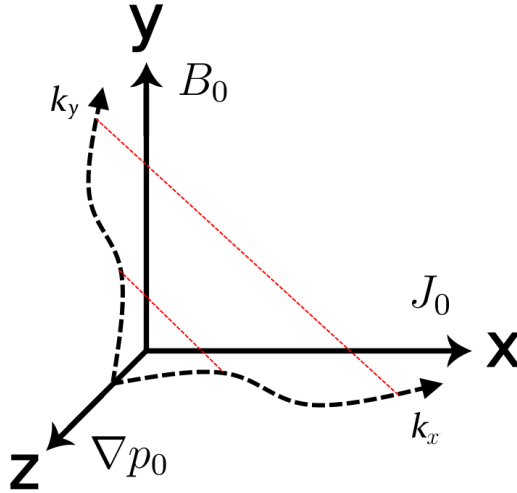
Figure 3.1: The geometry for the linearisation is quasi-3D with equilibrium pressure gradient, current density, and magnetic field that satisfy force balance. Perturbations are in x and y such that the total perturbation is at an angle to the magnetic field, B_0.

3.1.2 Geometry and linearisation

The two types of models will be compared by linearising them to obtain the dispersion relations, then solving for the instability growth rates and frequencies. Because the

dispersion relations are polynomials of complex frequency, Ω, there are multiple growth rates and frequencies for each system; it is the most unstable growth and corresponding frequency that is of interest for each system as it will dominate the linear growth phase.

For all linearisations, a quasi-3D, orthogonal coordinate system $(x\text{-}y\text{-}z)$ is defined such that the equilibrium magnetic field B_0 is in the y-direction, the equilibrium current density J_0 is in the x-direction, and the background pressure gradient ∇p_0 is in the z-direction; however, perturbations only have gradients in x and y consistent with a local approach, as detailed in figure 3.1.

The background pressure gradient is present to drive the drift-wave instability, and the background current density and magnetic field are provided to satisfy force balance. All perturbations are of the form $\tilde{f} = \exp\left[ik_x x + ik_y y - i\Omega t\right]$, where Ω is the complex frequency defined as $\Omega = \omega + i\gamma$ with γ as the growth rate and ω as the frequency. In the treatment that follows, it is assumed that the perpendicular vector potentials $\tilde{A}_x = \tilde{A}_z = 0$ and the parallel derivative operator acts along the perturbed field: $\nabla_\parallel f = \partial_\parallel f - \left[\dfrac{A_y}{B_0}, f\right]$.

3.2 Full velocity linearisation

Substituting the perturbed form for the fields into the equations given in 3.1 results in the following system.

$$
\begin{aligned}
-i\Omega \tilde{p} + \tilde{v}_z \nabla p_0 &= 0 \\
-i\Omega m_i n_e \tilde{v}_x + \frac{B_0}{c}\tilde{J}_z + ik_x \tilde{p}_e &= 0 \\
-i\Omega m_i n_e \tilde{v}_z - \frac{B_0}{c}\tilde{J}_x &= 0 \\
ick_x \tilde{\phi} + c\eta_\perp \tilde{J}_x - \frac{ick_x}{en_e}\tilde{p}_e + B_0 \tilde{v}_z - \frac{B_0}{en_e}\tilde{J}_z &= 0 \\
-i\Omega \tilde{A}_y - \frac{ick_x}{B_0 en_e}\tilde{A}_y + ick_y \tilde{\phi} + c\eta_\parallel \tilde{J}_y - \frac{ick_y}{en_e}\tilde{p}_e &= 0 \\
c\eta_\perp \tilde{J}_z - B_0 \tilde{v}_x + \frac{B_0}{en_e}\tilde{J}_x &= 0 \\
\tilde{J}_y - \frac{ck_x^2}{4\pi}\tilde{A}_y &= 0 \\
k_x \tilde{J}_x + k_y \tilde{J}_y &= 0
\end{aligned}
\tag{3.2}
$$
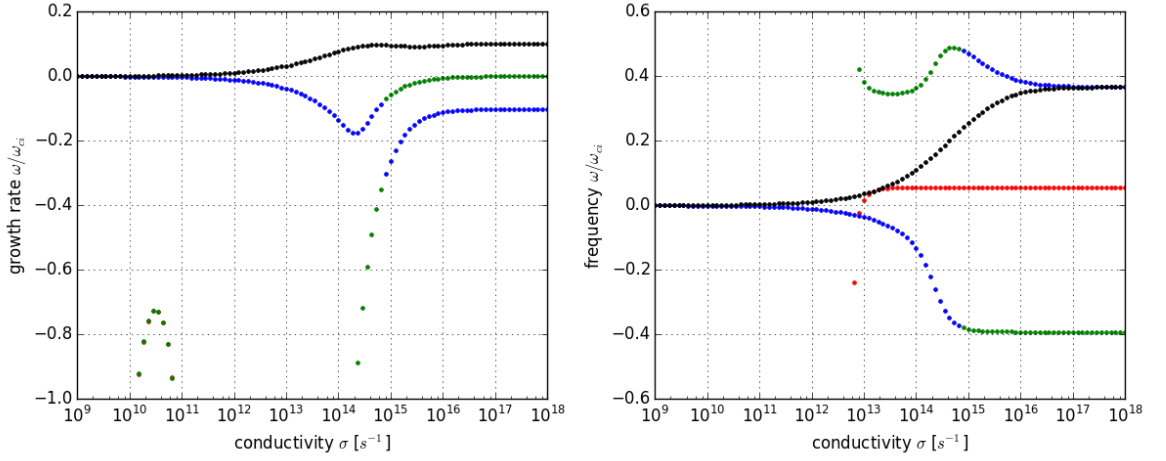
Figure 3.2: The solutions, both imaginary (growth rate in left plot) and real (frequency in the right plot), to the dispersion relation in equation 3.3 are shown. The black is the unstable solution and is is explored in more detail in figure 3.5. The blue, green, and red curves are all linearly stable solutions. The red curve is not shown on the growth rate plot because it is very large and negative.

This system is closed with eight variables and eight equations; therefore, it can be solved to produce a dispersion relation for the waves described by the system. The dispersion relation is

$$
\left(-\frac{\omega_{pi}^2}{2\pi\omega_{ci}^2}i\eta\right)\Omega^4 + \left(1 + \frac{v_A^2 k_y^2}{\omega_{ci}^2} - \frac{\omega_{pi}^2\omega_*}{2\pi\omega_{ci}^2}i\eta + \frac{\omega_{pi}^2 v_A^2\left(2k_y^2 + k_x^2\right)}{8\pi^2\omega_{ci}^2}\eta^2\right)\Omega^3
$$
$$
+ \left(\omega_* + \frac{v_A^2\omega_{pi}^2\left(4k_y^2 + k_x^2\right)}{4\pi\omega_{ci}^2}i\eta\right)\Omega^2 - \left(v_A^2 k_y^2\right)\Omega - \left(v_A^2 k_y^2\omega_*\right) = 0
$$

(3.3)

where ω_* is the drift-wave frequency, ω_{ci} is the ion cyclotron frequency, ω_{pi} is the ion plasma frequency, and v_A is the Alfvén speed. These are defined as

$$
\begin{aligned}
\omega_* &= \frac{\nabla p_0 k_z}{m_i n_0 \omega_{ci}} \\
\omega_{ci} &= \frac{eB_0}{m_i c} \\
\omega_{pi} &= \sqrt{\frac{4\pi n_0 e^2}{m_i}} \\
v_A &= \frac{B_0^2}{\sqrt{4\pi m_i n_0}}.
\end{aligned}
$$

(3.4)

The perpendicular resistivity is approximated to be twice the parallel resistivity, as given in Wesson [23]. The roots of this dispersion relation are shown in figure 3.2. These are calculated assuming reasonable tokamak parameters for magnetic field, pressure gradient, and background density within the tokamak pedestal ($B = 5 \times 10^3$G, $\nabla p =$

10^3Ba/cm, n_e = 10^{13}cm^{-3}, k_y = 0.04cm^{-1}, and k_z = 10cm^{-1}). The temperature varies with the conductivity via the Spitzer resistivity (inverse of conductivity):

$$\eta_S = \frac{2\sqrt{2\pi m_e}e^2 \ln \Lambda}{3T_e^{3/2}} \tag{3.5}$$

with the Coulomb logarithm approximated as $\ln \Lambda \simeq 14.9 - 0.5 \ln n_e + \ln T_e$ [23]. This relationship between conductivity and temperature allows the calculation of the ion mean free path in later sections.

Parallel Alfvén waves, resistive drift-waves, and cyclotron waves can be seen in the terms of the dispersion relation. The drift-wave should be the only unstable wave in the system (ie. the black dots in figure 3.2), though it is modified by the other stable waves. It is the growth rate and frequency of this unstable mode that is compared to the drift-reduced system in later sections.

3.3   Drift-reduced model

As discussed in chapter 1, an equation for vorticity is obtained by taking the curl of the momentum equation. It is convenient to take the parallel component of the vorticity equation, as shown in equation 3.6, because it includes the behaviour of the perpendicular velocities:

$$\varpi_\parallel = \varpi_y = \hat{b} \cdot \left(\vec{\nabla} \times \vec{v} \right) = \left(\frac{\partial v_x}{\partial z} - \frac{\partial v_z}{\partial x} \right) \tag{3.6}$$

where $\hat{x}$ and $\hat{z}$ are the perpendicular directions and $\hat{y}$ is parallel to the magnetic field line as shown in figure 3.1. Closing the system of equations then requires a relation between ϕ and $\varpi_\parallel$. An assumption is made that the perpendicular velocity is equal to the $\vec{E} \times \vec{B}$ velocity, giving $\varpi_\parallel = \nabla_\perp^2 \phi$. Simply taking the curl does not change the physics described by the equations - it is this assumption of the form perpendicular velocity where the differences between the full-velocity and drift-reduced system arise.

In the perpendicular vector potential equation, the fourth equation in the system in

3.2, the perpendicular velocity is found to be $v_z = -\dfrac{\nabla_x \tilde{\phi}}{B_0} - \dfrac{c}{B_0}\eta_\perp \tilde{J}_x + \dfrac{c}{B_0 e n_e}\nabla_x \tilde{p}_e + \dfrac{1}{en}\tilde{J}_z$. In this expression the first term is the $\vec{E} \times \vec{B}$ drift velocity, second term is due to resistive current, the third term is advection due to perpendicular pressure, and the final term is the Hall term. In the drift-reduced system, this velocity is simplified to include only the drift velocity resulting in the following set of equations:

$$
\begin{aligned}
-i\Omega\tilde{p} + \tilde{v}_z \nabla p_0 &= 0 \\
-i\Omega m_i n_e \tilde{v}_z - \frac{B_0}{c}\tilde{J}_x &= 0 \\
-i\Omega\tilde{A}_y - \frac{ick_x}{B_0 e n_e}\tilde{A}_y + ick_y\tilde{\phi} + c\eta_\parallel \tilde{J}_y - \frac{ick_y}{en_e}\tilde{p}_e &= 0 \\
ick_x\tilde{\phi} + B_0\tilde{v}_z &= 0 \\
\tilde{J}_y - \frac{ck_x^2}{4\pi}\tilde{A}_y &= 0 \\
k_x\tilde{J}_x + k_y\tilde{J}_y &= 0
\end{aligned}
\tag{3.7}
$$

By reducing the expression for the perpendicular velocity to only $\vec{E} \times \vec{B}$ drift, the dependence on $\tilde{J}_z$ and $\tilde{v}_x$ is removed, reducing the number of required equations for closure. Though the vorticity does not explicitly appear in equations 3.7, an expression for vorticity ($\tilde{\varpi}_y = ik_x\tilde{v}_z$) can be easily obtained by substituting the final equation ($\tilde{J}_z = \dfrac{k_y}{k_x}\tilde{J}_y$) for $\tilde{J}_z$ in the second (ion momentum):

$$
-\left[ik_x\tilde{v}_z\right]\Omega m_i n_e + \frac{B_0 k_y}{c}\tilde{J}_y = 0
\tag{3.8}
$$

This simplified model in equations 3.7 can then be solved to render the dispersion relation:

$$
\Omega^3 + \left(\omega_* + \frac{v_A^2 k_x^2 \omega_{pi}^2}{4\pi\omega_{ci}^2}i\eta\right)\Omega^2 - \left(v_A^2 k_y^2\right)\Omega - \left(v_A^2 k_y^2 \omega_*\right) = 0
\tag{3.9}
$$

The full solution (all three roots) of the dispersion relation are plotted in figure 3.3, where it is clear that, similar to the full-velocity system, only one of the solutions is unstable ($\gamma > 0$).
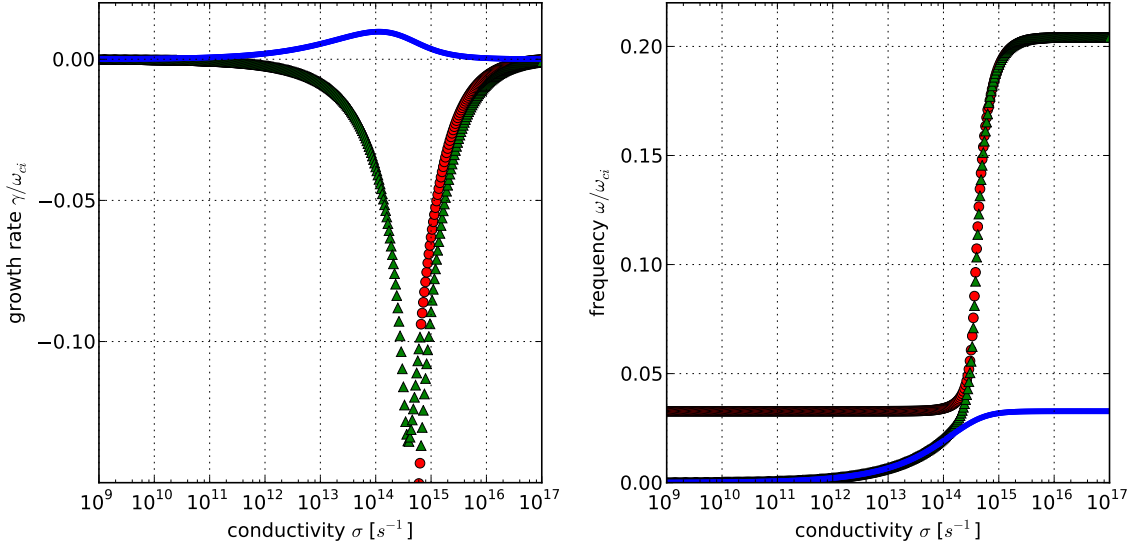
Figure 3.3: Growth rate (left) and frequency (right) solutions to the dispersion relation, equation 3.3. Because it is an order 3 polynomial in complex frequency, Ω, there are three solutions. Two of these solutions are stable (red circles and green triangles), while one is unstable (blue dots) with a positive growth rate. All frequencies and growth rates are normalised to the cyclotron frequency.

3.4   Comparing the dispersion relations

The two dispersion relations, equations 3.3 and 3.9, are identical when the Ω^4 term, the last three terms in Ω^3, and the parallel wave number in the second term of the Ω^2 are neglected, indicating that these terms contain the physics lost in the drift-reduction. Figure 3.4 shows the most unstable growth rate and corresponding frequency plotted with the drift-reduced dispersion solution for parameters chosen specifically to highlight the area of largest difference between the models ($B = 0.45$T and $n = 10^{19}$m^{-3}). The full-velocity growth rate remains unstable to infinite conductivity (zero resistivity), while the drift-reduced growth rate stabilises. This can be explained by setting $\eta = 0$ in the dispersion relations, at which point they become identical except for an extra term: $\frac{v_A^2 k_y^2}{\omega_{ci}^2}\Omega^3$. This Alfvén mode modifies the drift-wave growth rate to be unstable even at zero resistivity.

This is a significant difference between the two models, but importantly it occurs where the plasma is collisionless as indicated by the dotted green line in figure 3.4, which marks the conductivity corresponding to the mean free path, $\lambda_{mfp} = 100$cm. This is calculated by assuming Spitzer resitivity (equation 3.5) to find the temperature, and then using the temperature and density to calculate the mean free path:
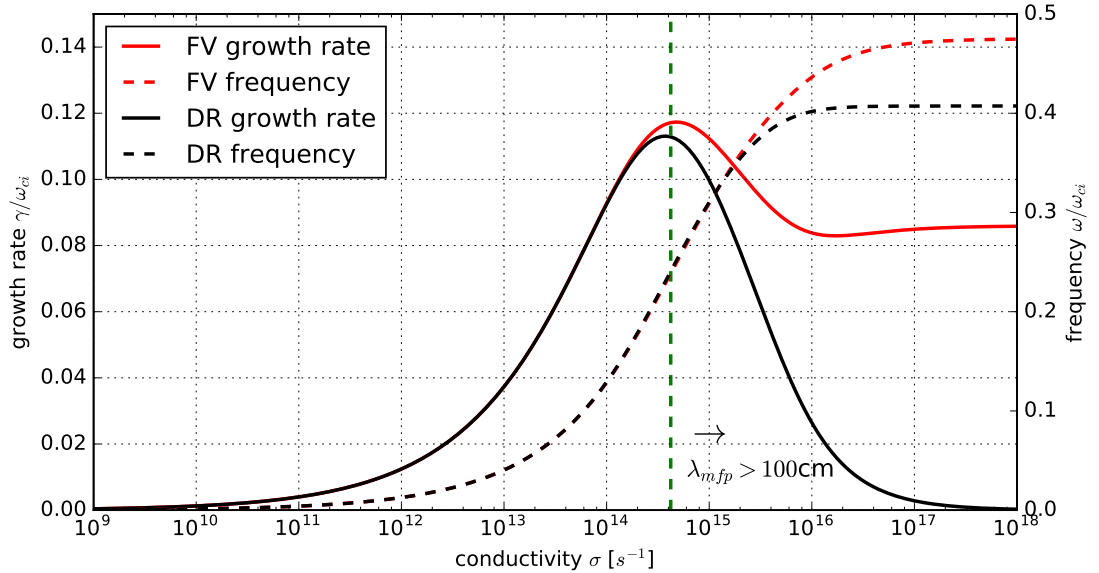
Figure 3.4: The most unstable solution to the dispersion relations for drift reduced and full velocity models in equations 3.3 and 3.9, respectively. At this particular location in parameter space, the full velocity solution is significantly more unstable at high conductivity than the drift-reduced solution. The frequencies and growth rates are normalised to the ion cyclotron frequency, ω_{ci}. The dotted green lines indicate the location of $\lambda_{mfp} = 100$cm, which is the order of magnitude at which a tokamak plasma transitions between collisional/collisionless regimes. To the right (ie. towards higher conductivity) the plasma is collisionless, therefore the fluid approximation is insufficient in describing the plasma.

$\lambda_{mfp} = v_{th}\tau_i$ where v_{th} is the ion thermal velocity and τ_i is the ion collision time given in equation 1.8. The condition for a collisional plasma is $\frac{\lambda_{mfp}}{L} < 1$, where L is the system scale, and since present-day tokamaks have a minor radius on the order of 100cm this line marks the transition from low to high collisionality. As mentioned previously, the fluid approximation is only valid at high collisionality, therefore this main difference between the two models lies in a region of parameter space where both models are insufficient descriptions.

To explore these differences in detail, the dispersions are evaluated in a large area of parameter space. It is useful to define a parameter called the electron beta, which is the ratio of electron pressure to magnetic pressure, to examine the behaviour of the two systems since this is often used to describe the overall plasma performance in both theory and experiment.

$$\beta_e = \frac{p_{\text{gas}}}{p_{\text{mag}}} = \frac{8\pi n T_e}{B^2} \tag{3.10}$$
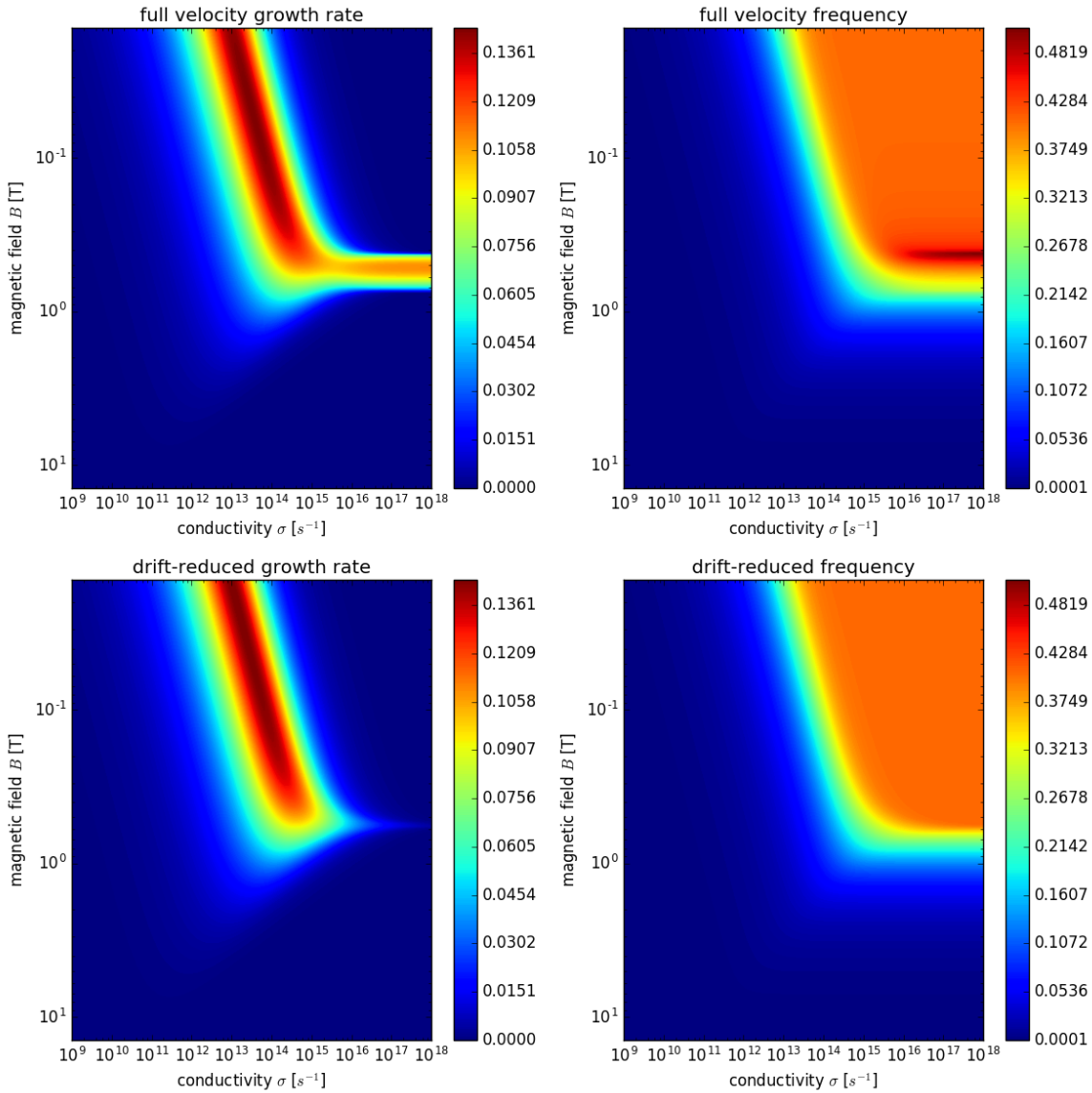
Figure 3.5: Full velocity and drift-reduced growth rates and frequencies as a function of conductivity and magnetic field at $n = 10^{18} \text{cm}^{-3}$. The y-axis is descending in magnetic field, indicating an increasing electron beta according to equation 3.10. Growth rates and frequencies are normalised to the ion cyclotron frequency, ω_{ci}.

In figure 3.5 the density is set to constant $n = 10^{19} \text{m}^{-3}$ and the magnetic field is scanned such that the electron beta, $\beta_e \in [10^{-6}, 10^0]$. This is useful to do because the terms in equations 3.3 and 3.9 are not functions of only β_e - they depend on various combinations of density and magnetic field. In essence, the parameter space is >3 dimensional, however this is not easily visualised so density has been held constant for illustrative purposes.

To compare the growth and frequency of the unstable modes described by these dispersions, the percentage difference between the two results are plotted in figure 3.6. Assuming the full velocity model is more accurate, this then equates to the error in

the drift-reduced model. Because the parameter space is multi-dimensional, there are multiple similar plots shown (figures 3.6 and 3.7), but with different axes to analyse the parameter dependency independently. Figure 3.6 depicts the percent difference in growth rates and frequencies between the full-velocity and drift-reduced systems as given by

$$\Delta_\% = \left| \frac{f_{FV} - f_{DR}}{f_{FV}} \right|. \tag{3.11}$$

where f can either be the frequency or the growth rate. The density held constant at $n = 10^{19} \mathrm{m}^{-3}$ in the top plots and magnetic field held constant at $B = 1\mathrm{T}$ in the bottom plots of figure 3.6.

It is expected that at high magnetic field the drift-reduction will be an accurate approximation for the plasma behaviour since the Larmor radius becomes very small and the cyclotron frequency becomes very large consistent with the assumptions. Figures 3.6a and 3.6b confirm this expectation, revealing a low and decreasing percentage error between the two models as the magnetic field increases. Note that the magnetic field axis on these plots is in descending order so that the electron beta is ascending across all plots. Interestingly, as the magnetic field decreases the error is not seen to monotonically increase, but instead there are regions of low error even at low magnetic field.

Examining figures 3.6c and 3.6d in which the density is varied holding $B = 1\mathrm{T}$ constant, it is seen that at low density there is a mostly universal disagreement between the models with an error of $> 10\%$ across a wide range of conductivity. All of the additional (extra physics) terms in the full velocity dispersion relation, equation 3.3, vanish at low density except for the second term of the Ω^3 order, $\frac{v_A^2 k_y^2}{\omega_{ci}^2}$ which is proportional to n^{-1}. At low density and high conductivity this term dominates, but as conductivity is lowered, the η^2 term takes over, thus the small area of agreement even at low density.

Since the mean free path is inversely proportional to density, the green line indicating the collisionality regime change is not constant in conductivity for figures 3.6c and
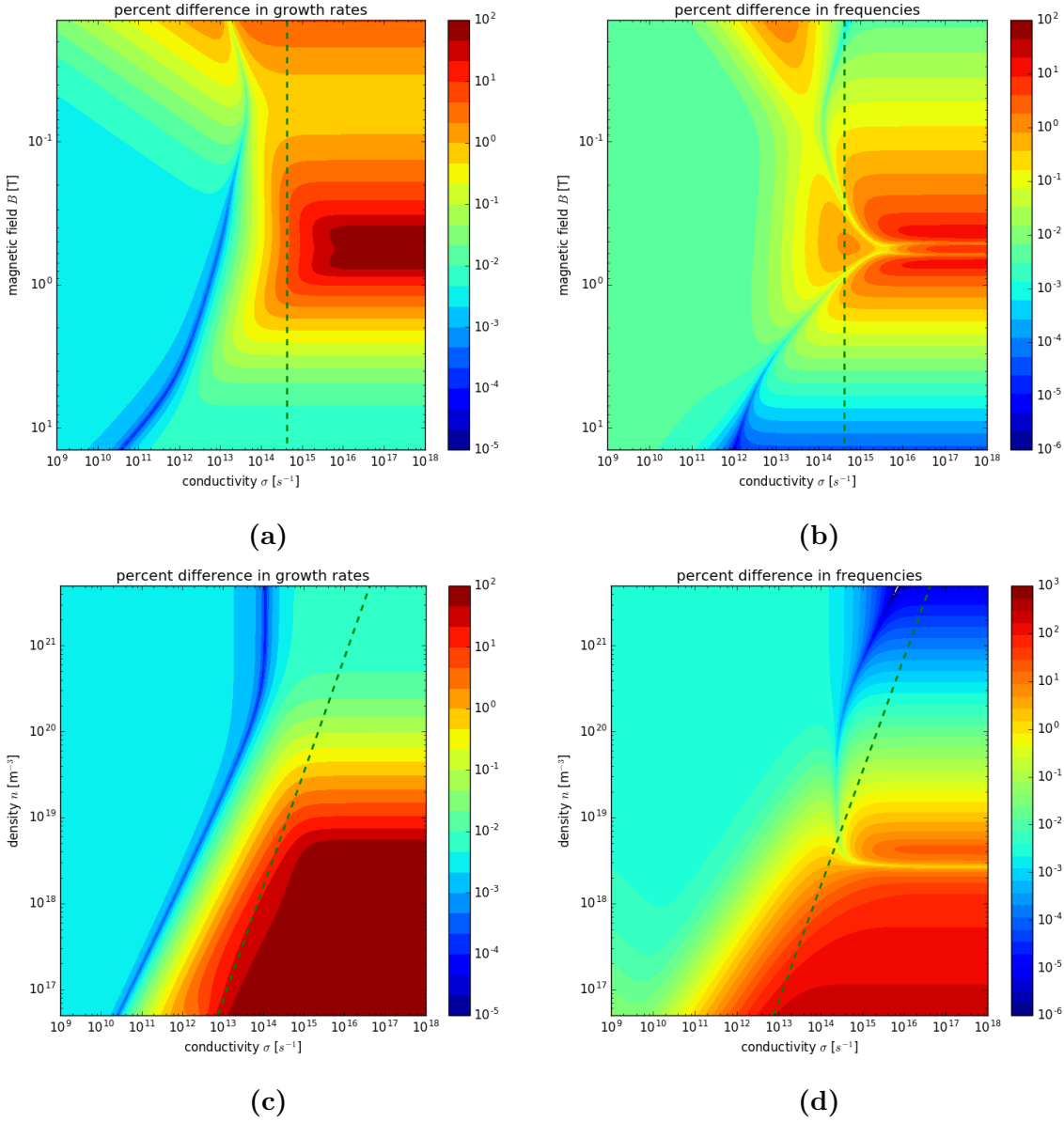
Figure 3.6: The percentage differences, calculated by equation 3.11, are shown as a function of conductivity, magnetic field, and density. The magnetic field is varied, with the density held at $n = 10^{18}\mathrm{m}^{-3}$, resulting in the percentage difference between the two models for (a) growth rate and (b) frequency. The magnetic field is then held constant at $B = 1\mathrm{T}$ and the density is varied giving the percentage differences between the two models for (c) growth rate and (d) frequency. The dotted green lines indicate the location of $\lambda_{mfp} = 100\mathrm{cm}$, which is the order of magnitude at which a tokamak plasma transitions between collisional/collisionless regimes. To the right (ie. towards higher conductivity) the plasma is collisionless, therefore the fluid approximation is insufficient in describing the plasma.

3.6d. As the density decreases, a plasma becomes less collisional, making the fluid approximation inapplicable in these regions. In all the plots in figure 3.6, the largest areas of disagreement are in the collisionless regime, though there are some areas of meaningful disagreement even in a collisional plasma.

While it is useful to analyse the percentage differences between the models to see the relative agreement between them, it is also worth studying the absolute differences between the models. If both models indicate a very small growth rate, but one is still much larger than the other, this will result in a large percentage difference, but the impact and importance of this difference is minimal due to the overall negligible growth rate. Figure 3.7 illustrates the absolute differences between the models, similarly to figure 3.6 with magnetic field and density varied independently. From these it is clear that the drift-reduced model breaks down significantly at low density, and also at high conductivity for a narrow band of magnetic fields around 0.5T. As $\lambda_{mfp} \propto n_e^{-1} T_i^2 \sim n_e^{-1} \sigma^{4/3}$, these regions of low density and high conductivity, where the most significant absolute errors arise, correspond to collisionless plasmas.

An important question to answer, then, is where within a tokamak the drift-reduced model is an acceptable approximation for the the full velocity description. The edge is lower density than the core, but also lower conductivity, so where does the drift-reduce model break down? The analysis so far has been based on parameters chosen for an example case with constant pressure gradient and independently varying magnetic fields and densities. The true plasma behaviour consists of simultaneous variations in many parameters, so to answer this question it is necessary to reduce the number of free parameters as much as possible by examining experimental data.

3.5   Tokamak relevance

The parameter space in which tokamaks operate is specific to the region within the tokamak (core, pedestal, and edge) and the particular tokamak in question. For a large tokamak such as JET, the Joint European Torus at the Culham Science Centre, the core operates around $\beta_e = 0.03$ and $\sigma = 10^{15} \text{s}^{-1}$, while in the edge $\beta_e = 0.005$
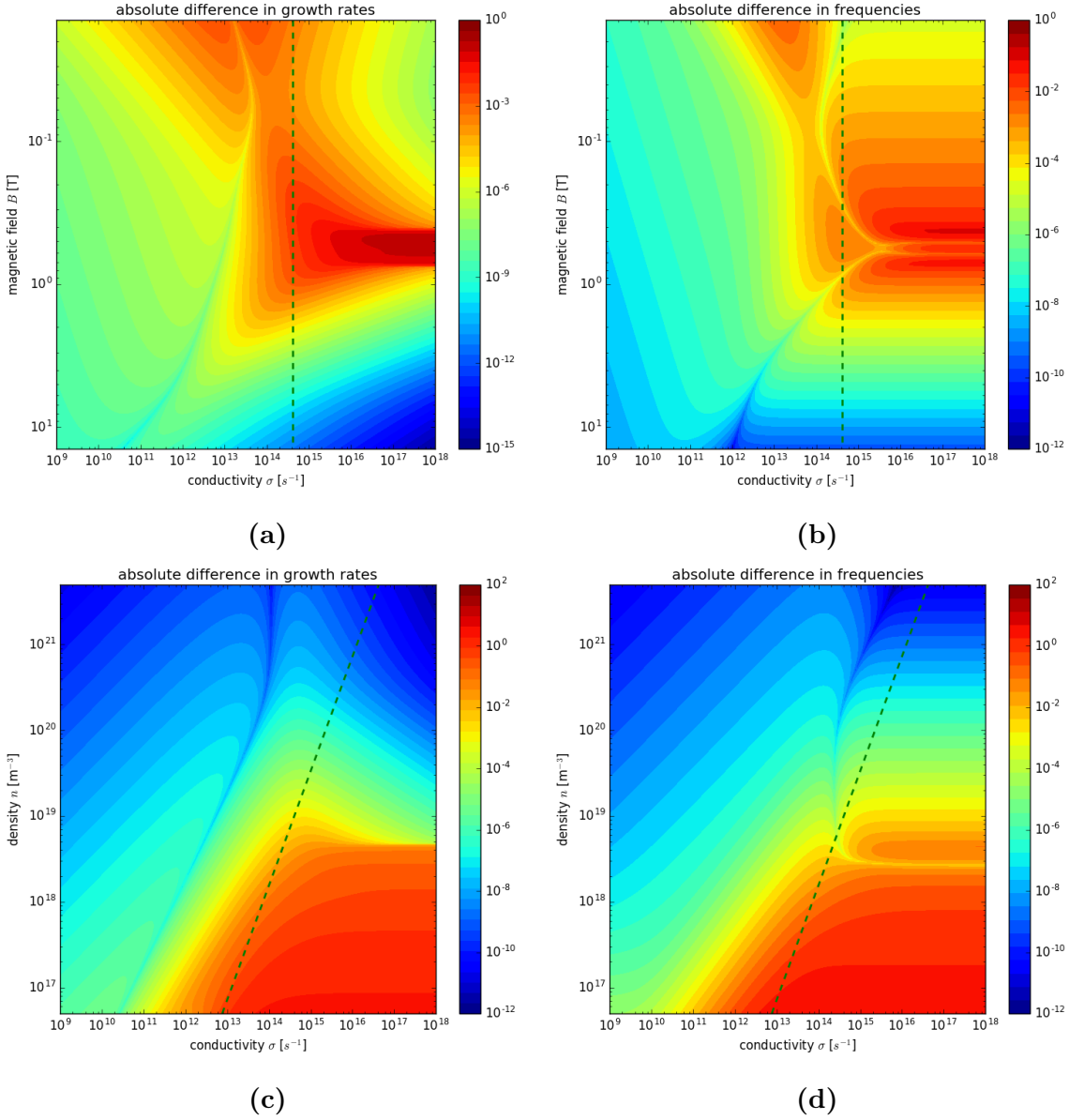
Figure 3.7: The absolute differences are shown as a function of conductivity, magnetic field, and density with the growth rates and frequencies normalised to the ion cyclotron frequency. The magnetic field is varied, with the density held at $n = 10^{18}\text{m}^{-3}$, resulting in the difference between the two models for (a) growth rate and (b) frequency. The magnetic field is then held constant at $B = 1\text{T}$ and the density is varied giving the differences between the two models for (c) growth rate and (d) frequency. The dotted green lines indicate the location of $\lambda_{mfp} = 100\text{cm}$, which is the order of magnitude at which a tokamak plasma transitions between collisional/collisionless regimes. To the right (ie. towards higher conductivity) the plasma is collisionless.

and $\sigma = 10^{12}s^{-1}$. These are estimations, so to determine how well the drift-reduced model can describe the core and edge of JET, actual experimental data is examined. The following analysis universally applies to any tokamak, and can be done providing density, temperature, and magnetic field are known.

3.5.1 Analysis with JET data

Using the Thomson scattering system on JET [104], density and temperature radial profiles at the mid-plane have been acquired for shot 87045. The time trace of the density and temperature in the core are shown in the top plot of figure 3.8, which indicates two regimes of interest: L-mode and H-mode (black and green, respectively, vertical dotted lines). Some parameters are then calculated from these profiles, such as the resistivity (assumed Spitzer [30]) and the Coulomb logarithm. Due to the constraints the experimental data provide, the only assumed values in the analysis are the parallel and perpendicular wave numbers $k_y = 0.03\text{cm}^{-1}$ and $k_z = 10.0\text{cm}^{-1}$, which have been chosen based on experimental and theoretical values [105]. By solving the dispersion relations for each system the percentage error between the two models is compared in the bottom right plot of figure 3.8.

A slightly different behaviour is seen for the actual JET data compared to the more general results, mostly due to the pressure gradient having a profile instead of being held constant. In the deep core, the pressure gradient approaches zero as the pressure reaches a maximum, reducing the drift-wave drive to nearly zero, stabilising both models, and giving very good agreement between the two. The edge, which is lower in density and higher in pressure gradient, is where the main error is seen to arise. The difference in growth rates between the models, $\Delta_\%$, increases to 0.4% and 1.7% for L-mode and H-mode, respectively - peaking at the far edge.

The L-mode analysis shows lower disagreement between the drift-reduced and full-velocity systems than the H-mode, remaining under 0.4% across the entire plasma profile. Note that the peak disagreement occurs at the same radial location as the peak growth rate. The error in the frequencies exhibits the exact same qualitative
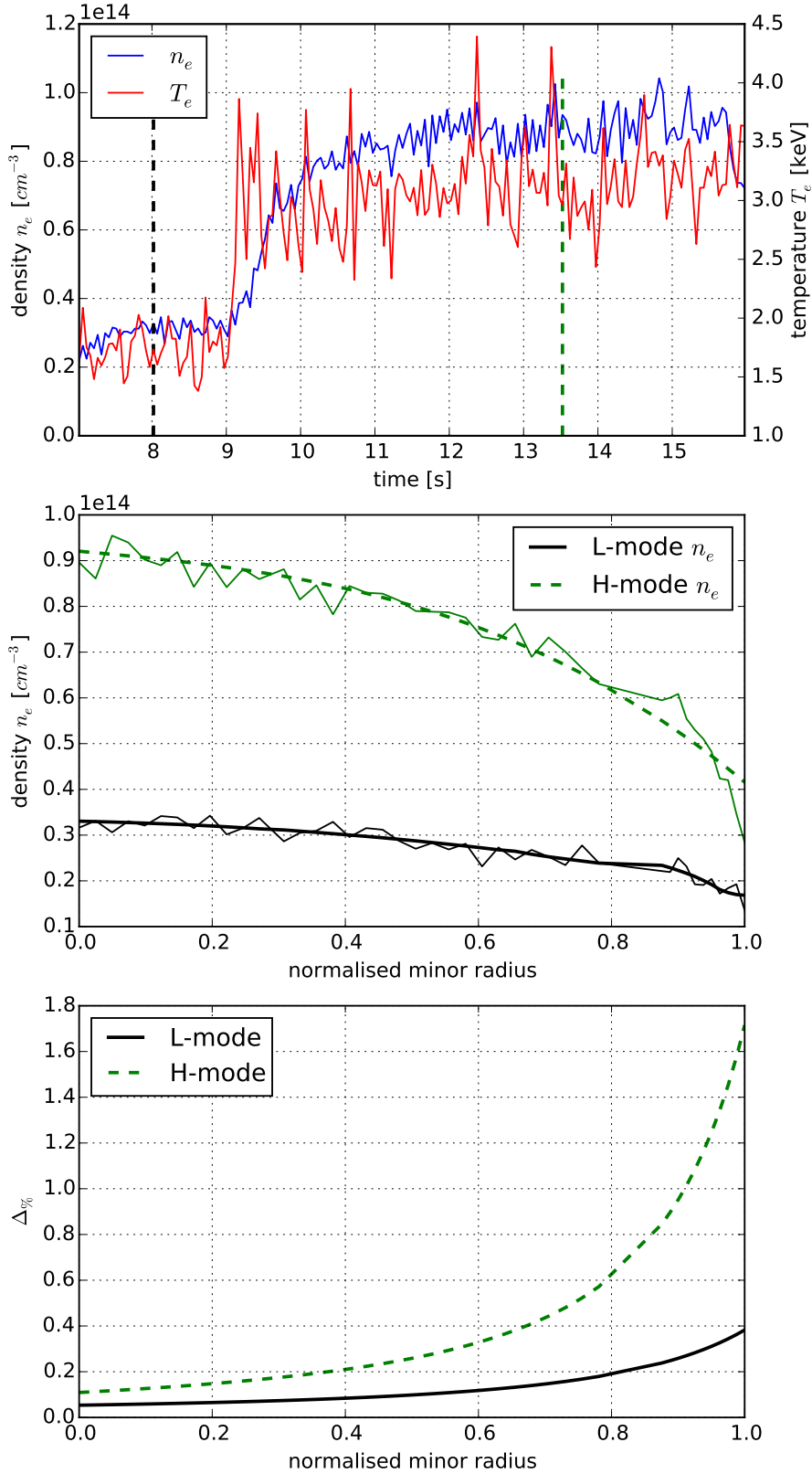
Figure 3.8: Thomson scattering data from JET (shot 87045) is used to calculate how well the drift-reduced model describes the linear drift-wave growth rate. A time trace (top) of the core density and temperature is shown with vertical lines marking the L-mode (black) and H-mode (green) that are investigated individually. Density profiles show increase in confinement (ie. core density) and development of the pedestal (middle). The error between drift-reduced and full-velocity model growth rates is shown (bottom) to be a function of the radial position within the plasma, where the far edge and deep core are shown to be most accurate.
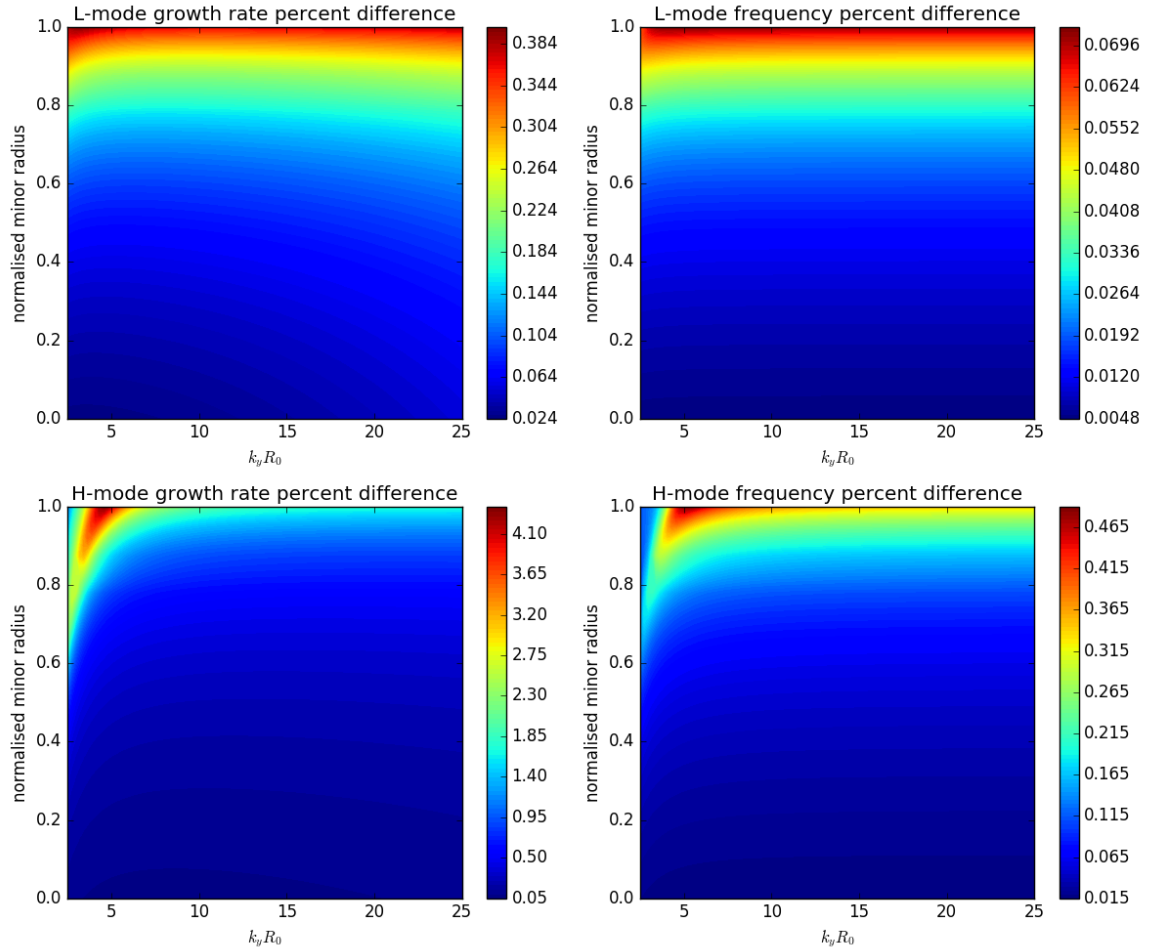
Figure 3.9: The percentage error in growth rate and frequency between the drift-reduced and full-velocity models is shown to depend on the ratio of parallel to perpendicular wave number for the drift-wave instability as well as normalised radius. A clear peak in error exists for a particular, low $k_y R_0$.

behaviour as the growth rate error, but with nearly ten times the accuracy. The maximum error in the frequency is 0.4% in H-mode compared to 4% for the growth rate.

Even when constrained by the JET data, the accuracy of the drift-reduction is sensitive to the remaining free parameters: the ratio of the parallel and perpendicular wavelengths of the drift-instability. Holding the perpendicular wave number constant at $k_z = 10\text{cm}^{-1}$ [105] and scanning the parallel wave number across a reasonable domain $k_y R_0 \in [5, 25]$, an interesting feature emerges - a peak in disagreement between the models around $k_y R_0 = 5$ in H-mode and $k_y R_0 = 2$ in L-mode. The parallel wavelength can be defined as $\lambda_y = 1/k_y = L_c/n$ where n is the toroidal mode number of the drift-wave and L_c is the connection length determined by the geometry and magnetic topology. This indicates that for a given tokamak, high mode number drift-waves will be represented more accurately by the drift-reduced model than those with low toroidal mode numbers, while accuracy is again recovered at very low mode number.

It is important to note that this analysis has been done on core HRTS data for JET, all of which is better represented by a kinetic description due to the low collisionality. Fluid models are more suited for the edge plasma region where the temperature and density are both low ($n_e \sim 10^{19}\text{m}^{-3}$ and $T = 1 - 100\text{eV}$).

3.6 Conclusion

Drift-reduced models provide simplified dispersion relations for more succinct analytics, and the exclusion of fast waves allows for larger time steps leading to faster simulations, so these models are an important subset of the full fluid description. The validity of these models has been tested for a simple quasi-3D slab resulting in drift-wave linear growth rates and frequencies that only agree with the full-velocity fluid description in specific regions of parameter space. Though the worst agreement lies outside of the validity of the fluid description (ie. low collisionality), there is still some meaningful disagreement in areas where the fluid model does apply.

When discussing the validity of drift-reduced models, it is necessary to consider the

non-linear behaviour in addition to the linear. In the basic slab geometry investigated here, the linear differences are directly related to the non-linear saturated turbulent transport and growth times. The relationship between drift-wave linear and non-linear behaviour and mode structure in a more realistic *sheared* magnetic field is discussed in detail by Scott [106], and it is concluded that the non-adiabaticity of drift-waves is affected and usually enhanced by the non-linearities. This then drives the drift-waves further unstable, at which point the growth from the linear phase is irrelevant to the behaviour of the turbulence. That is not to say the linear growth rates do not play a role in the initial development of the turbulence. In figure 3.5 it is apparent that for conductivities greater than $10^{13}\omega_{ci}^{-1}$ and magnetic field, $B \in [0.5, 1.0]$, which corresponds to parts of a tokamak operating regime, the full velocity fluid model dictates that drift-waves are highly unstable whereas the drift-reduced model places them near marginal stability. It is not unreasonable, then, to assert that the linear and non-linear behaviours are highly correlated in this region, since in the drift-reduced case the modes can be easily stabilised preventing altogether the development of turbulence. Once the non-linear turbulence is established, however, it is self-sustaining even if the linear modes are then stabilised [106]. It is important when choosing a fluid model to use for tokamak plasma simulations to identify the parameter space in which the simulation will be operating as to identify whether a drift-reduced model is appropriate or if a more accurate, full-velocity model should be used instead. The analysis performed in this chapter exemplifies the analysis that should always be done to check the accuracy of a simplified fluid model before its use.

Chapter 4

Large eddy simulation for plasma turbulence modelling

4.1 Introduction

Fluid turbulence is a phenomenon observable in many fields of physics from aerodynamics to plasma physics. With no analytical solution to the fluid equations, it is essential to simulate turbulence to understand and predict a fluid's behaviour. One of the fundamental properties of turbulence is the large range of length scales over which structures form and energy is injected and dissipated. This can be seen in figure 4.1, which shows a typical energetic cascade associated with turbulence, which is made of three ranges: the energy containing range, the inertial sub-range, and the dissipation range [107]. In general, energy is injected into the system at large scales and is then transferred to smaller scales via non-linear processes. This continues until the Kolmogorov micro-scale is reached (in the dissipation range), at which point the viscosity dominates and the energy is dissipated as heat. These diverse length scales pose a problem for efficient computational simulation because large length scales must be resolved at very high resolution in order to cover the entire scale range, creating a computationally intractable problem.

This issue has been addressed previously with the development of large eddy simulation (LES) - a technique that involves resolving the large scales and modelling the dissipation associated with the small scales without actually resolving them [108–110].
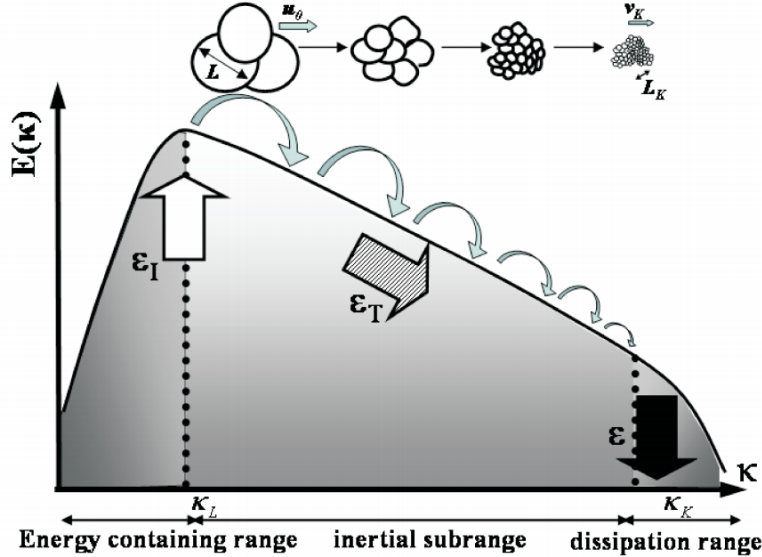
Figure 4.1: The energy spectrum for typical turbulence demonstrates a cascade from large to small scales. The y-axis is energy and the x-axis is $\log(k)$ where k is the spatial wave number of the turbulence [107]. The cartoon at the top gives an indication of the relative size of the turbulent eddies.

The challenge, then, is devising appropriate and accurate models for the small, unresolved scales. Many such models have been derived and used [111–113] over the past few decades for meteorological and fluid simulations, all of which are rigorous to a point but finally based on heuristic arguments. There has also be more recent effort to further develop these for plasma turbulence simulations [30, 114]. Four of these dissipation models will be tested here: viscosity, hyperviscosity, Smagorinsky, and the CENTORI model [30]. There are more complex and rigorous sub-grid (i.e. below the grid resolution scale) dissipation models than these four, however these are often used due to their simplicity to implement and computational efficiency. The most rigorous LES models, termed dynamic models, are very complex and involve the evolution of a separate model from the main fluid code [115–117]. This can be very time consuming, often taking as long as a full resolution fluid simulation defeating the purpose of LES. It is therefore simpler and more practical to implement the models that are investigated herein, since the focus is on the plasma physics of the resulting full simulation.

4.1.1 Method for comparison

The implementation of the LES models is straightforward due to the flexibility of BOUT++ [68] making it an ideal test bed for this study. These LES models will each be applied to the Hasegawa-Wakatani drift-wave turbulence model described in section

4.2. To do this, a high resolution reference simulation is first run that resolves all relevant length scales for the turbulence. In this way, the simulation results are the accurate solution (to second order) of the set of equations, which is then used as a reference against which the LES implementations can be compared. Simulations are then run with lower resolutions, such that the small scales are not resolved, and the LES dissipation models are included in an attempt to recover the previously obtained reference results. The comparisons are made by examining key turbulent characteristics and parameters - the energy, enstrophy, 'radial' (in the same direction as the background density gradient) and 'poloidal' (perpendicular to the background magnetic field and density gradient) fluxes, and the spatial spectra for density, vorticity, and potential. Due to the chaotic nature of turbulence, minor differences due to the LES models will cause the density, vorticity, and potential to evolve differently, so direct comparison of these fields is not useful and the spectra are used instead. Time traces of the fluxes, energy, and enstrophy are compared to investigate both the linear/non-linear evolution and the saturation values.

4.2 Turbulence model

The Hasegawa-Wakatani (H-W) equations form a 2D model (x and z) for drift-wave turbulence with non-adiabatic electrons, a homogeneous magnetic field $B = B_0\hat{y}$, and inhomogeneous density $n(x, z)$ [118]. It is one of the simplest models that can be used to describe drift-wave turbulence and is therefore a useful test case for exploring the effects of large eddy dissipation models. The domain is a periodic slab where x and z are the coordinates and both are perpendicular to the magnetic field, B_y.

4.2.1 The equations

The two Hasegawa-Wakatani equations are expressed as

$$
\begin{aligned}
\frac{\partial \varpi}{\partial t} &= -\{\phi, \varpi\} + \alpha\left(\phi - n\right) + \nu_\varpi \nabla^2 \varpi \\
\frac{\partial n}{\partial t} &= -\{\phi, n\} + \alpha\left(\phi - n\right) - \kappa\frac{\partial \phi}{\partial z} + \nu_n \nabla^2 n
\end{aligned}
\tag{4.1}
$$

with vorticity $\varpi = \nabla^2\phi$, number density n, plasma electric potential ϕ, adiabaticity parameter $\alpha = \dfrac{T_e \nabla_\parallel^2}{\eta n_0 \omega_{ci} e^2}$, drive coefficient $\kappa = -\dfrac{\partial}{\partial x}\ln(n_0)$, and viscosities ν_ϖ and ν_n. The curly brackets are Poisson brackets, with the definition

$$\{a, b\} = \left(\frac{\partial a}{\partial x}\frac{\partial b}{\partial z} - \frac{\partial a}{\partial z}\frac{\partial b}{\partial x}\right). \tag{4.2}$$

The H-W model is a fluid model useful for simulation of drift-wave turbulence because it is fairly simple, therefore fast computationally, but still includes resistivity to destabilise drift waves. It is related to the fluid model described in section 1.3.1, but with several key simplifications - it is drift-reduced, neglects temperature perturbations, approximates parallel dynamics through the adiabaticity parameter, the magnetic field is homogeneous, and the perturbations are electrostatic. The terms $\nu_\varpi\nabla^2\varpi$ and $\nu_n\nabla^2 n$ in the H-W model, equations 4.1, are standard viscosity terms that provide a base dissipation level due to collisional friction. Including extra dissipation for LES is accomplished by simply adding more dissipation terms to these equations, as will be discussed in section 4.3.

4.2.2 Turbulent behaviour

The qualitative characteristics of turbulence were described in detail in chapter 1 and 4.1. The following sections will go through the results of the reference simulation and explore the behaviour of this turbulence model through the energy cascade, field structures, time evolution, the effect of varying the model parameters κ and α, and finally the effect of changing the resolution. The reference simulation was run for $1000\omega_{ci}^{-1}$ with a resolution of about 10 points per ρ_i, with $\kappa = 0.1$ and $\alpha = 1.0$, and with normalised viscosities $\nu_n = \nu_\varpi = 0.001$ (these values are discussed in more detail in section 4.4). There is no extra LES dissipation present in the reference case. The boundary conditions are periodic in both spatial dimensions.

4.2.2.1 Density, vorticity, and potential

The simulation is initialised with a mix of mode numbers with pseudo-random phases and eventually develops into saturated turbulence after about $200\omega_{ci}^{-2}$. The initial and

final ($t=1000\omega_{ci}^{-1}$) density perturbations as well as the final potential and vorticity are shown in figure 4.2. The final density perturbations have a decreasing trend in x
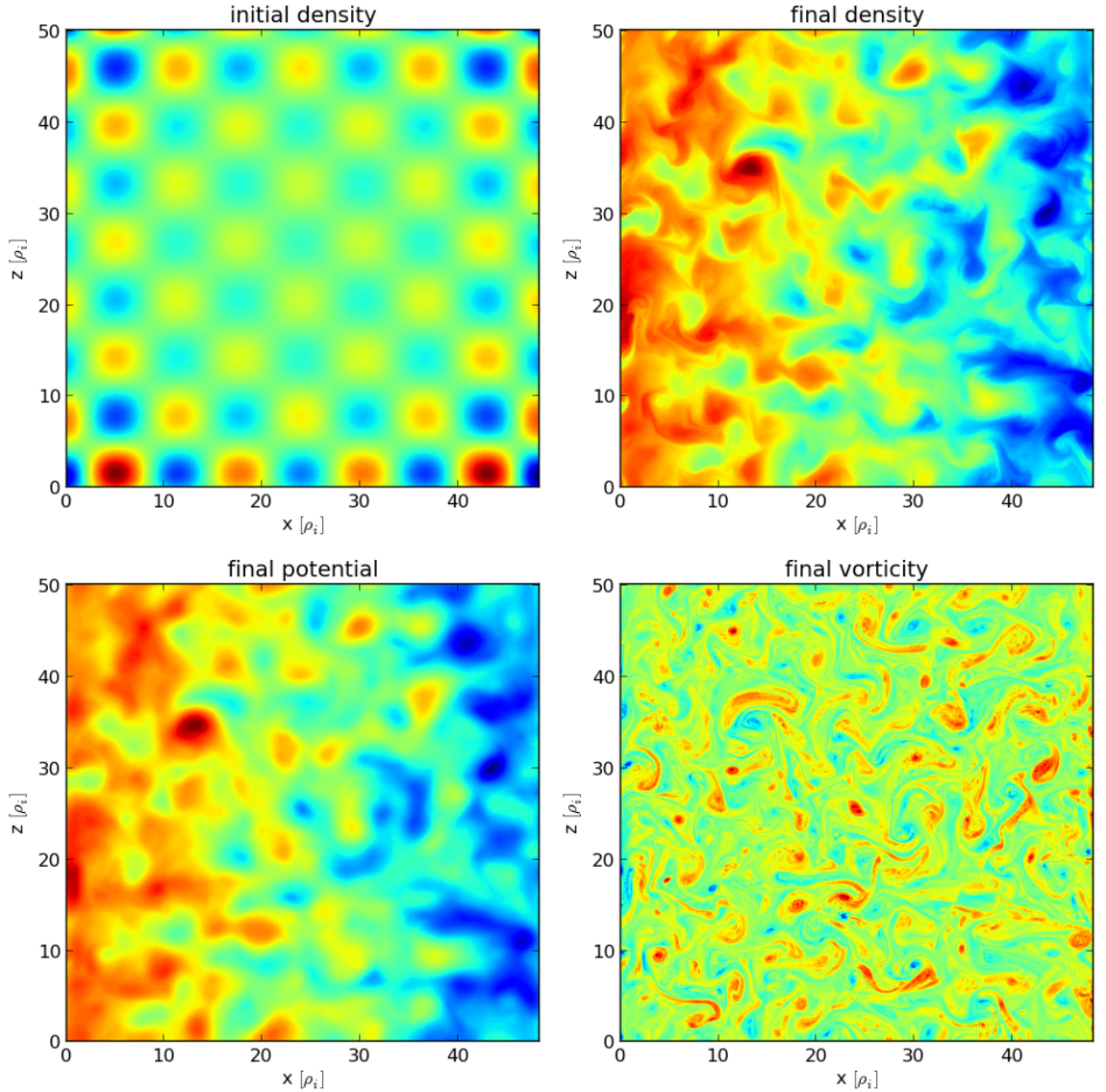
Figure 4.2: The initial (top left) and final (top right) density perturbations, final potential (bottom left), and final vorticity (bottom right) resulting from the reference (dx$\approx$ $0.1\rho_i$) Hasegawa-Wakatani simulation.

due to the underlying density gradient being positive - the perturbations attempt to relax the background profile. The structure of the density and electrostatic potential are very similar, however, the vorticity structures have a visibly smaller wavelength. These results are consistent with those found in other Hasegawa-Wakatani simulations [42,118,119], providing confidence that these can be used as the reference case for the LES study.

85

4.2.2.2 Turbulent cascade and energy

The energy of the system is conserved and is defined as

$$E = \frac{1}{2} \iint \left(n^2 + |\nabla \phi|^2 \right) \, \mathrm{d}x\mathrm{d}z \qquad (4.3)$$

where the integral is over the entire spatial domain, and the energy is comprised of a normalised thermal term (first) and kinetic term (second). This can be calculated at every time step to obtain figure 4.3 which shows the energy evolution as a function of time. The saturation of the turbulence can clearly be seen at around t=$200\omega_{ci}^{-1}$, at which point the energy saturates and oscillates about a constant value. This increase in energy is due to the initial density configuration being fed energy from the background gradient until turbulence forms and saturates - at which point energy in the system is constant due to a balance of the source (free energy from density gradient) and sink (small scale viscous dissipation). The turbulent cascade described in section 1.3.4, can indeed be seen in figure 4.3 as expected.
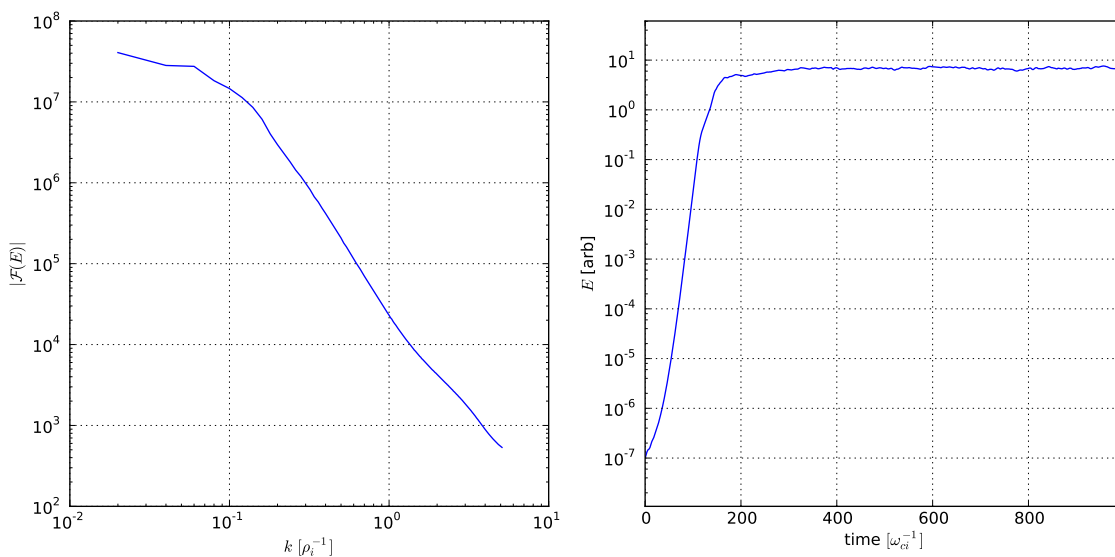
Figure 4.3: The energy cascade (left) and time trace (right) for the Hasegawa-Wakatani system in the reference case appear as expected. The energy grows and then oscillates about a constant value after a time, once the turbulence has saturated.

4.2.2.3 Effect of κ and α

A choice of α and κ can be made to exhibit behaviour consistent with particular regimes of turbulence. The adiabaticity parameter, α, is the ratio of the parallel diffusion rate

and the drift frequency - in the limit of $\alpha \to \infty$ (collisionless plasma) electrons become adiabatic as their motion is unimpeded along field lines. In the limit of $\alpha \to 0$ the electrons are slow to respond to potential fluctuations, leading to a decoupling of the HW equations.
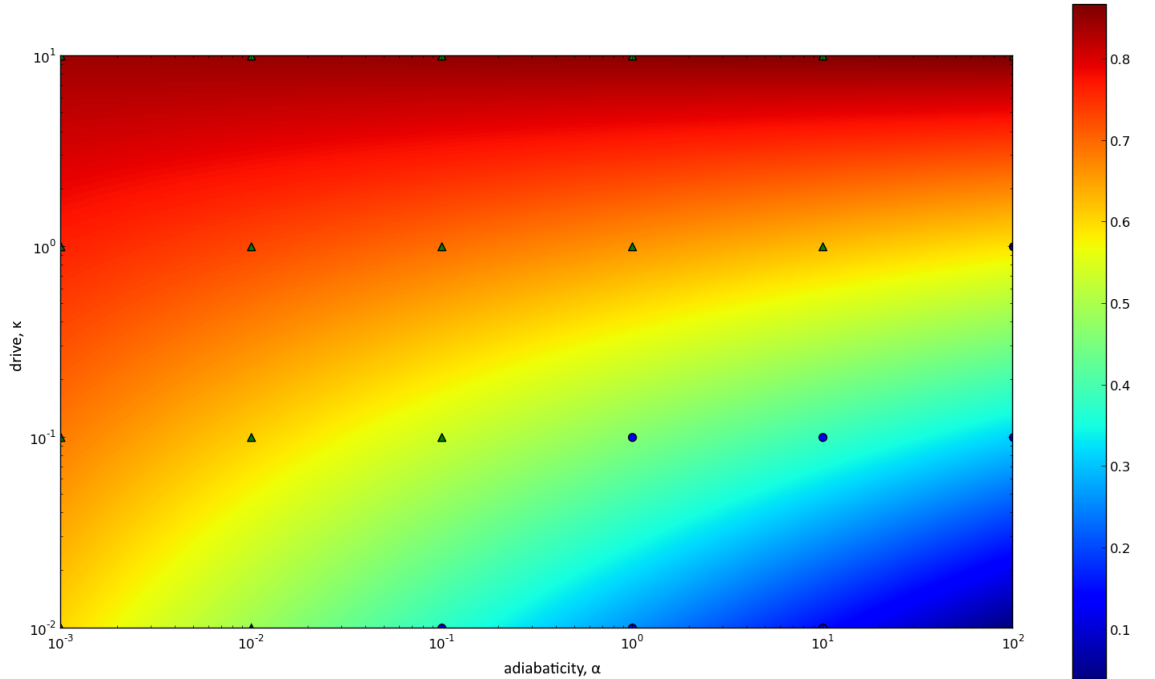
Figure 4.4: Fraction of energy in zonal flows after reaching steady state as a function of α and κ (triangles > 50% in zonals, circles < 50% in zonals).

The parameter κ represents the fractional change of density in the x-direction, which is essentially the density gradient or free-energy source for the drift-waves. The value of this term determines the saturation time-scales and amplitude of the turbulence, but it is the ratio of α to κ that dictates the regime of the simulated plasma. Figure 4.4 shows the fraction of energy in the zonal flows as these two parameters are varied independently. A limitation of these LES models is their inability to produce the inverse cascade, meaning zonal flows may not be reproduced. LES dissipation models are therefore expected to be more effective for plasma in a regime without zonal flows.

4.2.3 Varying resolution

A comparison of the k-spectrum for varying resolutions given *no* LES dissipation can be seen in figure 4.5. As resolution is decreased, not only does the range in k-space decrease, but the characteristics of the resulting turbulence are seen to change and

decrease in accuracy significantly from the reference 512×512 resolution. Notice that there is a resolution at which the k-space range extends so high that the power is dominated by noise at machine precision. It is unnecessary to have resolution as high as the reference case when the 256×256 case has sufficient resolution to reach this scale. The 128×128 simulation does not resolve the smallest necessary scales, so the accuracy begins to falter here and at lower resolutions. The LES dissipation models are needed for low resolution simulations to recover accuracy.
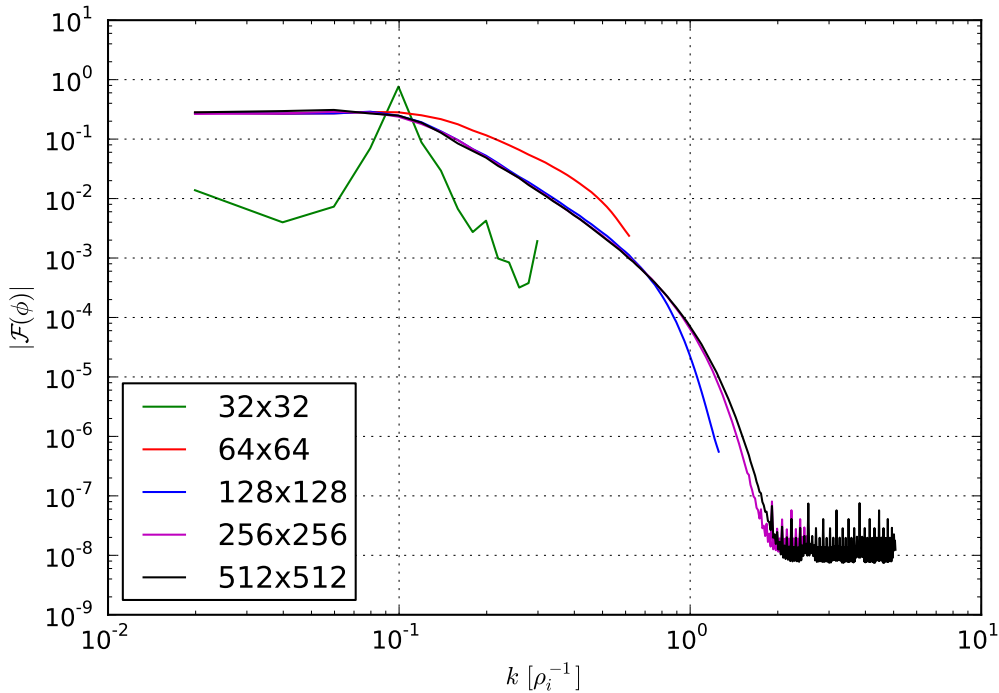
Figure 4.5: Potential k-spectra of turbulence simulations of varying resolutions with standard viscosity, but no LES dissipation model.

4.3 LES dissipation models

Decreasing the resolution of a given simulation acts as a low-pass filter on the k-space spectrum by limiting k to lower values. Unfortunately, important information at higher k-values can and will be lost, which impacts low-k behaviour at later time-steps. Aliasing is also possible where the high-k features, such as nonlinear coupling, are reflected and become low-k artefacts. To decrease resolution requirements for efficient computation it is thus imperative to model the effects of these small scale (large-k) behaviours. Four models will be investigated in this chapter, starting with additional standard viscosity, and moving to hyperviscosity, the Smagorinsky model, and finally a

dissipation scheme used in the 3D tokamak core turbulence code CENTORI [30]. In all cases, there are free parameters like LES viscosity constants, that must be determined; this process is explained in the next section (section 4.4). All of these LES dissipation rate terms, D, are included by simply adding them to the evolution equations:

$$\frac{\partial f}{\partial t} = \cdots + D \tag{4.4}$$

4.3.1   Standard viscosity

Viscosity is essentially the friction between fluid particles moving with different velocities (i.e. sheared flow), and it dissipates energy similarly: through heat, sound, etc. Viscous dissipation has a simple mathematical expression:

$$D = \vec{\nabla} \cdot (\nu \nabla f) \tag{4.5}$$

where ν is the viscosity and f is the relevant fluid field, such as density or vorticity. If ν is constant in space, this can be reduced to $D = \nu \nabla^2 f$. In the Hasegawa-Wakatani system there is already a standard viscosity dissipative term in each equation. For the large eddy tests, another such term is added to both equations with a different value for the viscosity than the original term. Linearising this term reveals that the energy is dissipated as a function of k^2, so in this way smaller scales are suppressed more strongly than large scales. Some of the limitations of this model have been explored previously [40], including the lack of inverse energy transfer (discussed later) and the arbitrariness of the smallest scale.

4.3.2   Hyperviscosity

The hyperviscosity model is named for its higher order k-space dissipation than standard viscosity. The form of the hyperviscosity model used here is

$$D = (-1)^{\frac{p}{2}-1} C_d \Delta^p \nabla^p f \tag{4.6}$$

where C_d is a constant, Δ is again the characteristic length scale, and p is an even integer with usually $p \geq 4$. This reduces to standard viscosity when $p = 2$. It can easily

be seen, then, that this method gives dissipation to the spectra of order k^p dissipating energy much more aggressively for small scales than the standard viscosity case. The hyperviscosity model has been explored in detail in [112], in an attempt to remove free parameters by constraining C_d and p as follows:

$$p = 1.7k_c/k_{av} + 2.4$$
$$C_d = 0.1Sk_c/k_{av}$$

(4.7)

where k_c is the cut-off wave number, k_{av}, is the average wave number, and S is the volume averaged shearing rate. These relations were derived empirically with fits of the data resulting from turbulence simulations of varying strength. Though this has the potential to be quite useful, it requires the knowledge of k_c and k_{av}, which means a high resolution simulation must have already been run and these values extracted. For a simple case, like the H-W system modelled here, this is possible, but for more complex (and therefore interesting) simulations there is not the luxury of running a reference case.

4.3.3 Smagorinsky

Joseph Smagorinsky proposed a sub-grid model for LES in 1963 [111], which also utilises the standard viscosity form shown in equation 4.5. However, the viscosity itself is a function of the flow velocity so is not constant across the simulation in space or time. The viscosity takes the form

$$\nu_\varpi = \nu_n = (C_d\Delta)^2 S_{xy}$$

(4.8)

with

$$S = \sqrt{\left(\frac{\partial v_x}{\partial x}\right)^2 + \left(\frac{\partial v_z}{\partial z}\right)^2 + \frac{1}{2}\left(\frac{\partial v_x}{\partial z} + \frac{\partial v_z}{\partial x}\right)^2}$$

(4.9)

where S is the rate of strain of the velocity field which has values varying spatially (very similar to the rate-of-strain tensor in equation 1.16), C_d is a dissipation constant, and Δ is a characteristic length scale (i.e. the grid spacing). Assuming the velocities of the particles within the plasma are dominated by $\vec{E} \times \vec{B}$ drift, the velocities can be

written as

$$v_x \sim -\frac{\partial \phi}{\partial z} \qquad\qquad v_z \sim \frac{\partial \phi}{\partial x}.$$

Like standard viscosity, the Smagorinsky model dissipates energy from the spectrum on the order k^2 due to the second derivatives present in S_{xy}. The Δ factor helps to scale this dissipation as simulation resolution is altered - at high resolutions Δ is small therefore the dissipation is also small, and *vice versa*. This particular dissipation model has been used extensively in fluid simulations for large systems like oceans and the weather [120] as well as for plasmas [121].

4.3.4   CENTORI dissipation

This dissipation model is an extension of the Smagorinsky model, and likewise provides dissipation on the order k^2. In the 3D CENTORI code [30], the full expression for the dissipation rate is

$$D_v = \frac{1}{v_A} \left\{ \chi_{e,NC} + \chi_{i,NC} \left(1 + q \langle R \rangle^2 \sqrt{\frac{m_i}{m_e}} \left[f_{JJ} \vec{J}^{*2} + \vec{\varpi}^{*2} \right] \right) \right\} \nabla \times \vec{\varpi}. \qquad (4.10)$$

where v_A is the Alfveǹ speed, $\chi_{e,NC}$ is the neoclassical electron diffusivity, $\chi_{i,NC}$ is the neoclassical ion diffusivity, q is the safety factor, $\langle R \rangle$ is the flux averaged major radius, m_s is the mass of each species, f_{JJ} is a user-defined quantity (usually unity), $\vec{J}^*$ is the normalised current density, and $\vec{\varpi}*$ is the normalised vorticity. This expression is the dissipation for the velocity equation. Since $\vec{\varpi} = \nabla \times v$ and $\vec{\nabla} \cdot \vec{v} = 0$, then $\nabla \times \vec{\varpi} = -\nabla^2 \vec{v}$, so this diffusion term is order k^2. Since the Smagorinsky model is for general fluids, this model attempts to modify it to include the dissipation not only due to vorticity and flows but also the dissipation due to currents, a phenomenon specific to plasmas. For the H-W system, such a model can be simplified to the following:

$$D = C_d \left(\left[\alpha \left(\phi - n \right) \right]^2 + \varpi^2 \right) \nabla^2 f \qquad (4.11)$$

where C_d is a constant. From the derivation of the H-W equations, it can be seen that $\alpha(\phi - n) \sim J_\parallel$. Some of the free parameters and constants from the original model have

been removed to simplify the expression and include only relevant physics.

4.4   Parameter constraints

There are multiple free parameters for each simulation that must be given values to keep the baseline simulation consistent while obtaining the best performance from the LES models. The values used are determined carefully and justified in this section.

4.4.1   Simulation geometry

The simulations of the Hasegawa-Wakatani system are all performed in a slab geometry of $50\rho_i \times 50\rho_i$. As stated earlier, the magnetic field is in the y-direction, but the H-W system is for perpendicular behaviour only so the simulation axes are x and z. The resolution of the reference simulation is 512×512 points for a $50\rho_i \times 50\rho_i$ box, therefore $dx = dz = 0.098\rho_i$. The LES simulations are chosen to have a resolution of 64×64 points for the same size box, so $dx_{LES} = dz_{LES} = 0.78\rho_i$. This is chosen from figure 4.5 where this resolution starts to have a divergent solution from the reference. The even lower resolution of 32×32 points is essentially just noise, and though the LES dissipation models would improve the accuracy of simulations at this resolution, the improvement would not be significant enough for it to be useful.

Because the density gradient is imposed in the x-direction this is sometimes referred to herein as the radial direction since it is the analogous tokamak coordinate. Likewise, the z-direction will sometimes be referred to as the poloidal direction since the magnetic field is dominantly toroidal for a standard tokamak; however, the z-direction is more accurately in the binormal direction $\hat{x} \times \hat{b}$, where $\hat{b}$ is the direction of the magnetic field.

4.4.2   Adiabaticity and density gradient

The adiabaticity parameter, α, is related to the parallel magnetic field connection length and resistivity (i.e. $\alpha \sim \dfrac{k_\parallel^2}{\eta}$), and κ is essentially the background density gradient and instability drive. These two parameters determine the regime of the turbulent

behaviour, and specifically, the zonal component of the energy. For this study, these parameters are chosen to produce a turbulent plasma with minimal energy in zonal flows - $\alpha = 1.0$ and $\kappa = 0.1$, placing the simulations in the bottom right of figure 4.4.

4.4.3   Numerical dissipation

The standard viscous dissipation that is present, even in the reference case, is given a normalised value $\nu = 0.001$ for the following reasons. Too much dissipation can cause an over-suppression of features in the turbulence, so it is desirable to keep this as low as possible; however, there is a lower limit. When running simulations there is an intrinsic numerical dissipation related to the resolution due to the order of the numerical methods utilised (differentiation, Laplacian inversion, etc.). Lower resolution results in higher numerical dissipation. To remove this as a variable in this study, the imposed viscous dissipation should be significantly larger than the numerical dissipation present for 1.2 grid points per ρ_i, the lowest resolution of interest. Simulations were run with no imposed dissipation to determine the level of numerical dissipation, which was found to be consistent with a viscosity of the order 10^{-6}. This sets a safe lower limit on the viscosity to $\sim 10^{-3}$, which is about an order of magnitude less than measured viscosity corresponding to diffusivity $D = 1\mathrm{m}^2/\mathrm{s}$ (assuming $\rho_i = 1\mathrm{cm}$ and $\omega_{ci}^{-1} = 10^{-6}\mathrm{s}$) [122].

4.4.4   LES dissipation constants

The constants in the LES dissipation models are free parameters that can be chosen by the user. However, that is not ideal, because there will be a value for these constants that results in the best agreement with the reference case. In order to find the best value for these constants, a scan over multiple orders of magnitude is performed, clearly demonstrating a peak in performance for each model as shown in figure 4.6. The parameters minimised here are the density and potential spectral errors and the energy error. The average line (red) is spline interpolated to find the best dissipation constant value for each model. The simulations with these values that minimise the error are the ones used in the results section to complete the analysis. Since different values for C_d minimise each field, the average was used, but it could be that some fields are more important than others for a given simulation. The results of this scan are shown

in figure 4.6. It is up to the user to determine what this constant should be taking into account all the variables. This scan over values of dissipation constant obviously
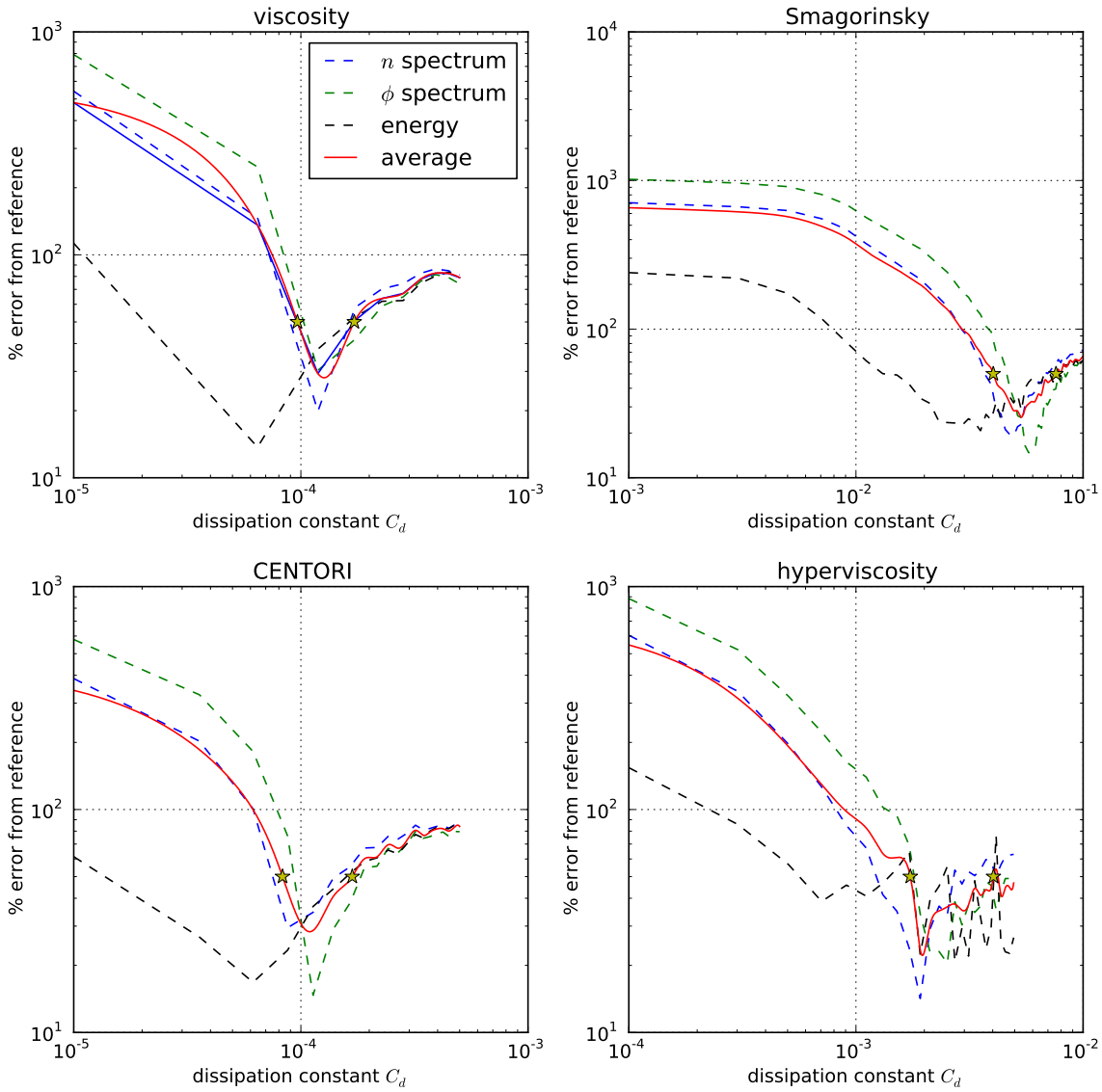
Figure 4.6: Many simulations were run to determine the ideal value for the free parameter, C_d the dissipation constant. The density spectrum, potential spectrum, and energy were compared to the reference case and the error minimised. The yellow stars indicate where the error is 50% and the corresponding value of C_d for each is shown in table 4.1.

requires a reference simulation for comparison of the results. Though for this study is was feasible, in many more realistic simulations this is not possible. It is striking, as well, the small width of the minima troughs indicating that there is a very narrow region of parameter space that provides good agreement with the reference case. Yet, it is apparent that it is better to err on the side of higher dissipation over lower.

For this study it is assumed that the dissipation constants for both density and vorticity equations are the same, removing a free parameter that could be explored. This

Table 4.1: The values for dissipation constant, C_d, that minimise the error between the reference and LES dissipation models. The bounds C_d^- and C_d^+ are the values for the constant that give 50% error from the correct solution (shown as the yellow stars in figure 4.6).

	viscosity	hyperviscosity	Smagorinsky	CENTORI
C_d^-	9.65e-5	1.73e-3	4.02e-2	8.30e-5
C_d	1.27e-4	1.96e-3	5.35e-2	1.10e-4
C_d^+	1.71e-4	4.03e-3	7.60e-2	1.68e-4

is reasonable because the normalised vorticity and density tend to be about the same order of magnitude; however, more improvement could be seen by relaxing this condition. The hyperviscosity dissipation contains one more free parameter than the other models - the value p that determines the rank of the derivative. This has been set to 6, which is a common value used [112], though an extension of this work could explore the effect of a wider range for this parameter.

4.5   Results

Seven system features are analysed and compared with the reference case for each dissipation model to assess their suitability as LES models. These comparisons are the density, potential, and vorticity spectra, the fluxes, the energy, and the enstrophy. None of the tested models emerged as the clear best, with each recovering different system features better than the others. The results and analysis are detailed in the following sections.

4.5.1   Spectra

Figure 4.7 shows the potential and density spectra for all of the models. The density and potential spectra show a similar cascade in the energy with large structures dominating, but also with energy trickling down to smaller scales. The k-range of the LES dissipation model spectra is much smaller than that of the reference due to the lower resolution of the simulations. The resolution in k-space, however, is the same for all the simulations as the size of the simulation slab is the same.

All of the models show a reasonable agreement at high-k values, but there is obvious disagreement at low-k. This is due to over-dissipation at the medium k-values, slowing
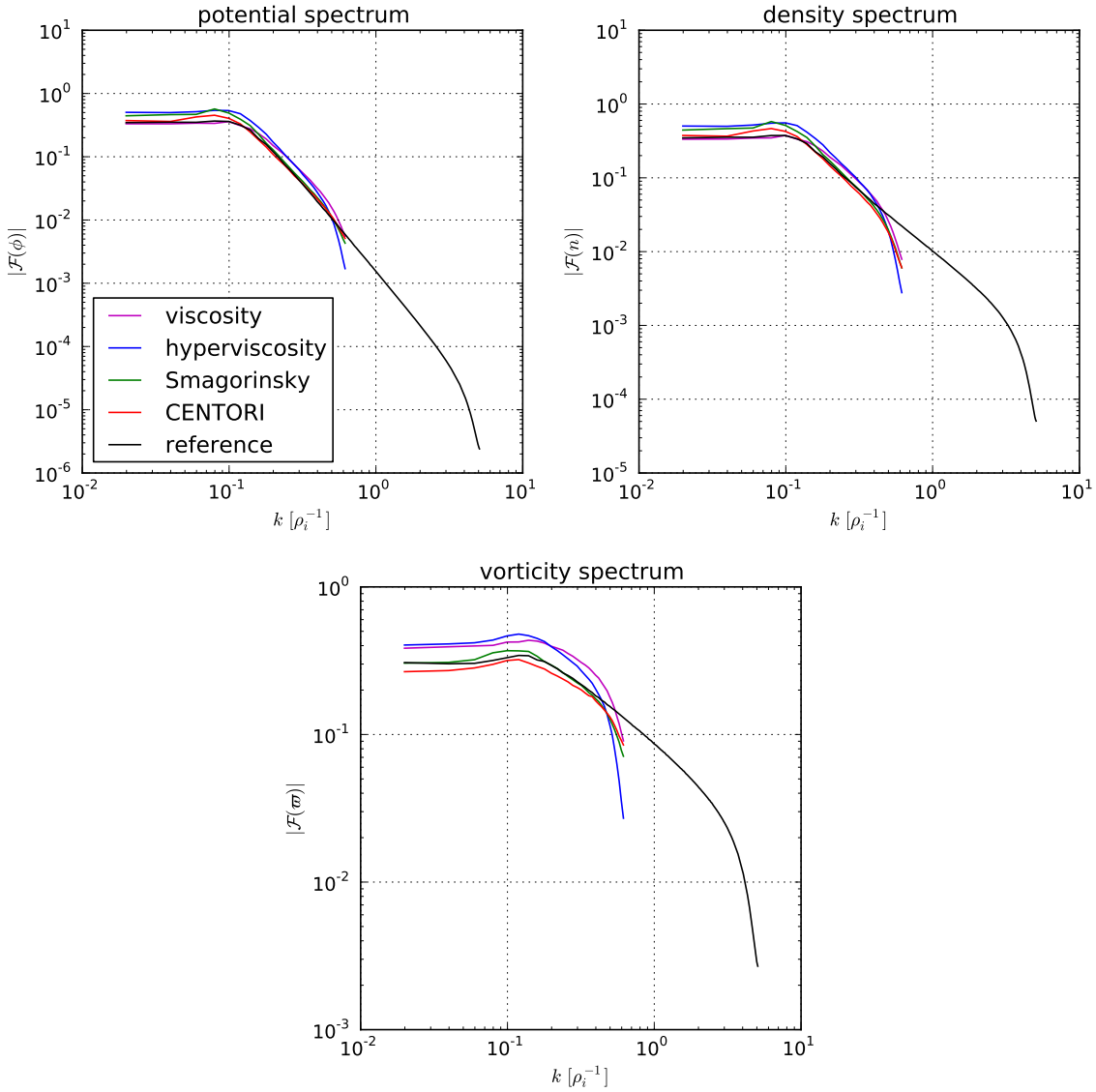
Figure 4.7: The potential (left), density (right), and vorticity (bottom) spectra are shown for the reference case (black) and the simulations using the LES dissipation models.

the cascade. The standard viscosity and CENTORI dissipation models qualitatively show the best agreement throughout the entire spectrum.

The vorticity spectrum is not much different in the reference case to the density and potential spectra; however, the lower resolution viscosity and hyperviscosity cases show a consistent overestimation of the energy in the vorticity at low k-values. All the low resolution LES cases show a steep fall-off in the vorticity at medium k-values, a feature that is not seen in the reference until high k. These differences are expected since the vorticity spectrum is much flatter than the density and potential (i.e. more energy in smaller features) so with lower resolution these are not explicitly resolved.

4.5.2 Flux

Particle flux is often the most important feature of turbulence simulations since anomalous levels of transport usually dominate over neo-classical levels. Figure 4.8 shows smoothed flux levels for both radial-x and poloidal-z directions. Since the driving background density gradient is in the x-direction, the radial flux is expected to be the most relevant to tokamak transport. Particle flux is calculated here by assuming the perpendicular velocities are $\vec{E} \times \vec{B}$, so

$$\vec{\Gamma} = n\vec{v} = n\hat{b} \times \nabla \phi \tag{4.12}$$

Hyperviscosity is the only model which overestimates the radial flux (by about 45%), while the other models underestimate the radial flux by about the same amount. The linear stage and non-linear stages of the evolution of the turbulence (i.e. pre-saturation) develop at a slower rate for the LES models compared to the reference case due to the ubiquitous dissipation of energy from the LES, while the reference case will only have this dissipation once the turbulence has begun to saturate and the cascade has developed.

The poloidal flux is quite different between all of the LES cases and the reference case, which demonstrates a substantial non-zero poloidal flow. The hyperviscosity and Smagorinsky models show about zero net poloidal flux, while the CENTORI and viscosity cases have a slight net flux. Poloidal flows can be very important in tokamaks since a radial shear in these flows can reduce turbulence [43] and potentially give rise to the L-H transition [46]. In the reference case, positive and negative density perturbations are seen to move in opposite directions poloidally, giving rise to this net flux. However, in the LES cases, the hills and holes all flow in the same poloidal direction resulting in nearly no flux. In the reference case this is thought to be due to the inverse cascade, where energy is transferred from small scales back up to large scales, giving rise to zonal behaviour [43, 124]. The LES models do not have sufficient complexity to generate an inverse cascade since the operator is dissipative only. One could imagine a system where the dissipation coefficient is self-consistently calculated to be positive or negative depending on whether the local cascade should be down
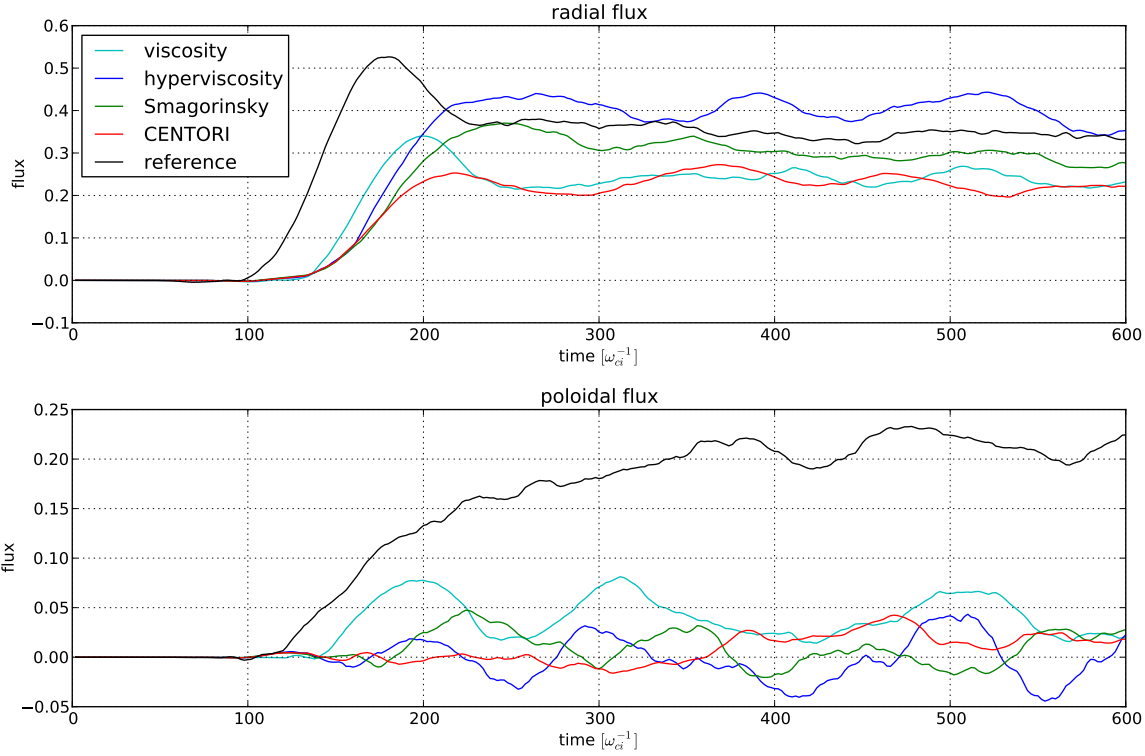
Figure 4.8: The radial (top) and poloidal (bottom) particle fluxes for the reference (black) and LES simulations. These have been smoothed in time using the Savitzky-Golay filter [123] to reveal the time-averaged features important in transport.

or uphill; however, this in itself is worthy of a full thesis so is not investigated here. Despite the lack of poloidal flow generation in this model, a more complex model in realistic geometry should be able to generate these flows even with LES dissipation due to diamagnetic rotation and geometric terms.

4.5.3 Energy and enstrophy

The energy and enstrophy of the HW system are both conserved quantities where the energy is defined in equation 4.3, and the enstrophy is

$$W = \frac{1}{2} \iint (n - \varpi)^2 \ \mathrm{d}x\mathrm{d}z \tag{4.13}$$

The energy and enstrophy of all the simulations grow to a value about which they oscillate indefinitely, which corresponds to the evolution and full development of the turbulent cascade at which point the sources and sinks of energy equalise. Figure 4.9 shows the results for all the LES models as compared to the reference case (black). All of the models are qualitatively similar to the reference case, however, there are key differences worth discussing. The final value of the energies and enstrophies are not

the same, but within about 60%, as detailed in the table 4.2. The energy, interestingly, is highest for the reference case - the LES dissipative models remove too much energy from the system. The evolution of the plasma from its initial state to the saturated turbulent state is also slowed by the extra dissipation, as the growth of the energy and enstrophy is slower for all LES cases.

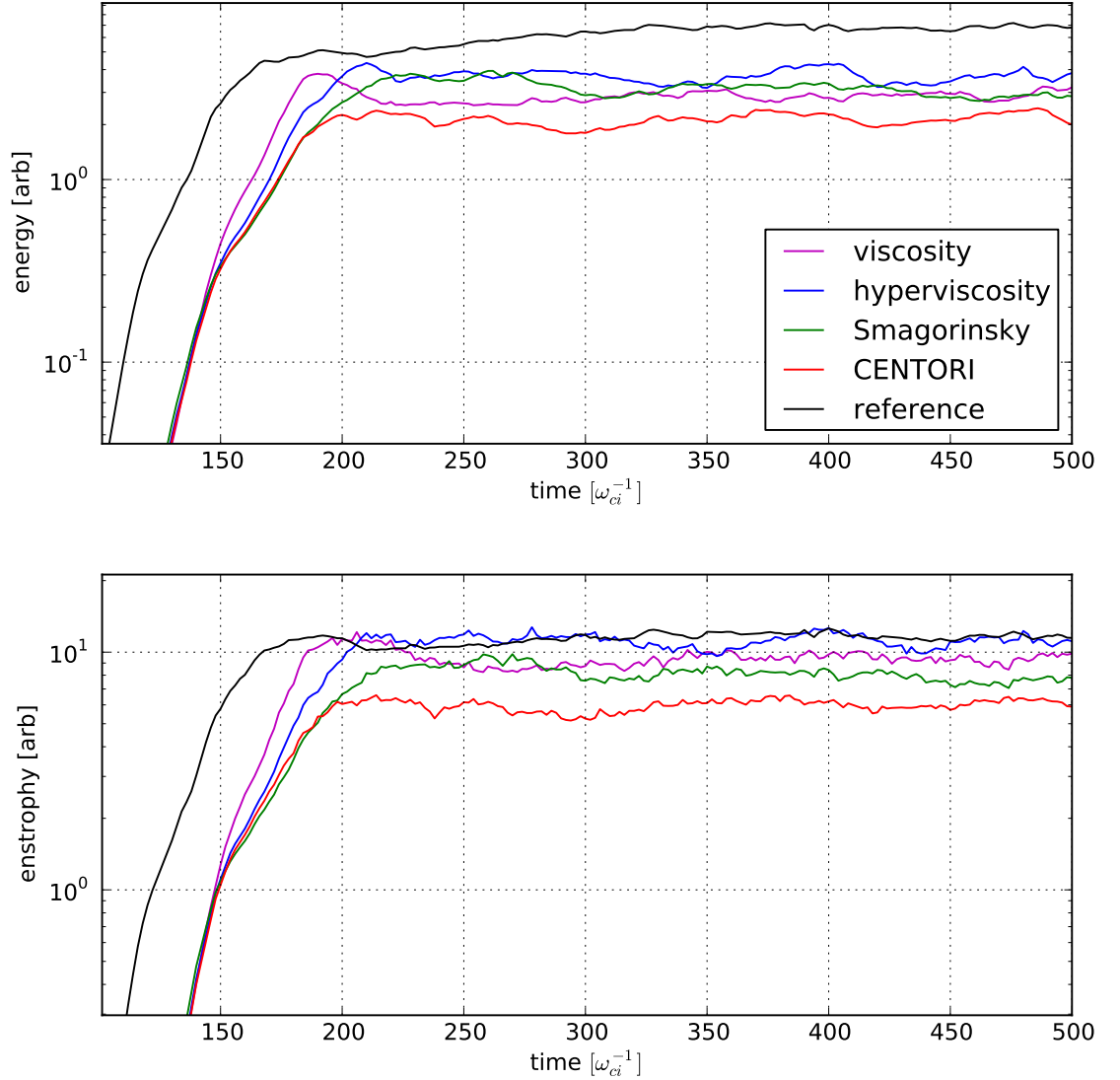**Figure 4.9:** The energy and enstrophy of all the LES models are compared to the reference case.

The enstrophy is also well reproduced, within about a factor of two, but there is no clear trend as some models produce a higher enstrophy than the reference and others a lower. Nor is it related to the order of dissipation with hyperviscosity, Smagorinsky, and CENTORI all below the reference case.

4.5.3.1 Energy cascade

In addition to the time trace of the energy evolution from the initial conditions to the saturated turbulent state, the energy also has a characteristic spectrum called the "cascade," discussed earlier in section 4.1. Figure 4.10 shows the reference cascade as well as the spectra for the LES cases. The slope of these energy cascades is about -2.6, which agrees with the published literature on Hasegawa-Wakatani drift-wave turbulence for $\alpha = 1$ [42]. There is very good qualitative and quantitative agreement, especially for the Smagorinsky and CENTORI cases.
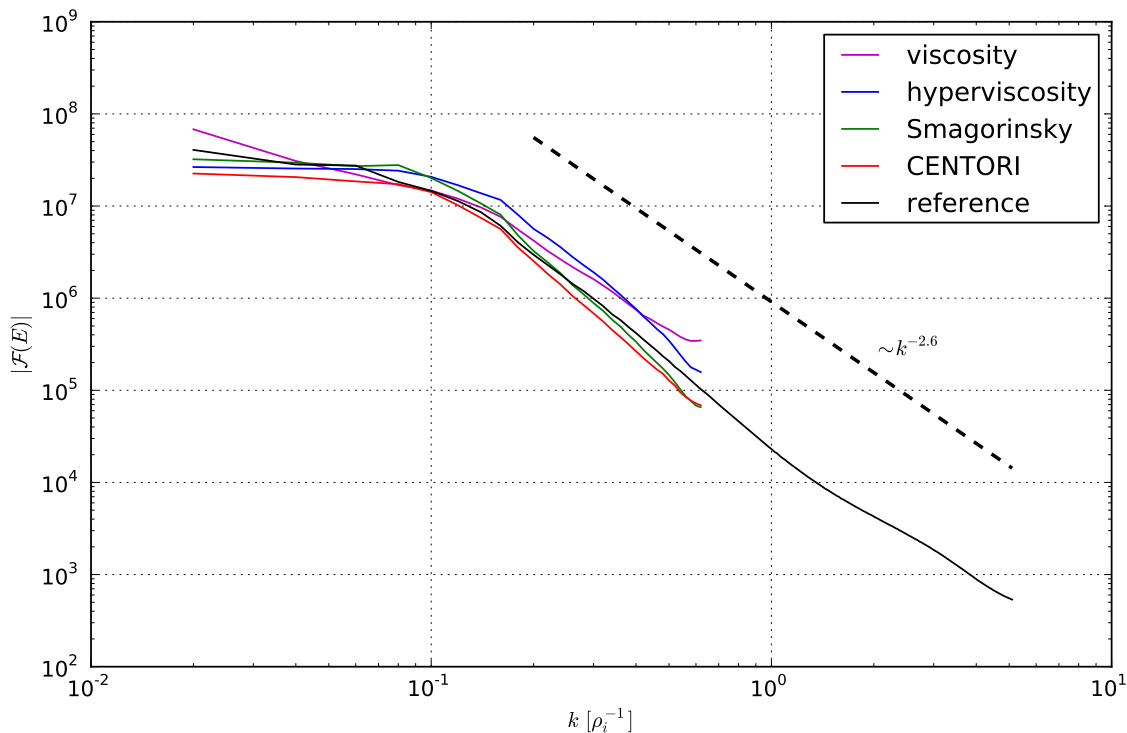
Figure 4.10: The energy cascade is shown for the reference and all the LES models. The agreement is qualitatively very good for all models with the peak in low wave numbers and a cascade down to higher k. The cascade has a k-dependence of $\sim k^{-2.6}$.

4.5.3.2 Enstrophy cascade

Despite the reasonable agreement between the models for enstrophy as a function of time, the enstrophy cascades in figure 4.11 exhibit a significant disagreement consistent with a breakdown in the inverse cascade. This, in combination with the lack of flux transverse to the background density gradient, indicates that the LES models are unable to reproduce the inverse cascade that exists in the high resolution, reference case.
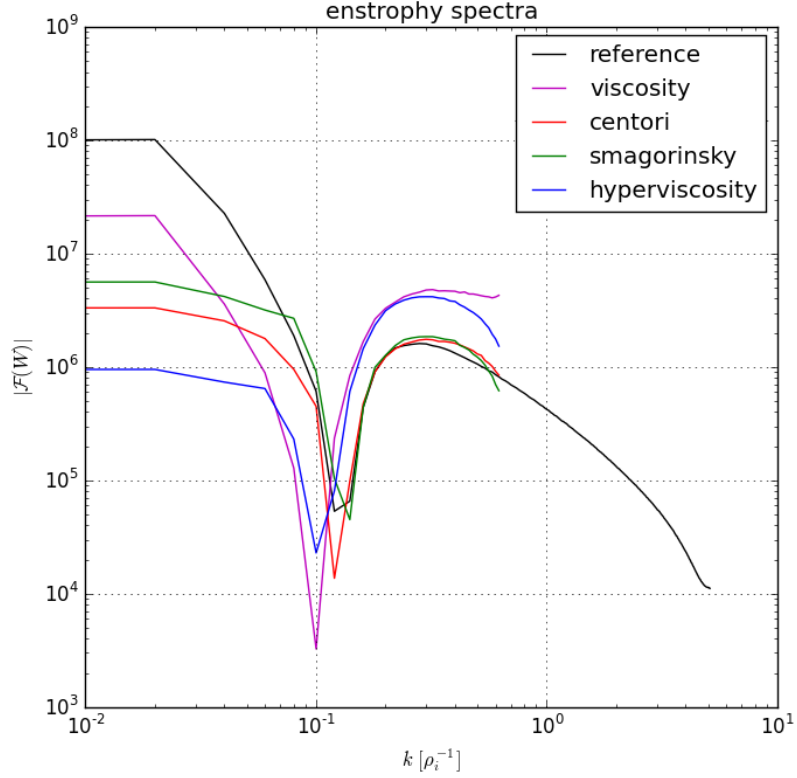
Figure 4.11: The enstrophy cascade is shown for the reference and all the LES models.

4.5.4   Overview

The accuracy of each LES model (using the optimised dissipation constants in table 4.1) as compared to the reference case is detailed in table 4.2. The minimum error for each system parameter is shown in bold. Each model is compared to the reference case and the result is given as the root mean squared percentage error calculated by

$$E_{RMS\%} = \sqrt{\frac{1}{N_k N_t} \sum_{t=t_f/3}^{t_f} \sum_{i=k_{\min}}^{k_{\max}} \left(1 - \frac{\log |\mathcal{F}(f)|_{i,t}}{\log |\mathcal{F}(f_{\mathrm{ref}})|_{i,t}}\right)^2} \tag{4.14}$$

where $|\mathcal{F}(f)|$ is the spectrum of analysed field, f, N_t is the total number of time steps averaged over, t_f is the final time, N_k is the total number of wave numbers in the LES cases, and $k_{\min}$ and $k_{\max}$ are the minimum and maximum wave numbers for the LES cases. This metric is chosen to compare the models because it relatively equally weights the differences at high and low wave number, as well as produces a percentage error that has an obvious interpretation. Because the reference case extends to higher wave numbers, the mean in this calculation is performed across the common domain for the wave number and across the last two-thirds of the time trace (i.e. steady state region) when performed on the energy, enstrophy, and flux time traces. The clear indication is

101

that all models provided a marked improvement over the case without any large eddy dissipation. Again, it is vital to note that none of these models recovers the radial flux seen in the reference case.

Table 4.2: The RMS percentage errors ($E_{RMS\%}$) are detailed for each LES model as compared to the reference case as well as for the case with *no* LES. The parameters analysed are (from left to right) density spectrum n, potential spectrum ϕ, vorticity spectrum ϖ, energy E, enstrophy W, radial flux Γ_x, and poloidal flux Γ_z. The lowest error for each parameter is in bold.

	n	ϕ	ϖ	E	W	Γ_x	Γ_z
Viscosity	**10.2**	**9.8**	7.3	56.1	19.3	32.4	**82.8**
Hyperviscosity	25.4	23.5	12.2	**46.0**	**8.19**	45.0	101
Smagorinsky	23.7	22.5	5.04	55.5	33.1	**25.2**	104
CENTORI	26.0	24.9	**4.85**	69.0	50.0	35.2	97.0
No LES	41.2	43.7	28.4	87.4	89.3	56.0	101

4.6   Conclusions

Of the four LES dissipation models explored in this chapter, the standard viscosity recovers the high resolution behaviour best. Each method minimises at least one of the system parameters. The hyperviscosity minimises two (energy and enstrophy), while the standard viscosity minimises three (density, potential, and poloidal flux). Various properties of the plasma turbulence are reproduced by each model, so it is important to consider this analysis when deciding which model to use. For all models the agreement with the reference case is within 5-30% for most fields - the qualitative behaviour looks correct but quantitatively this is a significant difference. The same models can be used with a higher resolution to still obtain a speed-up from the reference case, but also have better accuracy than was achieved for the 64×64 case. With higher resolution, more of the small scale dissipation will be resolved, so it is expected that the dissipation constants for the LES models would need to be smaller since less extra dissipation is required. However, some of the models (Smagorinsky, hyperviscosity, and CENTORI) contain a Δ factor which is a function of the resolution and should 'automatically' scale the viscosity when the resolution is adjusted.

The Hasegawa-Wakatani system tested in this chapter is a gradient driven, relatively

simple model for drift-wave turbulence. There are, however, many types of turbulence codes (e.g. flux driven, spectral, and gyro-fluid/kinetic) that require the appropriate implementation of the LES models and may result in different behaviour for the models. There are efforts to use LES in gyrokinetic simulations [114], as well as other fluid simulations, but these tend to default to viscosity or hyperviscosity due to their ease of implementation and reasonable performance. Performing a reference simulation at high resolution becomes increasingly difficult as the model becomes more complex, so the results from this study may potentially be extrapolated to at least provide an idea for how the models will perform.

Chapter 5

Flexible field-aligned coordinates for realistic tokamak edge simulations

5.1 Introduction

In a tokamak plasma, waves and instabilities are elongated along the magnetic field line, while the perpendicular structures are small (on the order of the Larmor radius). Therefore, when simulating a tokamak plasma it is desirable to also have a coordinate system and grid that are aligned along the field. It is then required to derive a new set of coordinates related to the standard tokamak coordinates, (ψ, θ, ϕ), where $\nabla\psi \cdot \nabla\theta = 0$. This new system is derived such that one coordinate is aligned to the field. The standard method for doing this is to keep the radial flux coordinate ψ, but to replace the toroidal angle ϕ and the poloidal angle θ with a shifted toroidal angle z and field-aligned coordinate y, respectively. The mathematical derivation of this is detailed in the next section. Conceptually this means that if ψ and z are held constant while y is increased, both the toroidal and poloidal angle must change to obtain helical movement around the torus along the field line. This also implies that y and z are no longer orthogonal as θ and ϕ are. This system allows for resolution along the field line to be more sparse as is appropriate for the large structures, while maintaining fine resolution perpendicular to the magnetic field.

Though this system solves the problem of resolution, it leaves other problems un-addressed. Namely, the grid is restricted in shape in the poloidal plane. The ψ coordinate must remain perpendicular to the poloidal projection of y. If this restraint is lifted by deriving a new set of coordinates that are both field-aligned but also non-orthogonal in ψ and y, there is freedom to define a grid that matches the geometry of a particular machine in the divertor region. In the second half of this chapter, a new coordinate system that allows such freedom is presented, tested, and utilised for novel divertor plasma simulations.

In the derivation of these coordinates standard symbols for tokamak flux-coordinate geometry are used for the toroidal, poloidal, and radial directions - ϕ, θ, and ψ respectively. These coordinates form a right-handed, orthogonal coordinate system as shown in figure 5.1.

5.1.1 Standard field-aligned coordinates

The standard field-aligned coordinate system [125] is defined as

$$
\begin{aligned}
x &= \psi \\
y &= \theta \\
z &= \phi - \int_{\theta_0}^{\theta} \nu \, d\theta
\end{aligned}
\tag{5.1}
$$

where the local field line pitch is given by

$$
\nu(\psi, \theta) = \frac{\partial \phi}{\partial \theta} = \frac{\mathbf{B} \cdot \nabla \phi}{\mathbf{B} \cdot \nabla \theta} = \frac{B_\phi h_\theta}{B_\theta R}.
\tag{5.2}
$$

with toroidal field B_ϕ, poloidal field B_θ, major radius R, and poloidal arc-length h_θ. Figure 5.1 shows the geometry described by the coordinate system in equations 5.1. It is important to notice that the shift added to the z-coordinate causes the y-coordinate to be field-aligned. The x-coordinate remains perpendicular to the poloidal project of the y-coordinate, a fact that has consequences that are discussed in a later section.

The contravariant basis vectors are then found by taking the gradient of each co-
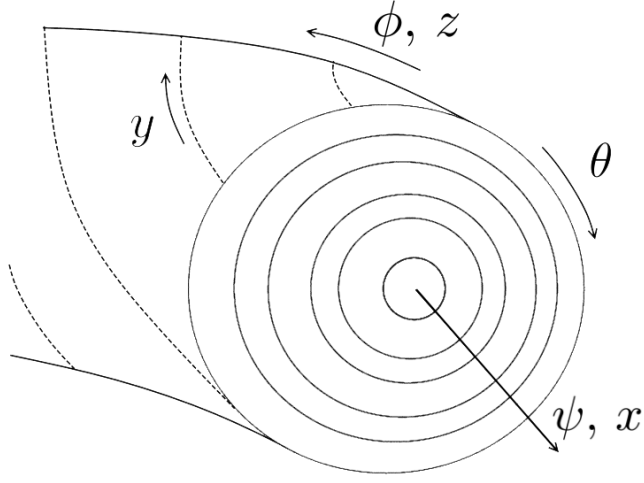
Figure 5.1: The geometry described by the coordinate system posed in equations 5.1.

ordinate, using $\nabla = \nabla\psi\frac{\partial}{\partial\psi} + \nabla\theta\frac{\partial}{\partial\theta} + \nabla\phi\frac{\partial}{\partial\phi}$ to calculate

$$\nabla x = \nabla\psi$$

$$\nabla y = \nabla\theta \qquad (5.3)$$

$$\nabla z = \nabla\phi - \nu\nabla\theta - I\nabla\psi$$

with

$$I = \int_{\theta_0}^{\theta} \frac{\partial\nu}{\partial\psi}\,d\theta. \qquad (5.4)$$

The magnetic field can be written in Clebsh form [125],

$$\mathbf{B} = \nabla x \times \nabla z = \frac{1}{J}\mathbf{e}_y \qquad (5.5)$$

where J is the Jacobian, therefore the coordinate system is field aligned. The contravariant metric tensor is symmetric and defined as

$$g^{ij} = \nabla u^i \cdot \nabla u^j = \begin{bmatrix} (\nabla\psi)^2 & 0 & -I(\nabla\psi)^2 \\ & & \\ \cdots & (\nabla\theta)^2 & -\nu(\nabla\theta)^2 \\ & & \\ \cdots & \cdots & I^2(\nabla\psi)^2 + \nu^2(\nabla\theta)^2 + (\nabla\phi)^2 \end{bmatrix}. \qquad (5.6)$$

107

Using the following identities

$$|\nabla\psi| = R|B_\theta| \qquad\qquad |\nabla\theta| = |h_\theta|^{-1} \qquad\qquad |\nabla\phi| = R^{-1} \qquad\qquad (5.7)$$

the contravariant metric tensor can be rewritten as

$$
g^{ij} = \begin{bmatrix}
(RB_\theta)^2 & 0 & -I(RB_\theta)^2 \\[2ex]
\cdots & h_\theta^{-2} & \nu h_\theta^{-2} \\[2ex]
\cdots & \cdots & I^2(RB_\theta)^2 + \nu^2 h_\theta^{-2} + R^{-2}
\end{bmatrix}
\qquad (5.8)
$$

To calculate the covariant metric tensor, one must first find the Jacobian of the system, which is given by

$$J^{-1} = \nabla x \cdot (\nabla y \times \nabla z) \qquad\qquad (5.9)$$

thus

$$J = \frac{h_\theta}{B_\theta} \qquad\qquad (5.10)$$

There is a null in the coordinate system at any X-point and O-point since $B_\theta = 0$ therefore J is undefined. The covariant basis vectors of this system are given by

$$\mathbf{e}_i = J(\nabla u^j \times \nabla u^k)$$

giving

$$\mathbf{e}_x = \frac{1}{R|B_\theta|}\hat{\mathbf{e}}_\psi + h_\theta\hat{\mathbf{e}}_\theta + IR\hat{\mathbf{e}}_\phi$$
$$\mathbf{e}_y = h_\theta\hat{\mathbf{e}}_\theta + R\nu\hat{\mathbf{e}}_\phi \qquad\qquad (5.11)$$
$$\mathbf{e}_z = R\hat{\mathbf{e}}_\phi$$

The covariant metric tensor can be written

$$
g_{ij} = \mathbf{e}_i \cdot \mathbf{e}_j =
\begin{bmatrix}
I^2 R^2 + (RB_\theta)^{-2} & B_\phi h_\theta I R B_\theta^{-1} & I R^2 \\
 & & \\
\cdots & h_\theta^2 + R^2 \nu^2 & \nu R^2 \\
 & & \\
\cdots & \cdots & R^2
\end{bmatrix}.
\tag{5.12}
$$

5.2 Flexible field-aligned coordinates

A new set of coordinates, dubbed the flexible field-aligned (FFA) system, is needed to allow a simulation mesh to be aligned with not only the magnetic field but also the divertor (or any smoothly varying) geometry in the poloidal plane. To derive these coordinates, the following system is defined by analogue to equation 5.1:

$$
x = \psi
\tag{5.13a}
$$

$$
y = \theta - y_{\text{shift}}
\tag{5.13b}
$$

$$
z = \phi - z_{\text{shift}}
\tag{5.13c}
$$

such that the shift in y (y_{shift}) allows for the x-coordinate to be aligned with any arbitrary geometry in the poloidal plane. Likewise the shift in z (z_{shift}) enables the y-coordinate to follow an arbitrary geometry toroidally. As is standard in field-aligned coordinates the z_{shift} will be defined to ensure that the y-coordinate follows the magnetic field line, as demonstrated in the previous section.

For a coordinate system to uniquely define all points in space it must obey

$$
\frac{\partial x}{\partial y} = \frac{\partial x}{\partial z} = \frac{\partial y}{\partial x} = \frac{\partial y}{\partial z} = \frac{\partial z}{\partial x} = \frac{\partial z}{\partial y} = 0.
\tag{5.14}
$$

In this way one can derive the y_{shift} by recognising that $\frac{\partial y}{\partial x} = 0$ so

$$
0 = \frac{\partial y}{\partial x} = \frac{\partial}{\partial \psi} \left(\theta - y_{\text{shift}} \right) \quad \rightarrow \quad y_{\text{shift}} = \int_{\psi_0}^{\psi} \frac{\partial \theta}{\partial \psi} \, d\psi.
\tag{5.15}
$$

A non-orthogonality parameter (analogous to the field line pitch, but in the poloidal plane) is defined as $\eta = \dfrac{\partial \theta}{\partial \psi}$. Similar to ν, the field line pitch, η is a function of ψ and θ. In grid generation, this parameter is related directly to the geometry of the grid where $\eta = \sin \beta$ where β is the angle between the lines connecting grid points, as indicated in figure 5.2. This yields the final expression for the y-coordinate:

$$y = \theta - \int_{\psi_0}^{\psi} \eta \, d\psi. \tag{5.16}$$

It is simple to see that if the grid is orthogonal (i.e. $\beta = 0 \implies \eta = 0$), the coordinates reduce back to the standard field-aligned system. Figure 5.2 demonstrates the physical functionality of the y-shift term in matching the divertor geometry. The result of this shift, represented by the green arrow, is the alignment of the x-coordinate with the divertor plate.
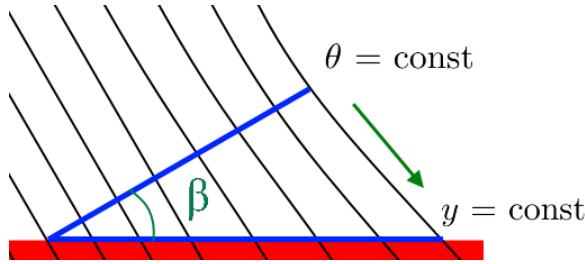

Figure 5.2: A physical picture of why the y-shift term (indicated by the green arrow) is needed and how lines of constant θ compare to lines of constant y. β represents the angle between the grid points and is related to the non-orthogonality of the system by $\eta = \sin \beta$.

The same method can be used to solve for z_shift by this time recognising that $\dfrac{\partial z}{\partial y} = 0$,

$$0 = \frac{\partial z}{\partial y} = \frac{\partial}{\partial y} (\phi - z_\text{shift}) \quad \rightarrow \quad z_\text{shift} = \int_{y_0}^{y} \frac{\partial \phi}{\partial y} \, dy \tag{5.17}$$

however this needs further manipulation using equation 5.16 to obtain a final system dependent established parameters.

$$\begin{aligned} z_\text{shift} &= \int_{y_0}^{y} \frac{\partial \phi}{\partial y} \, dy \\ &= \int_{y_0}^{y} \frac{\partial \phi}{\partial \theta} \frac{\partial \theta}{\partial y} \, dy \\ &= \int_{y_0}^{y} \frac{\partial \phi}{\partial \theta} \left(1 + \frac{\partial}{\partial y} \int_{\psi_0}^{\psi} \eta \, d\psi \right) dy \end{aligned} \tag{5.18}$$

110

As defined previously, the field line pitch $\nu = \dfrac{\partial \phi}{\partial \theta}$, yielding the final expression for the z-coordinate:

$$z = \phi - \int_{y_0}^{y} \nu \left(1 + \frac{\partial}{\partial y} \int_{\psi_0}^{\psi} \eta \, d\psi \right) dy \tag{5.19}$$

With new coordinate definitions derived above and given in equations 5.13a, 5.16, and 5.19, the new more general covariant and contravariant metric tensors are then derived. The contravariant basis vectors are found, as before, by taking the gradient of each coordinate.

$$\nabla x = \nabla \psi$$

$$\nabla y = G \nabla \theta - \eta \nabla \psi \tag{5.20}$$

$$\nabla z = \nabla \phi - H \nabla \theta - I \nabla \psi$$

where

$$
\begin{aligned}
G &= \frac{\partial y}{\partial \theta} = 1 - \frac{\partial}{\partial \theta} \int_{x_0}^{x} \eta \, dx \\
I &= \frac{\partial z}{\partial \psi} = \frac{\partial}{\partial \psi} \int_{y_0}^{y} \nu \left(1 + \frac{\partial}{\partial y} \int_{x_0}^{x} \eta \, dx \right) dy \\
H &= \frac{\partial z}{\partial \theta} = \frac{\partial}{\partial \theta} \int_{y_0}^{y} \nu \left(1 + \frac{\partial}{\partial y} \int_{x_0}^{x} \eta \, dx \right) dy.
\end{aligned}
\tag{5.21}
$$

These expressions cannot be simplified via the Leibniz integral rule, as was done previously, because y is not independent of θ or ψ. Since the magnetic field can still be written in Clebsh form, as in equation 5.5, the system is still field aligned. The contravariant metric tensor can be written

$$
g^{ij} = \nabla u^i \cdot \nabla u^j =
\begin{bmatrix}
(\nabla \psi)^2 & -\eta(\nabla \psi)^2 & -I(\nabla \psi)^2 \\[2ex]
\cdots & (G)^2(\nabla \theta)^2 + \eta^2(\nabla \psi)^2 & I\eta(\nabla \psi)^2 - GH(\nabla \theta)^2 \\[2ex]
\cdots & \cdots & I^2(\nabla \psi)^2 + H^2(\nabla \theta)^2 + (\nabla \phi)^2
\end{bmatrix}
\tag{5.22}
$$

Using the physical identities in equation 5.7, which are still valid, the contravariant metric tensor can be rewritten as

$$
g^{ij} = \begin{bmatrix}
(RB_\theta)^2 & -\eta(RB_\theta)^2 & -I(RB_\theta)^2 \\
& & \\
\cdots & G^2 h_\theta^{-2} + \eta^2 (RB_\theta)^2 & I\eta(RB_\theta)^2 - GHh_\theta^{-2} \\
& & \\
\cdots & \cdots & I^2(RB_\theta)^2 + H^2 h_\theta^{-2} + R^{-2}
\end{bmatrix} \tag{5.23}
$$

To calculate the covariant metric tensor, one must first find the Jacobian as in 5.9, giving

$$
J = \frac{h_\theta}{GB_\theta} \tag{5.24}
$$

There is a singularity in the coordinate system when either G or B_θ are zero, such as at the X-point. The covariant basis vectors of this system are calculated in the same way as before yielding

$$
\begin{aligned}
\mathbf{e}_x &= \frac{1}{R|B_\theta|}\hat{\mathbf{e}}_\psi + \frac{h_\theta \eta}{G}\hat{\mathbf{e}}_\theta + \left(\frac{RH\eta}{G} + IR\right)\hat{\mathbf{e}}_\phi \\
\mathbf{e}_y &= \frac{h_\theta}{G}\hat{\mathbf{e}}_\theta + \frac{RH}{G}\hat{\mathbf{e}}_\phi \\
\mathbf{e}_z &= R\hat{\mathbf{e}}_\phi
\end{aligned} \tag{5.25}
$$

The covariant metric tensor can now be written

$$
g_{ij} = \mathbf{e}_i \cdot \mathbf{e}_j = \begin{bmatrix}
(RB_\theta)^{-2} + \left(\frac{h_\theta \eta}{G}\right)^2 + \left(\frac{RH\eta}{G} + IR\right)^2 & \frac{h_\theta^2 \eta}{G^2} + \frac{R^2 H}{G}\left(\frac{H\eta}{G} + I\right) & R^2\left(\frac{H\eta}{G} + I\right) \\
& & \\
\cdots & \frac{h_\theta^2}{G^2} + \frac{R^2 H^2}{G^2} & \frac{HR^2}{G} \\
& & \\
\cdots & \cdots & R^2
\end{bmatrix}
$$
$$\tag{5.26}$$

Importantly, in the limit where x and the poloidal projections of all field lines are orthogonal (ie. the standard field-aligned system), $y = \theta$ therefore $\eta = 0$, $G = 1$, $H = \nu$, and $I = \int_{\theta_0}^{\theta} \frac{\partial \nu}{\partial \psi} d\theta$. Thus, the standard field-aligned metric tensors are recovered.

112

5.3 Boundary Conditions

The boundary conditions in BOUT++ are set halfway between the last grid point and the first boundary point (ie. on the cell faces), as shown in figure 5.3. The two common boundary conditions set are Dirichlet and Neumann, in which the value of the field and the ψ-derivative of the field are set as constants, respectively. The changes to the metric require adjustments to the Neumann boundary conditions, though the Dirichlet conditions remain correct.

5.3.1 Original boundaries

Previously the x-coordinate was ψ-aligned, so setting the Neumann conditions was straightforward. The value of the derivative of the function at the boundary layer
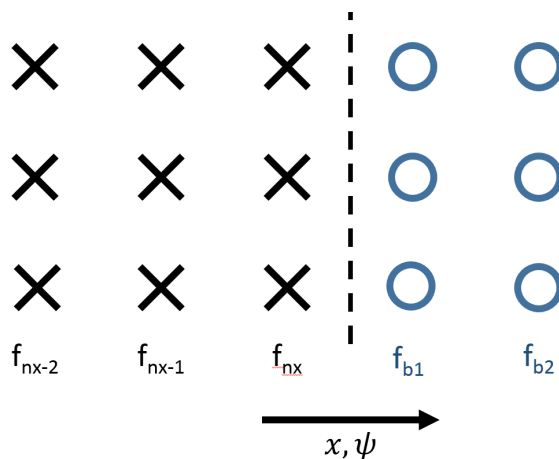

Figure 5.3: The grid cell locations in BOUT++ for mesh that is orthogonal in the poloidal plane. The boundary layer (dashed line) lies halfway between the last grid point and the first boundary cell (X's are real data and O's are boundaries). The x-direction and ψ-direction are the same for the orthogonal case.

(dotted line in figure 5.3) is set to a user-specified value, $\dfrac{\partial f_b}{\partial \psi} = f'_\psi$. A second order derivative scheme is used, so this becomes

$$\frac{f_{b1} - f_{nx}}{\delta_\psi} = f'_\psi \qquad \rightarrow \qquad f_{b1} = f_{nx} + f'_\psi \delta_\psi \tag{5.27}$$

where δ_ψ is the grid spacing in ψ. The second boundary cell can be similarly calculated to obtain

$$f_{b2} = f_{nx-1} + 3 f'_\psi \delta_\psi \tag{5.28}$$

5.3.2   New boundaries

A more general form for the boundaries can be calculated, using the new metrics derived in section 5.2. The desired boundary conditions are still to be set in the ψ-direction, but it is possible that at points on the grid the x-direction is not aligned with ψ - internally BOUT++ will solve derivatives on the mesh (ie. $\dfrac{\partial f}{\partial x}$, $\dfrac{\partial f}{\partial y}$, and $\dfrac{\partial f}{\partial z}$). A layout for the data and boundary cells for such a situation can be seen in figure 5.4. As before, Neumann conditions require $\dfrac{\partial f_b}{\partial \psi} = f'_\psi$, but on a grid that is not aligned with ψ this must be written

$$f'_\psi = \frac{\partial f_b}{\partial \psi} = g_b^{xx}\frac{\partial f_b}{\partial x} + g_b^{xy}\frac{\partial f_b}{\partial y} + g_b^{xz}\frac{\partial f_b}{\partial z}. \tag{5.29}$$

The partial derivatives in equation 5.29 are all calculated numerically on the grid, so this can be rearranged to solve for the x-derivative

$$\frac{\partial f_b}{\partial x} = \frac{1}{g_b^{xx}}\left(f'_\psi - g_b^{xy}\frac{\partial f_b}{\partial y} - g_b^{xz}\frac{\partial f_b}{\partial z}\right). \tag{5.30}$$

As before, this is combined with a second order derivative scheme to acquire equations for the values of the first and second boundary cells that satisfy $\dfrac{\partial f_b}{\partial \psi} = f'_\psi$

$$
\begin{aligned}
f_{b1} &= f_{nx} + \frac{\delta_\psi}{g_b^{xx}}\left(f'_\psi - g_b^{xy}\frac{\partial f_b}{\partial y} - g_b^{xz}\frac{\partial f_b}{\partial z}\right) \\
f_{b2} &= f_{nx-1} + \frac{3\delta_\psi}{g_b^{xx}}\left(f'_\psi - g_b^{xy}\frac{\partial f_b}{\partial y} - g_b^{xz}\frac{\partial f_b}{\partial z}\right)
\end{aligned}
\tag{5.31}
$$

The values of the metric and partial derivatives with respect to y and z should be calculated on the boundary layer itself, as is indicated by the b subscripts. However, there are no data on the boundary since it is half-way between two grid points, so linear interpolation is used to average the values on either side of the boundary. However, at the corner of the x-y and x-z domains, the average cannot be taken since the corner boundary cells are empty. In this case, the value of $\dfrac{\partial}{\partial y}$ and $\dfrac{\partial}{\partial z}$ inside the domain is used.
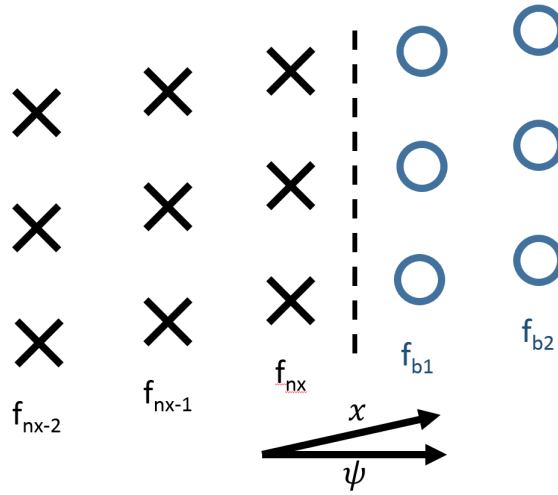
114

Figure 5.4: The grid cell locations in BOUT++ for a grid that is non-orthogonal in the poloidal plane. Importantly, the x-direction and ψ-direction are not necessarily the same for the non-orthogonal case; however, boundary conditions are still to be set for $\dfrac{\partial f}{\partial \psi}$.

5.4 Testing the Coordinate System and Metrics

To ensure that this substantial change to the simulated geometry has been implemented correctly, the numerical accuracy of the system must be benchmarked. This is done using the method of manufactured solutions [96], which is a common method for testing the numerical validity of fluid simulations. After the numerics pass the test, a physics model is simulated on a mesh that conforms to the divertor geometry and compared to the same model simulated on the original field-aligned grid used in BOUT++. The important results investigated to compare these two systems are the flux, temperature, and heat transport at the divertor plates.

5.4.1 Numerical accuracy

The method of manufacture solutions (MMS) [96] has been used to test the numerical accuracy of the newly developed and implemented metric in BOUT++. A field $f(\psi, \theta, \phi, t)$ is defined and evolved using a simple advection model

$$\frac{\partial f}{\partial t} = \hat{Q}f + S \tag{5.32}$$

where the operator $\hat{Q} = \frac{\partial}{\partial \psi} + \frac{\partial}{\partial \theta} + \frac{\partial}{\partial \phi}$ and $S(\psi, \theta, \phi, t)$ is a source term for the MMS. We choose an analytic function for $f = F$ and define the source term as

$$S = \frac{\partial F}{\partial t} - \hat{Q}F \tag{5.33}$$

By doing this, we ensure that the numerical time derivative will be equal to the analytic time derivative in the case where the numerical $\hat{Q}$ is equivalent to the analytic $\hat{Q}$. In this way the numerical accuracy of the derivative operators is tested, as any error in them will propagate in time. This has previously been done for BOUT++ to test all numerical operators [126], so the same test can be done, which is known to be accurate to second-order, to verify the new metric by evaluating this equation on various non-orthogonal grids. The order found using MMS refers to the accuracy of the numerical methods used, such as central differencing, due to the truncation of the Taylor expansion while defining the method. The lowest order method in use will determine the order of convergence seen in the MMS test.
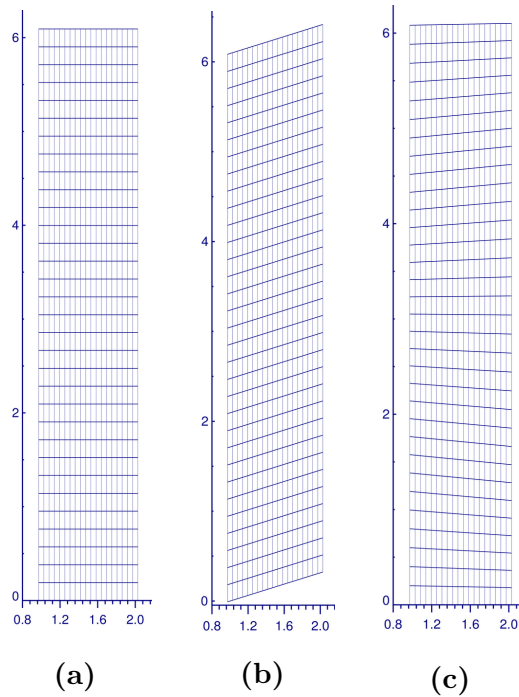

(a)　　(b)　　(c)

Figure 5.5: The grids used for both the wave test case and the MMS verification. (a) A fully orthogonal grid. (b) A grid with constant non-orthogonality in the poloidal plane. (c) A grid with sinusoidally varying grid spacing in the y-direction.

The analytic solution is defined

$$F(\psi, \theta, \phi, t) = \cos^2(\psi + \theta + \phi - t) \tag{5.34}$$

which in turn provides the definition for the source term

$$S(\psi, \theta, \phi, t) = 8\sin(\psi + \theta + \phi - t)\cos(\psi + \theta + \phi - t). \tag{5.35}$$

This manufactured solution is chosen to satisfy the criteria given by Salari, *et al.* [96], that a solution must:

(a) be composed of smooth analytic functions

(b) be general enough to exercise all terms in the system of equations

(c) have sufficient number of non-trivial derivatives

(d) have derivatives bounded by a small constant (i.e. not varying significantly in space or time)

(e) allow the code to run successfully to completion during testing

(f) be defined on a connected subset of space

(g) should be constructed such that the differential operators in the system of equations makes sense physically

Using a test grid and working from lowest to highest complexity in meshing, the new metric was fully validated. Since BOUT++ solves the equations in the shifted space (x, y, z), but the source and solution are in (ψ, θ, ϕ) space, a transformation was required to calculate the desired derivatives within the code. Consider the operator $\hat{Q}$ acting on f,

$$\hat{Q}f = \frac{\partial f}{\partial \psi} + \frac{\partial f}{\partial \theta} + \frac{\partial f}{\partial \phi} = \left(\hat{\mathbf{e}}^\psi + \hat{\mathbf{e}}^\theta + \hat{\mathbf{e}}^\phi\right) \cdot \nabla f \tag{5.36}$$

where $\hat{\mathbf{e}}^\psi$, $\hat{\mathbf{e}}^\theta$, and $\hat{\mathbf{e}}^\phi$ are the contravariant basis vectors for the respective coordinate and are defined as

$$\hat{\mathbf{e}}^\psi = \nabla\psi = \left(\nabla x \frac{\partial}{\partial x} + \nabla y \frac{\partial}{\partial y} + \nabla z \frac{\partial}{\partial z}\right)\psi$$
$$\hat{\mathbf{e}}^\theta = \nabla\theta = \left(\nabla x \frac{\partial}{\partial x} + \nabla y \frac{\partial}{\partial y} + \nabla z \frac{\partial}{\partial z}\right)\theta \tag{5.37}$$
$$\hat{\mathbf{e}}^\phi = \nabla\phi = \left(\nabla x \frac{\partial}{\partial x} + \nabla y \frac{\partial}{\partial y} + \nabla z \frac{\partial}{\partial z}\right)\phi$$

The basis vectors $\hat{\mathbf{e}}^x$, $\hat{\mathbf{e}}^y$, and $\hat{\mathbf{e}}^z$ have already been calculated in equation 5.20, and can be rearranged to give

$$\hat{\mathbf{e}}^\psi = \nabla x$$
$$\hat{\mathbf{e}}^\theta = \frac{1}{G}\left[\eta\nabla x + \nabla y\right] \tag{5.38}$$
$$\hat{\mathbf{e}}^\phi = \frac{1}{G}\left[\left(GI + H\eta\right)\nabla x + H\nabla y + G\nabla z\right].$$

Substituting these into equation 5.36 yields

$$\hat{Q}f = \frac{1}{G}\left[\nabla x \underbrace{\left(G + \eta + GI + H\eta\right)}_{v_x} + \nabla y \underbrace{\left(1 + H\right)}_{v_y} + \underbrace{G}_{v_z}\nabla z\right] \cdot \nabla f \tag{5.39}$$

Finally, using the contravariant metric tensor $g^{ij} = \nabla i \cdot \nabla j$ as calculated in equation 5.22, and assuming for this slab case $|\nabla\psi| = |\nabla\theta| = |\nabla\phi| = 1$, the evolution equation is obtained

$$\begin{aligned}
\frac{\partial f}{\partial t} = {}& \frac{v_x}{G}\left[g^{xx}\frac{\partial f}{\partial x} + g^{xy}\frac{\partial f}{\partial y} + g^{xz}\frac{\partial f}{\partial z}\right] \\
& + \frac{v_y}{G}\left[g^{yx}\frac{\partial f}{\partial x} + g^{yy}\frac{\partial f}{\partial y} + g^{yz}\frac{\partial f}{\partial z}\right] \\
& + \frac{v_z}{G}\left[g^{zx}\frac{\partial f}{\partial x} + g^{zy}\frac{\partial f}{\partial y} + g^{zz}\frac{\partial f}{\partial z}\right]
\end{aligned} \tag{5.40}$$

with $v_x = G(1+I)+\eta(1+H)$, $v_y = 1+H$, and $v_z = G$. Running the simulation to solve this equation allows the code to take derivatives of f in the shifted (x, y, z) space, though it solves the original equation which contains derivatives in the orthogonal (ψ, θ, ϕ) space.

The combinations of non-orthogonalities tested can be seen in table 5.1 where all
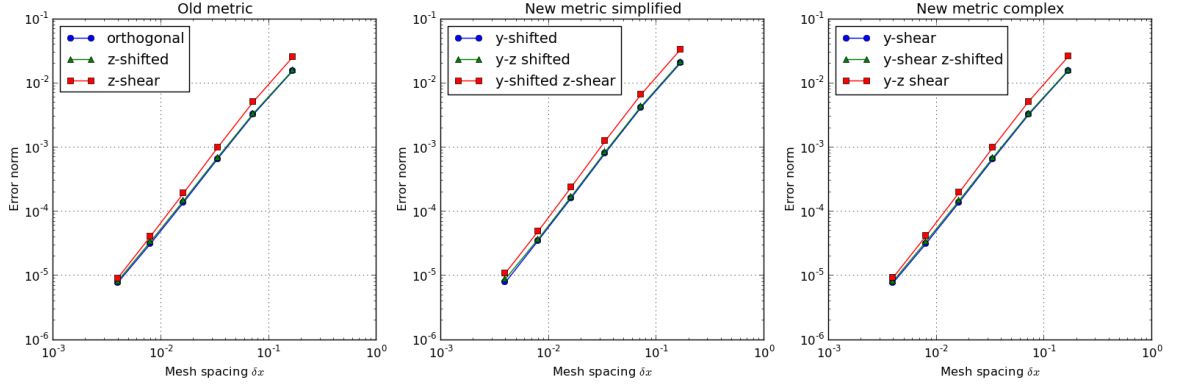
Figure 5.6: Second order convergence demonstrated by all metric tests: (left) the old metric with a orthogonal poloidal plane, (center) constant non-orthogonality in the poloidal plane, (right) and varying non-orthogonality in the poloidal plane. These correspond to the three grids shown in figure 5.5.

complexities demonstrate at least 2nd order convergence with Dirichlet boundary conditions. Figure 5.6 shows the error norm, defined as the root mean squared error between f and F over the entire grid, as a function of grid spacing. The slope of the lines on these graphs indicates the order of convergence for the numerical methods in use in the simulation. Similar convergence of at least 2nd order is seen for the newly implemented Neumann boundary conditions, as well (not shown).

Table 5.1: Numerical scheme ordering as converged from 8x8x8 to 64x64x64 using the MMS. Columns indicate non-orthogonality in the x-y plane and rows describe non-orthogonality in the y-z plane.

	Orthogonal $(\eta = 0)$	Poloidal pitch $(\eta = 0.2)$	Poloidal shear $(\eta = f(\psi, \theta))$
No pitch $(\nu = 0)$	2.00	2.14	2.00
Constant pitch $(\nu = 0.1)$	2.02	2.04	2.02
Shear $(\nu = 0.1x)$	2.14	2.14	2.13

The x-y grids used for these MMS verification tests can be seen in figure 5.5. Though the z-direction is not pictured, the 3-D location of the grid points is calculated through the pitch ν and non-orthogonality factor η according to equations 5.13a, 5.16, and 5.19. The field line pitches used for the test cases are $\nu = 0$ for the orthogonal case, $\nu = 0.1$ for the constant field line pitch case, and $\nu = 0.1x$ for the magnetic shear case, with $x \in [0, 1]$. The y-grid spacing for the third grid (figure 5.5c) is defined

by $y = \theta + b(0.5 - x)\sin\theta$, where θ is equally spaced in $[0, 2\pi]$, and b determines the amount of non-orthogonality ($b = 0.1$ for this case). With this expression for y, there is no analytic form for η so it was calculated numerically.

5.4.2 Wave simulation

A simple wave equation is simulated on the three grids shown in figure 5.5, which cover the same physical space with different levels of non-orthogonality. The wave equations are as follows

$$
\begin{aligned}
\frac{\partial f}{\partial t} &= v\nabla_{\parallel} g \\
\frac{\partial g}{\partial t} &= v\nabla_{\parallel} f.
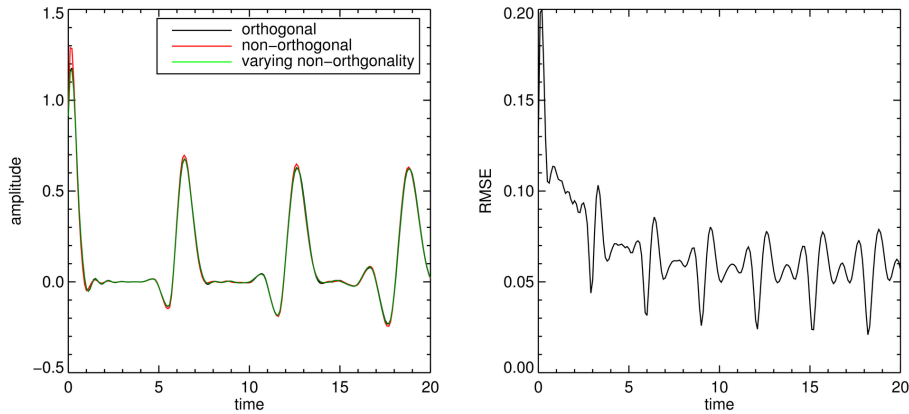\end{aligned}
\tag{5.41}
$$

Figure 5.7: The value of field f (left) and root mean square error (right) between non-orthogonal and orthogonal simulation results of the wave propagating on the grids in figure 5.5.

A wave propagating in this space should behave the same regardless of the location of the grid points. The results of these simulations, shown in figure 5.7, indicate that the behaviour of the wave on all the grids is very similar. The root mean squared error (RMSE) is taken with the orthogonal case as the reference (ie. correct solution). The largest error is for the non-orthogonal grid, not the varying non-orthogonal, so this is the RMSE shown in figure 5.7. The error decreases until oscillating about a steady, small value.

5.5 Application to divertor physics

In order to simulate physics in a realistic tokamak geometry, a grid generator called Hypnotoad [68] is used to create BOUT++ meshes from EFIT equilibria [127]. This generator had to be modified (done by B. Shanahan) in order to create non-orthogonal meshes, and the calculations for the metrics are included in post-processing of the grids.

5.5.1 Grid generation and processing

Before the derivation of the new coordinate system, BOUT++ utilised a standard field-aligned coordinate system requiring simulation meshes like that seen in figure 5.8a. However, the mesh can now be constructed to match the geometry of the divertor as shown in figure 5.8c, allowing for more accurate simulations of the physics in this region. The x-point can also be more clearly resolved by maintaining a regular grid spacing in the poloidal plane around it, creating a Cartesian-like grid in this area (thanks to M Umansky and M Dorf). If this were attempted using the standard field-aligned coordinates, the spacing at the edges would become very small, limiting the time step due to the CFL condition [29] mentioned in 1.3.1.1.

There are significant differences in these two grids at the divertor leg and also at the X-points. The changes to the x-points are another benefit of this new coordinate system because it allows a more regular distribution of grid spacing in y in this region, which increases the stability of simulations taking them further from the Courant-Freidrichs-Lewy condition limit and increasing the speed of the simulations. The non-orthogonality of the new mesh is captured in the value η, which can be seen contoured in figure 5.9. It was not as straight-forward to calculate η for these realistic meshes as it was for the meshes in figure 5.5 created for the MMS verification. In the generation of those grids, θ was defined and y was derived from the by setting the value of y_{shift} analytically and utilising equation 5.16. This process, however, is not possible for the realistic tokamak geometries, so η needs to be calculated from the layout of the grid as produced by the grid generator. This is done by realising that the non-orthogonality factor $\eta = \sin\beta$ where $\frac{\pi}{2} - \beta$ is the local angle between y and x. In this way, Hypnotoad
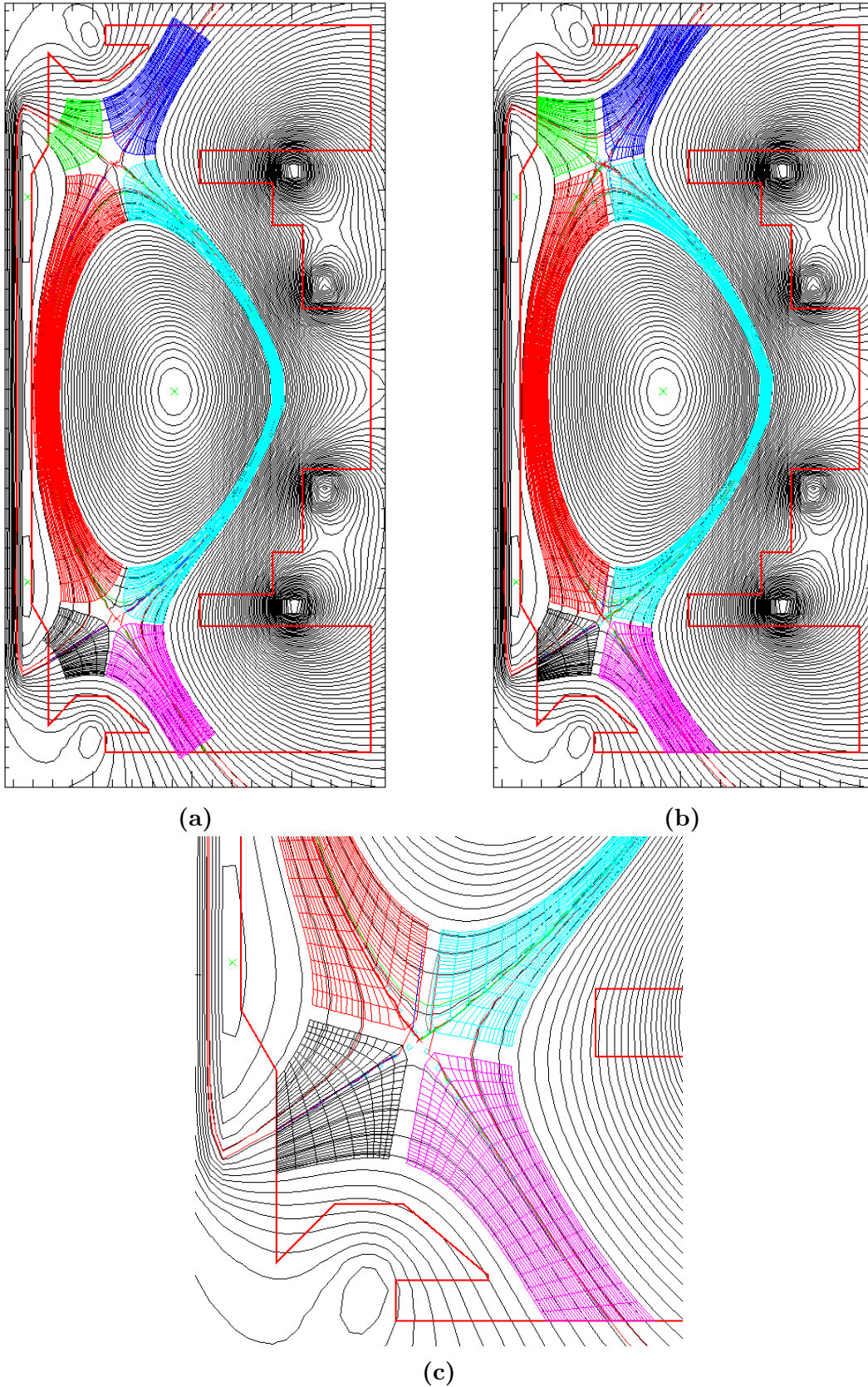
Figure 5.8: (a) Orthogonal in the poloidal plane, this mesh cannot extend all the way to the divertor plate. (b) This grid does extend to the divertor plate, but requires the new metric derived above. (c) The Cartesian nature of the x-point grid can be seen when the picture is zoomed for the new coordinate system case. The slow change from orthogonal to non-orthogonal in the divertor leg as the plate is approached can also be seen.
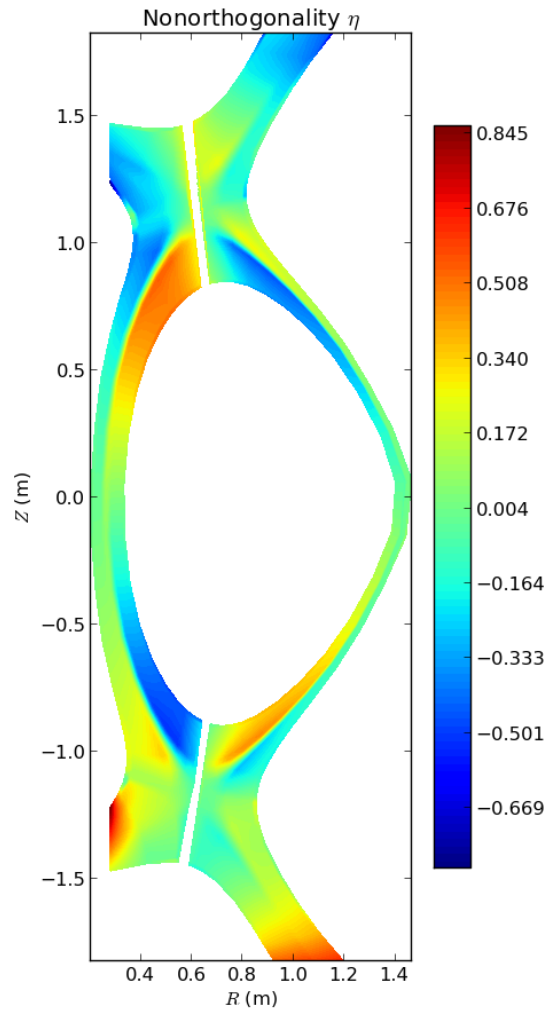
Figure 5.9: The non-orthogonality factor, η, is contoured onto the MAST mesh to highlight the differences between this mesh and the old one around the divertors and x-points.

was modified to include the calculation of β and η for each grid point, allowing for the calculation of the full metric tensors.

These meshes are constructed based on an EFIT [127] equilibrium reconstruction for the MAST tokamak in the Culham Centre for Fusion Energy (CCFE). An L-mode plasma is simulated with the pedestal temperature at the inner boundary set to 100eV and the edge to 10eV, the core density to 10^{19}m^{-3} and edge density to 10^{18}m^{-3}, and the velocity boundary conditions set to the initial Bohm speed.

5.5.2 SimCat model

There are many three-dimensional turbulence models that have been derived for simulation of tokamak plasmas [121]. Since the non-orthogonal coordinate system is ideal for simulating the edge and divertor, it is sensible to choose a drift-reduced model, as determined in chapter 3. In addition to this, the edge is very collisional due to the low temperatures and densities so one might consider the drift-reduced Braginskii model derived by Mikhailovskii and Tsypin [28]; however, this model is missing various contributions from the viscous stress tensors - a problem that was corrected by Simakov and Catto [103]. It is this system, then, that will be considered for 3-D divertor and edge simulations in the following sections and chapters.

The Simakov and Catto model (dubbed SimCat) is a system is derived to describe field-aligned fluctuations in the low-beta collisional magnetised plasma edge region. This implies the follow assumptions:

$$k_\perp \rho_j \ll 1 \qquad \text{and} \qquad k_\parallel \lambda_j \ll 1 \tag{5.42}$$

where ρ_j is the larmor radius of species $j = e, i$ and $\lambda_j \equiv v_{Tj}/\nu_j$ is the mean-free path with the thermal speed $v_{Tj} = \sqrt{2T_j/m_j}$ and the collision frequency $\nu_j = \tau_j^{-1}$ is the inverse of the collision time as given in equation 1.8. Essentially, these assumptions mean that the plasma features along the field line are much larger than the mean free path, and that the plasma features perpendicular to the field line are much larger than the Larmor radius.

Though the SimCat system conserves energy, it has been modified by Ben Dudson so as to be more amenable to flux-conservative numerical implementation. The equation to evolve density includes $\vec{E} \times \vec{B}$ advection, parallel flows, curvature effects, diffusion, and a source term.

$$\frac{\partial n}{\partial t} = -\vec{\nabla} \cdot \left(n\hat{b} \times \frac{\nabla\phi}{B}\right) - \nabla_{\parallel}(nv_{i\parallel}) - \vec{\nabla} \cdot \left(-nT_e\hat{b} \times \vec{\kappa}\right) + \vec{\nabla}_{\perp} \cdot (D_n\nabla n) + S_n \qquad (5.43)$$

where n is particle number density (electron and ion assumed equal due to quasi-neutrality), $\hat{b}$ is the unit vector pointing in the direction of the magnetic field, ϕ is the electrostatic potential, B is the magnetic field, $v_{i\parallel}$ is the parallel ion velocity, T_e is the electron temperature, κ is curvature, D_n is the density perpendicular diffusion constant (calculated with coefficients given in section 1.3.1), and S_n is a density source term. For the evolution of the parallel vorticity, ϖ, the following terms are included: $\vec{E} \times \vec{B}$ advection, parallel current gradients, curvature and diffusion.

$$\frac{\partial \varpi}{\partial t} = -\vec{\nabla} \cdot \left(\varpi\hat{b} \times \frac{\nabla\phi}{B}\right) - \nabla_{\parallel}\left[n\left(v_{e\parallel} - v_{i\parallel}\right)\right] - \vec{\nabla} \cdot \left(-nT_e\hat{b} \times \vec{\kappa}\right) + \vec{\nabla}_{\perp} \cdot (\mu\nabla\varpi) \qquad (5.44)$$

where $v_{e\parallel}$ is the parallel electron velocity and μ is the perpendicular diffusion coefficient. Instead of evolving the magnetic flux perturbations, a quantity $v_{e\psi} = v_{e\parallel} + \frac{1}{2}\frac{m_i}{m_e}\beta_e\psi$ is instead evolved to convert Ohm's law into an ordinary differential equation, where m is the mass of the species and β_e is the electron beta (ratio of magnetic to gas pressure).

$$\frac{\partial v_{e\psi}}{\partial t} = \frac{m_i}{m_e}\frac{\nu}{n}\left(J_{\parallel} - J_{\parallel 0}\right) + \frac{m_i}{m_e}\nabla_{\parallel}\phi - \frac{m_i}{m_e}\frac{1}{n}\nabla_{\parallel}p_e - 0.71\frac{m_i}{m_e}\nabla_{\parallel}T_e \qquad (5.45)$$

where ν is the collisional damping frequency, $J_{\parallel}$ is the current density, and p_e is the electron pressure. The parallel ion flux is evolved taking into account $\vec{E} \times \vec{B}$ advection and parallel flows due to density and pressure gradients.

$$\frac{\partial(nv_{i\parallel})}{\partial t} = -\vec{\nabla} \cdot \left(nv_{i\parallel}\hat{b} \times \frac{\nabla\phi}{B}\right) - \nabla_{\parallel}\left(nv_{i\parallel}^2\right) - \nabla_{\parallel}p_e \qquad (5.46)$$

Finally, the electron pressure is evolved (ie. temperature since $p_e = n_eT_e$) including $\vec{E} \times \vec{B}$ advection, parallel advection, curvature effects, terms coming from $\vec{\nabla} \cdot \pi_{ij}$ (the

divergence of the pressure tensor), and a source term for adding or removing energy from the system. The ion temperature is assumed to be zero, which simplifies the stress tensor described in section 1.3.1.

$$\frac{3}{2}\frac{\partial p_e}{\partial t} = -\frac{3}{2}\vec{\nabla} \cdot \left(p_e\hat{b} \times \frac{\nabla\phi}{B}\right) - \frac{5}{2}\nabla_{\|}\left(p_e v_{e\|}\right) - \frac{5}{2}\vec{\nabla}\cdot\left(-p_e T_e \hat{b} \times \vec{\kappa}\right) + \vec{\nabla}\cdot\left(\kappa\nabla_{\|}T_e\right)$$
$$+ \frac{3}{2}\vec{\nabla}_{\perp}\cdot\left(D_n \nabla n T_e\right) + S_p \tag{5.47}$$

where κ is the parallel electron thermal conductivity and S_p is the pressure/power source. To close the system the following relationships are defined:

$$\nabla_{\perp}^2\psi = n\left(v_{i\|} - v_{e\|}\right) = J_{\|}$$
$$\varpi = \vec{\nabla}\cdot\left(\frac{n}{B^2}\nabla_{\perp}\phi\right) \simeq \frac{n_0}{B^2}\nabla_{\perp}^2\phi \tag{5.48}$$
$$T_e = \frac{p_e}{n}$$

The equation that relates vorticity to the electric potential is often inverted to solve for potential. This is computationally difficult, which often leads to a simplification of the equation, called the Boussinesq approximation, which assumes the density perturbations are small compared to the background density. The density can then be pulled out of the divergence, resulting in a perpendicular Laplacian of the potential, which can more easily be inverted. The drawbacks of this are that the density perturbations in the scrape-off layer plasma are often *not* much smaller than the background plasma density, with $\frac{\delta n}{n_0} \sim 1$.

5.5.3   2-D transport model

The SimCat model can be simplified to include only perpendicular and parallel transport via diffusion, conduction, and convection. This is a useful tool for initialising a full turbulence run and also to check the basic behaviour of a system. The reduced equations are

$$\frac{\partial n}{\partial t} = -\nabla_{\|}\left(nv_{i\|}\right) + \vec{\nabla}_{\perp}\cdot\left(D_n\nabla n\right) + S_n$$
$$\frac{\partial(nv_{i\|})}{\partial t} = -\nabla_{\|}\left(nv_{i\|}^2\right) - \nabla_{\|}p_e \tag{5.49}$$
$$\frac{3}{2}\frac{\partial p_e}{\partial t} = -\frac{5}{2}\nabla_{\|}\left(p_e v_{i\|}\right) + v_i\nabla_{\|}p_e + \vec{\nabla}\cdot\left(\kappa\nabla_{\|}T_e\right) + \frac{3}{2}\vec{\nabla}_{\perp}\cdot\left(D_n\nabla p_e\right) + S_p$$

This system can be simulated in two-dimensions to evolve the flows within the system, but turbulence and electric effects (such as $\vec{E} \times \vec{B}$ drifts) are absent. Sheath conditions are used for the boundary in contact with the divertor plate according to the constraints given by Loizu [128]. The ion velocity at the plate is assumed to be the sound speed, as described by the Bohm criterion, and this is then related to the electron velocity.

$$v_i = c_s = \sqrt{\frac{T_e}{m_i}} \tag{5.50}$$

The electron temperature is assumed to have zero gradient at the divertor allowing no flow of heat to the plates.

$$\nabla_\parallel T_e = 0 \tag{5.51}$$

The density and velocity gradients are set by assuming the gradient of the ion flux is zero.

$$\nabla_\parallel n = -\frac{n}{c_s} \nabla_\parallel v_i$$
$$\nabla_\parallel \phi = -c_s \nabla_\parallel v_i \tag{5.52}$$

Finally, the pressure gradient is set by assuming zero temperature gradient and $p_e = nT_e$.

$$\nabla_\parallel p_e = T_e \nabla_\parallel n \tag{5.53}$$

5.5.3.1 Results

After evolving the system above for 10^3 cyclotron times (~ 0.01 seconds), steady state was reached. Figure 5.10 shows the density, temperature, and Mach number of the plasma in steady state. The density and temperature confinement is easily seen in the temperature and density where the field lines are closed. Plasma that has diffused perpendicularly across the separatrix then flows down to the primary divertors. Any density that diffuses perpendicularly further, past the secondary separatrix flows up to the secondary divertors.
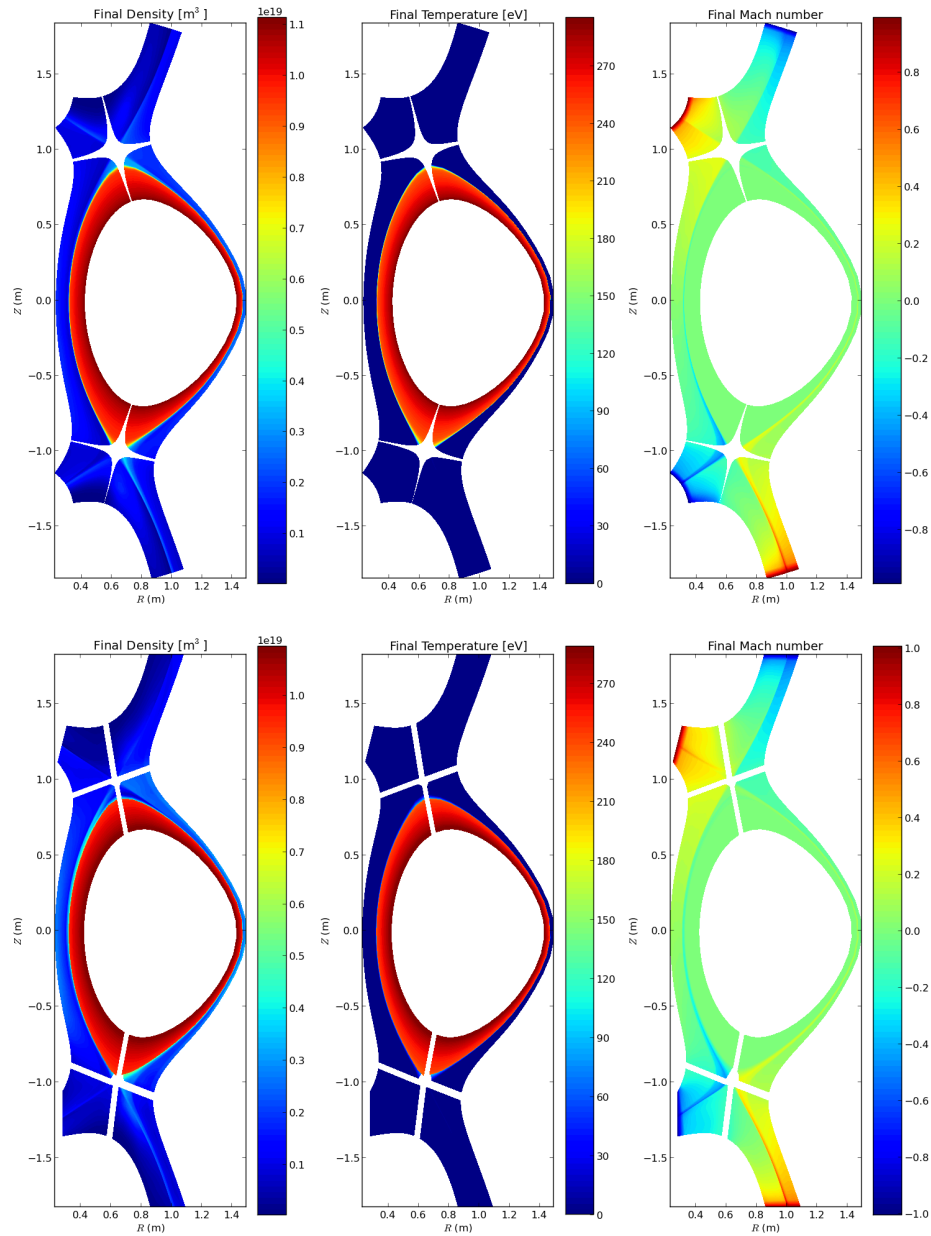
Figure 5.10: The density, temperature, and Mach number are shown for the orthogonal (top) and the new non-orthogonal (bottom) grids. The qualitative behaviour is very similar, as expected.
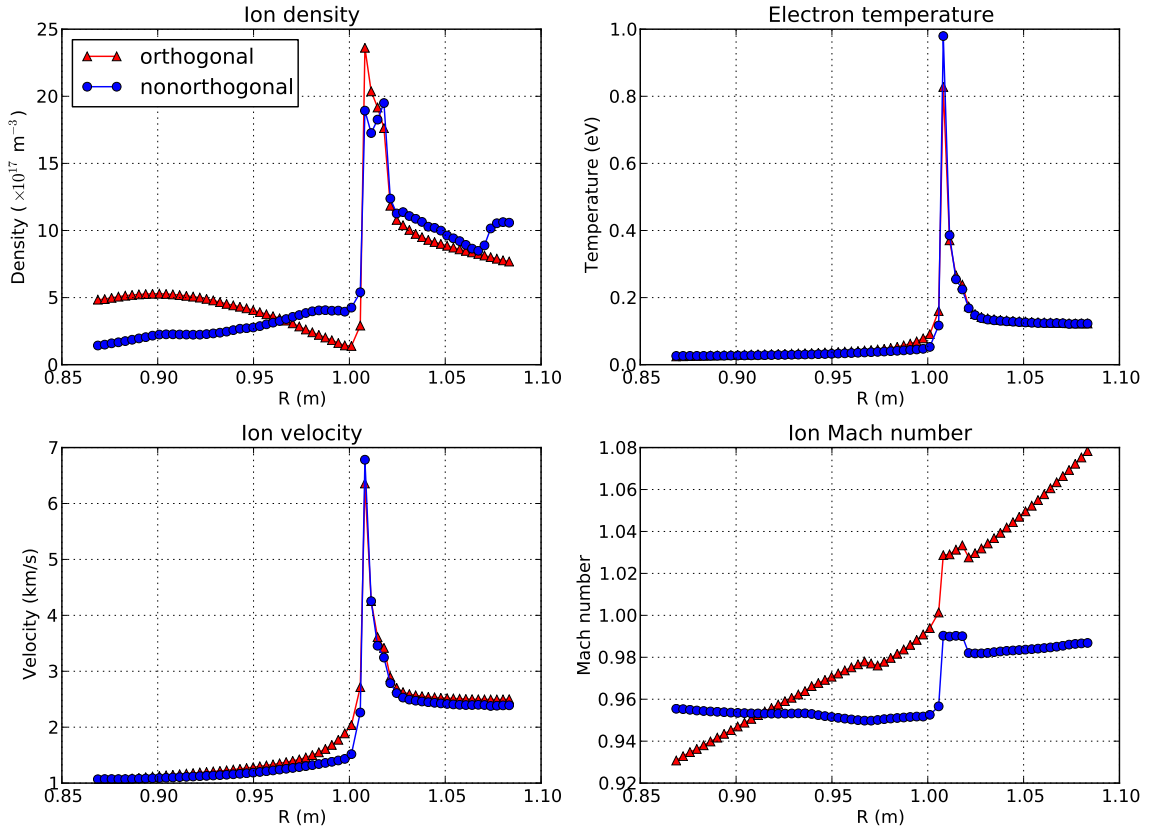
Figure 5.11: The density, temperature, parallel velocity, and Mach number profiles are shown for both the orthogonal (red) and non-orthogonal (blue) grids.

The Bohm boundary conditions set the Mach number to 1 in the last grid cells in the y-direction. For the non-orthogonal case this corresponds to the divertor plate, but for the orthogonal grid, this lies in an arbitrary distance form the plate, so values must be extrapolated and scaled based on the flux expansion, $\dfrac{B_\phi}{B_\theta}$, to obtain the quantitative results at the divertor plate. Figure 5.11 shows the density, temperature, parallel velocity, and Mach number at the strike point for both the orthogonal and the non-orthogonal grids. The density, temperature, and velocity are very similar, while the Mach number shows a background linear profile for the orthogonal grid which is due the boundary conditions being set at the last grid cells, but the grid itself being at an angle to the plate. Since the peak temperature is higher for the non-orthogonal case, the ion velocity is also higher to maintain a unity Mach number.

At the core edge the density and temperature are held constant at $10^{19} \mathrm{m}^{-3}$ and 295eV, respectively, to replicate the pedestal. The density drops at the plate to a value around 2×10^{18} and the temperature to only 1eV. If neutrals interactions existed in the divertor region, plasmas of this temperature would be dominated by charge exchange reactions
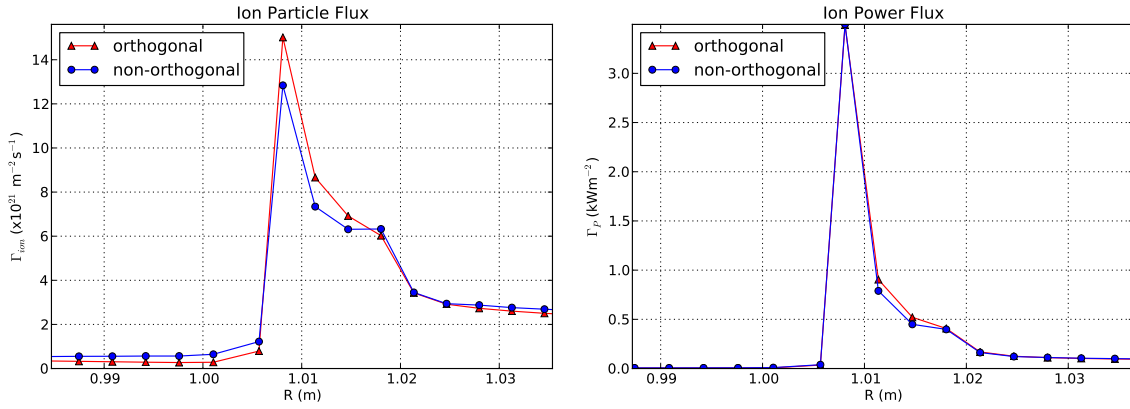
Figure 5.12: The particle (left) and power (right) fluxes are shown for both the orthogonal (red) and non-orthogonal (blue) grids.

and detachment would occur. Since there are no neutrals, however, the low temperature and density lead to small ion and power fluxes, which are calculated by

$$\Gamma_{\text{ion}} = n_i v_i$$
$$\Gamma_{\text{P}} = \left(\frac{1}{2} m_i v_i^2 + \frac{3}{2} e T_i\right) n_i v_i. \tag{5.54}$$

The resulting fluxes are shown in figure 5.12. Both the particle and power flux are very similar for both the orthogonal and non-orthogonal case, as expected. This affirms the validity of the implementation of the new coordinate system in BOUT++ and allows for more detailed and interesting simulations to be run, such as those including neutrals in the next section.

5.5.4 Amputated divertor leg

The divertor is an especially difficult area of the tokamak to simulate due to the large gradients and complex geometry, so it is sensible to focus computational power on a single leg. In order to isolate the divertor leg, where the non-orthogonality is most pronounced, a grid is produced by amputating the leg from a full diverted plasma grid. For this section the grid is a MAST lower, outer leg, as shown in figure 5.13. For this to be sufficient an approximation for the core density and power fluxes must be made at the top of the leg. This is accomplished by holding the density and temperature constant at the upper boundary in the outer SOL, while allowing the density and temperature to float with zero gradient boundary conditions in the private flux region. The fixed SOL profiles are shown in figure 5.14 and were chosen to have realistic density
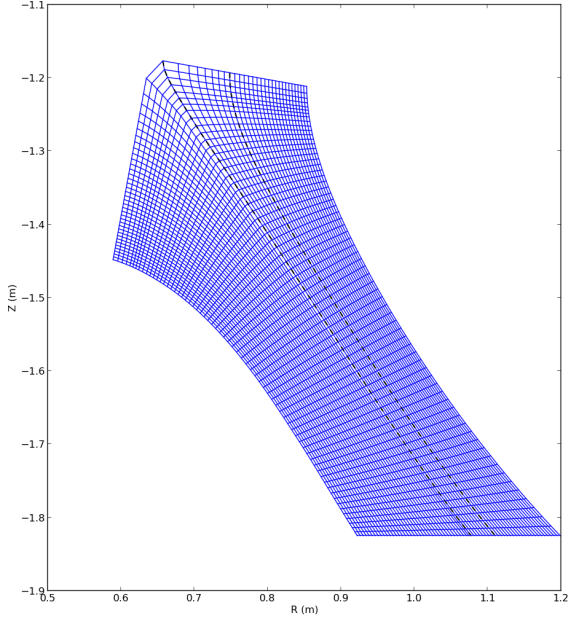
Figure 5.13: The grid displayed is used for the isolated divertor simulations and detachment study, though the resolution is made sparse so the individual grid points can be seen. The inner and outer separatrix are marked by dashed black lines.

and temperature values at the last closed flux surface. These profiles are described by equations for density and pressure

$$n = n_0 \exp\left[-\frac{|x - x_{\text{sep}}|}{\sigma_n}\right] \qquad p = p_0 \exp\left[-\frac{|x - x_{\text{sep}}|}{\sigma_p}\right] \tag{5.55}$$

where $\sigma_p > \sigma_n$ and x_{sep} is the radial position of the separatrix. This results in a profile for the temperature given by

$$T = \frac{p_0}{n_0} \exp\left[-\frac{|x - x_{\text{sep}}|\,(\sigma_p - \sigma_n)}{\sigma_n \sigma_p}\right] \tag{5.56}$$

5.5.4.1   Inclusion of neutrals

The addition of neutrals to the plasma results in plasma-neutral interactions changing the behaviour of the plasma. Four atomic processes are included to describe this interaction: ionisation, recombination, charge exchange and radiation. Ionisation, recombination and charge exchange provide sources and sinks for density, energy, and momentum, each of which can be described by the following density rate coefficients
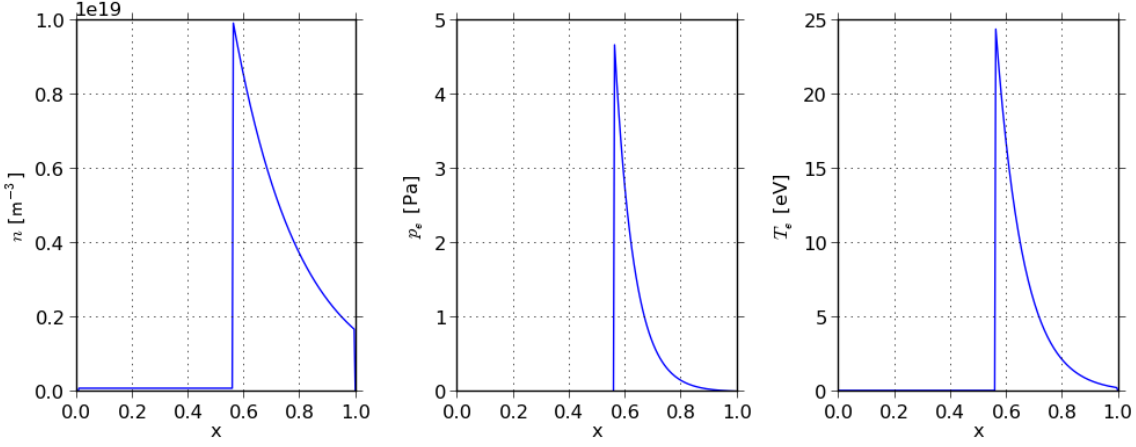
Figure 5.14: These profiles correspond with equations 5.55 and 5.56 where $p_0 = 4.82$Pa, $n_0 = 10^{19}$m^{-3}, $\sigma_n = 0.24$, $\sigma_p = 5.8$, and $x_{\text{sep}} = 0.559$ (x is normalised distance along the divertor leg grid flux surfaces). The density and temperature profiles are fixed, while the pressure is set to have Neumann boundary conditions allowing the flow of energy in and out of the system through the top of the divertor leg.

$(\text{m}^{-3}\text{s}^{-1})$

$$\mathcal{R}_{iz} = nn_n \langle \sigma v \rangle_{iz} \qquad \text{(Ionisation)}$$

$$\mathcal{R}_{rc} = n^2 \langle \sigma v \rangle_{rc} \qquad \text{(Recombination)} \tag{5.57}$$

$$\mathcal{R}_{cx} = nn_n \langle \sigma v \rangle_{cx} \qquad \text{(Charge exchange)}$$

where n is the plasma density, n_n is the neutral density, and $\langle \sigma v \rangle$ is the cross-section $(\text{m}^3\text{s}^{-1})$ for the relevant process which is a function of the plasma temperature. These cross-sections (shown in figure 5.15) are pre-calculated and interpolated from a look-up table within the code. Ionisation increases the plasma density while recombination decreases it, so the resulting density source is described as the difference:

$$S_n = \mathcal{R}_{iz} - \mathcal{R}_{rc} \tag{5.58}$$

Recombination and charge exchange both remove momentum from the ions transferring it to the neutrals. Therefore the sink of momentum is given by

$$F = -m_i \left(v_\parallel - v_{n\parallel} \right) \left(\mathcal{R}_{rc} + \mathcal{R}_{cx} \right) \tag{5.59}$$

where $v_\parallel$ is the parallel ion velocity and F can be described as a friction-like term. Energy is transferred between the ions due to all three plasma-neutral interactive
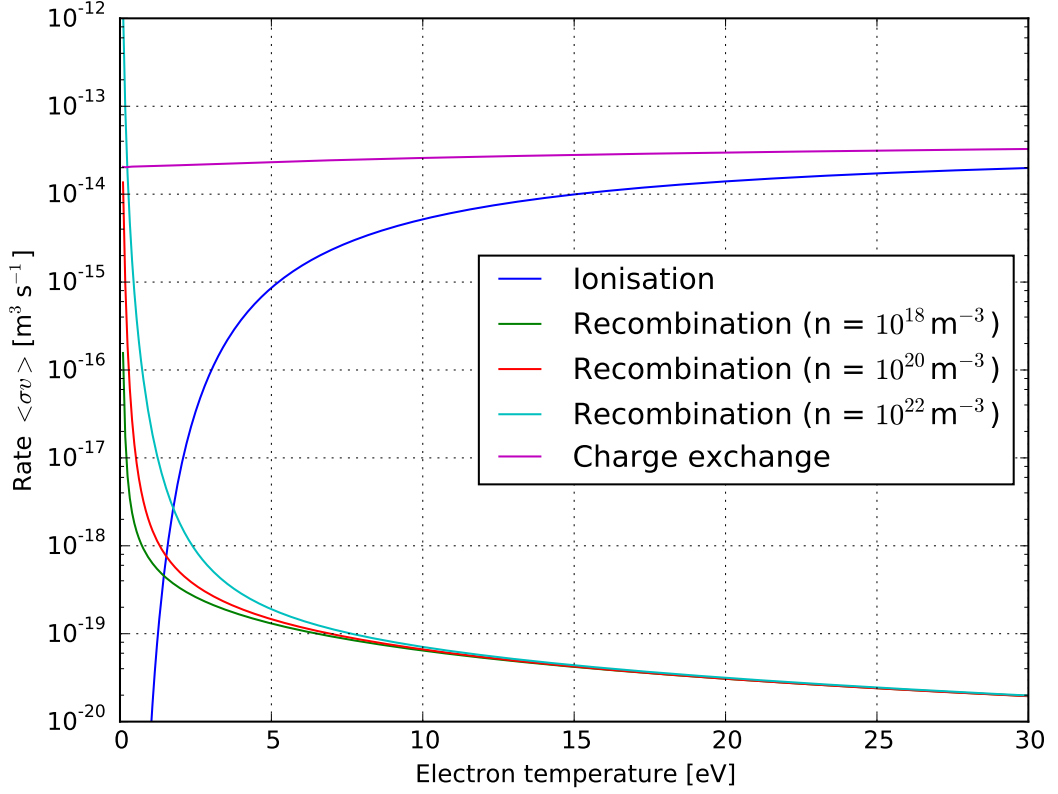
132

Figure 5.15: The cross-section rates for ionisation, recombination, and charge exchange are pre-calculated for hydrogen species as a function of the plasma temperature. Provided by H. Willett at University of York.

processes. Ionisation provides an energy source to the plasma, while recombination removes energy from the plasma. Charge exchange can technically act as a source or a sink for plasma energy depending on the relative temperature difference between the plasma and neutrals; however, it is unlikely for the neutrals to be hotter than the plasma, so in most cases charge exchange acts as a sink for plasma energy.

$$E = \frac{3}{2} T_n \mathcal{R}_{iz} - \frac{3}{2} T_e \mathcal{R}_{rc} - \frac{3}{2} \left(T_e - T_n \right) \mathcal{R}_{cx} \tag{5.60}$$

where T_e is the plasma temperature and T_n is the neutral temperature. The plasma energy is also effected by radiation, which causes a loss of energy through photon emission, and 3-body recombination, which actually heats the plasma at temperatures less than 5.25eV. These two processes are calculated with

$$R = \left(13.6\text{eV} - 1.09 T_e \right) \mathcal{R}_{rc} - E_{iz} \mathcal{R}_{iz} \tag{5.61}$$

133

where $E_{iz} = 30$eV is the ionisation energy given by Togo [129].

In order to calculate the interactions described above, the neutral density and temperature must be known. There are various approximations that can be made for the behaviour of neutrals; however, for these simulations the neutrals have been included rigorously by co-evolving neutral density, pressure, and velocity with a standard system of fluid equations.

$$
\begin{aligned}
\frac{\partial n_n}{\partial t} &= -\nabla \cdot (n_n \mathbf{v}_n) \\
\frac{\partial \mathbf{v}_n}{\partial t} &= -\mathbf{v}_n \cdot \nabla \mathbf{v}_n - \frac{1}{n_n}\nabla p_n + \frac{1}{n_n}\nabla \cdot (\mu \nabla \mathbf{v}) + \frac{1}{n_n}\nabla \left[\left(\frac{1}{3}\mu + \zeta \right) \nabla \cdot \mathbf{v}_n \right] \\
\frac{\partial p_n}{\partial t} &= -\nabla \cdot (p_n \mathbf{v}_n) - (\gamma - 1) p_n \nabla \cdot \mathbf{v}_n + \nabla \cdot (\kappa_n \nabla T_n)
\end{aligned}
\tag{5.62}
$$

where μ, ζ, and κ are constants describing the dynamic viscosity, bulk viscosity, and thermal conduction respectively. For numerical stability, the neutral velocity is shifted to cylindrical coordinates, calculated, and then shifted back into the field-aligned coordinates. This proves more stable and accurate since the neutrals are unaffected by the field lines. The only neutral sources are due to the atomic processes listed above(ie. no gas puffing). The boundary conditions for the neutral are reflecting on the side walls and plate, but allow neutrals to freely flow out of the top of the divertor leg. Figure 5.16 shows neutrals that are generated at the divertor plate due to the plasma flux. These neutrals then stream away from the plasma along the plate and then up the divertor leg. The flow is shown to be cyclic as the neutrals make their way up the leg, back into the plasma where they are accelerated back to the plate. The boundary conditions at the plate and sides of the legs are reflecting for neutrals, but the top of the leg allows outflow.

5.5.4.2   Results

Detachment is seen to occur when the upstream density is high enough for the recycling at the divertor plate to cool the plasma below about 5eV. At this point, the plasma rapidly cools and recombines, forming a cloud of neutrals which helps to radiate the heat away before the plasma reaches the divertor plate. To see this in simulation, first a plasma fluid model (with no currents or neutrals) was run until equilibrium
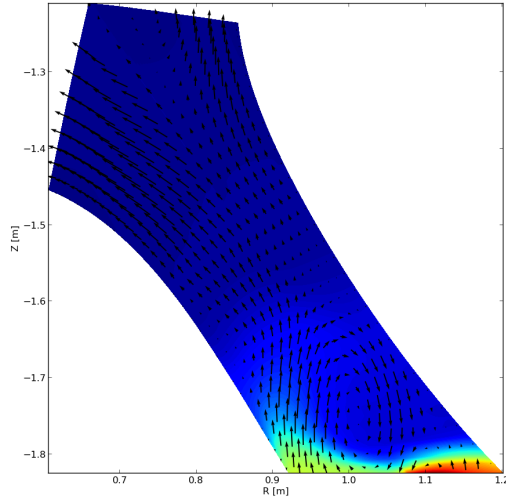
Figure 5.16: The coloured contours show the neutral density and the vectors indicate the flow direction and speed. Neutrals flow away from the point of generation (ie. where the high plasma flux hits the plate) and cycle around the divertor leg.

was reached. The behaviour of the density and temperature should be similar to the two-point model discussed in section 1.3.5.1. Figure 5.17 shows the density and temperature along a field line just outside the separatrix for the steady state fluid simulation and a comparison with the two-point model analytic solution (T_t/T_u versus n_u). The simulation is qualitatively similar but does not give the exact solution to the two-point model; however, this is expected since the two-point model is a simplified view of the behaviour that assumes parallel pressure conservation in a flux tube geometry with no flux expansion, yet the simulation has perpendicular diffusion and flux expansion.

Once steady state is reached in the fluid model, neutrals are added to the simulation and evolved using the fluid equations described in the previous section. The recycling fraction is set to 95% for the following simulations, and the expectation is that the T_t/T_u should move to lower values at higher upstream densities, indicating a detached regime as the neutrals remove energy and momentum from the plasma. Figure 5.18 shows the parallel profiles of density and temperature before and after neutrals are added, and a clear drop in temperature is seen as well as a rise in plasma density near the plate due to ionisation.

Figure 5.19 shows how the introduction of neutrals affects the T_t/T_u curve - clearly, the neutrals are cooling and slowing the plasma through collisions and atomic processes. Simulations with upstream density over 10^{19}m^3 were unable to complete due to numer-

Figure 5.17: Density and temperature are shown (left) to decrease towards the divertor plate. The ratio of the target temperature to upstream temperature, as a function of upstream density, is seen to be similar to the two-point model prediction.
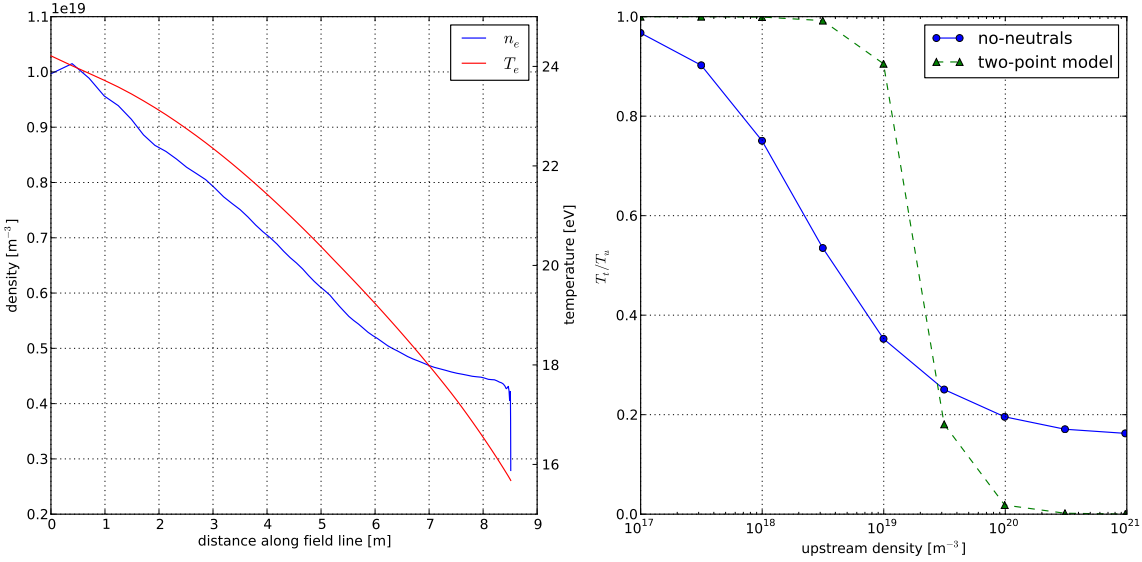

Figure 5.18: Density and temperature are shown (left) to decrease towards the divertor plate. The ratio of the target temperature to upstream temperature, as a function of upstream density, is seen to be similar to the two-point model prediction.
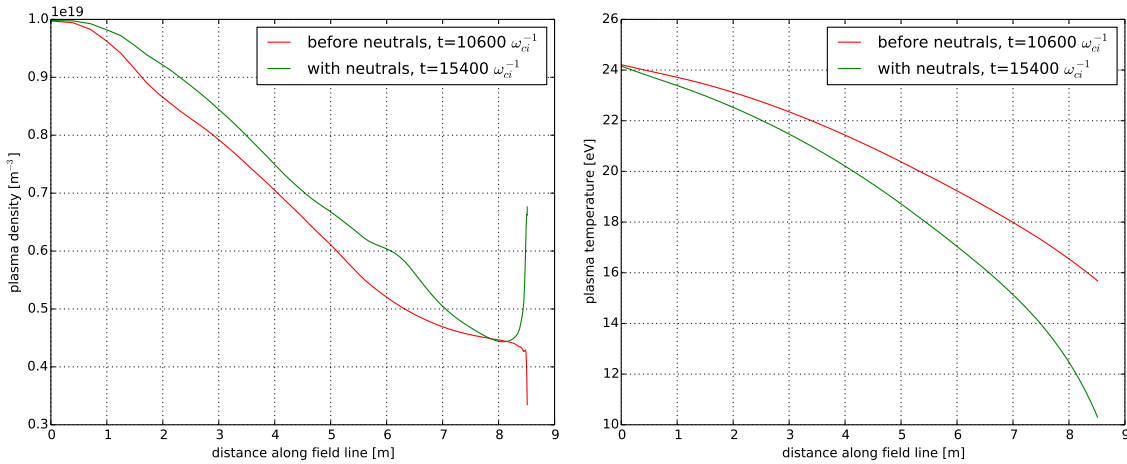
ical instability. The mean-free path of the neutrals decreases as a function of density, so with higher density, the resolution requirement is significant near the plate where the neutrals are initially formed. By generating new grids with increased resolution in this region, the simulations were pushed to later time steps, but ultimately they still crashed with peaked neutral pressure profiles near the plate.

Leading up to the crashes, the simulations show decreasing plasma temperature and increasing neutral density. This is in line with the expectations, unfortunately none of these simulations show the transition into actual detachment where the electron
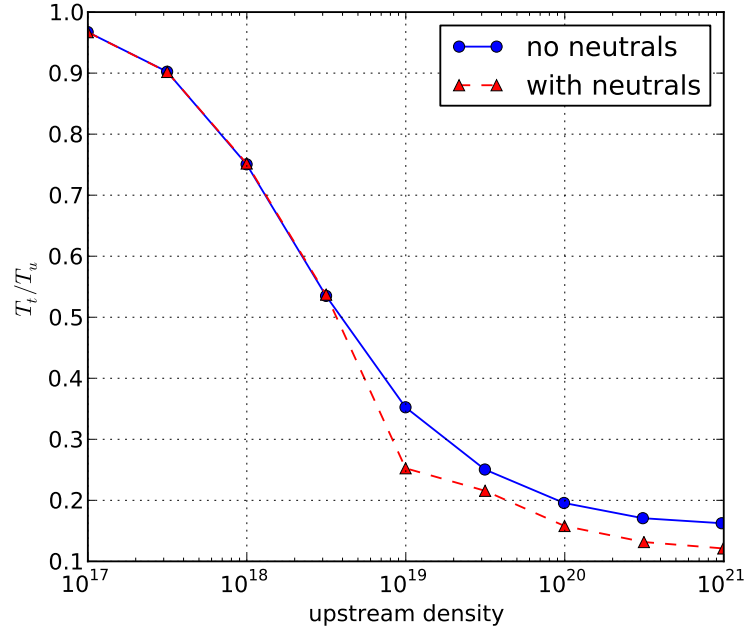
Figure 5.19: Without neutrals, the figure is the same as the right plot in figure 5.17. Once neutrals are added, the temperature at the plate falls and the plasma is cooled as it approaches detachment.

temperature and density (ie. pressure) drop to 1-2 orders of magnitude at the plate due to the generation of a dense cloud of neutral gas.

5.6   Conclusion

A novel coordinate system has been developed to address multiple issues surrounding the use of standard field-aligend coordinates. This new system has been tested using the method of manufactured solutions and then implemented in the BOUT++ code. The implementation of this new system enables more detailed divertor simulations to be run, focusing on a single divertor leg. In these simulations, a fluid neutral model was evolved and the interactions between the neutrals and the plasma were described by ionisation, recombination, charge exchange, and radiation. Running the simulations without neutrals shows a T_t/T_u vs n_u curve that qualitatively agrees with the two-point model described in the introduction. When neutrals were added, the ratio drops at higher upstream densities, as a detached regime is approached.

Chapter 6

Toroidal Edge And Core Unification Program

6.1   Introduction to integrated code

As stated in chapter 2, the purpose of integrating two codes is to obtain a more accurate and complete simulation of a complex system using multiple subsidiary codes that are specialised and have been individually been benchmarked. The toroidal edge and core unification program (TEACUP) integrates BOUT++ and CENTORI to simulate the edge and core, respectively, of tokamaks. Though it is possible to do this in a single code, this approach allows flexibility between the two distinct regions of the tokamak - physics models, numerical methods, etc. can differ for each. Figure 6.1 describes the basic operation of TEACUP as it initialises and simulates both regions in an integrated way.

TEACUP is written in IDL and is a code that manages the initialisation, simulation, and inter-communication of BOUT++ and CENTORI. The initial step is to supply input parameters for both codes, though this is done with a single input file. The parameters for the core simulation include time step, number of grid points for each dimension, initial plasma current, initial velocity profile, and many others. The edge has choices for boundary conditions, resolution for each dimension, numerical methods for differentiation and Laplacian inversion, and more. When these are supplied to TEACUP, two separate input files are created for the core and edge in the proper format for each individual code.
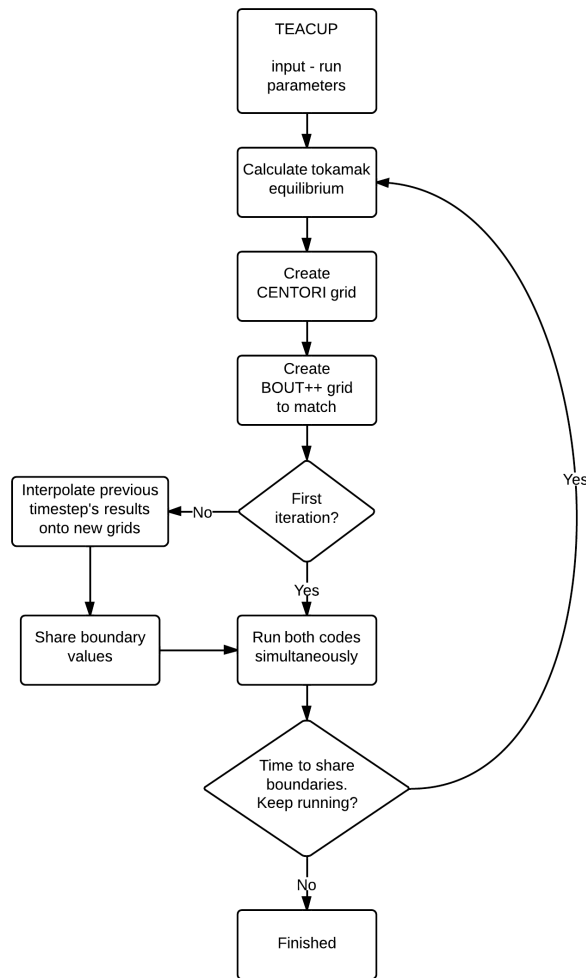
Figure 6.1: Flowchart depicting the operating procedure for TEACUP as an interface between BOUT++ and CENTORI.

CENTORI, as discussed in section 2.3.2, utilises a Grad-Shafronov solver to calculate the equilibrium flux surfaces based on magnetic coil locations and currents and then generates a simulation grid based on this equilibrium, shown in figure 6.2a. BOUT++ then uses this same equilibrium calculation to create its own grid shown in figure 6.2c using a grid generation tool, Hypnotoad, created by Ben Dudson. In this way, the entire tokamak cross-section is filled with grid points for the joint simulation.

The two codes are then automatically set to run individual simulations with these complimentary grids. After a user-defined simulation time, the codes stop and share their data. Many tests, discussed later in this chapter, have been done to determine the optimal time between sharing the boundary data and the method for this sharing. After the boundary data have been interpolated and communicated, the codes they are set running again. Optionally, this can involve a recalculation of the equilibrium
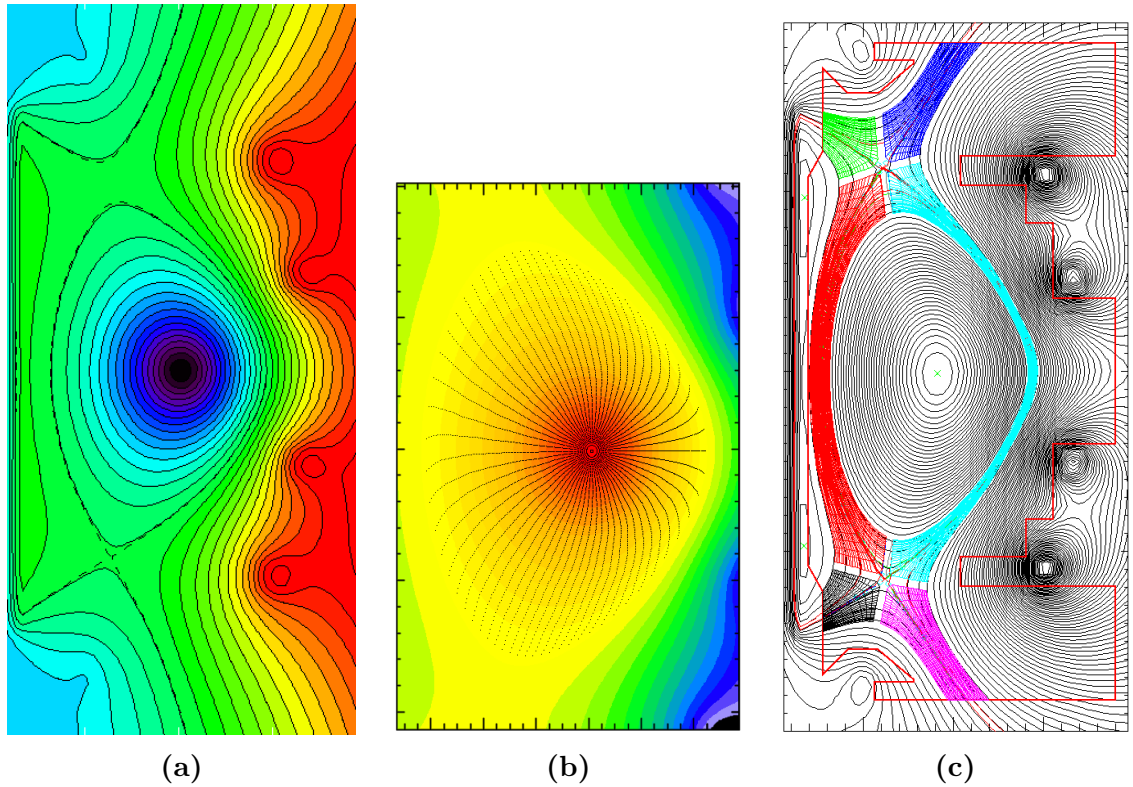
Figure 6.2: The process of grid generation from (a) CENTORI Grad-Shafranov solver calculating the equilibrium, then (b) the grid point creation for the CENTORI core, and finally (c) BOUT++ grid generation with Hypnotoad.

and simulation grids, though this is usually not done every time the boundaries are shared but instead on a longer time scale due to the relatively slow evolution of the plasma equilibrium. This process is repeated as many times as required resulting in a full tokamak plasma simulation that covers the very core to the scrape-off layer and into the divertor. Such simulations are one-of-a-kind for 3D, 2-fluid systems, and are useful for exploring the complicated relationship between the core and edge.

6.2   BOUT++ for the edge

In section 2.3.1 the details of BOUT++ operation and functionality are detailed. BOUT++ can be used to simulate a variety of physics models, and in chapter 3 it is determined that a drift-reduced model is sufficient for describing the edge plasma. In section 5.5.2, the SimCat model, evolving ion flux, ion velocity, electron pressure, and poloidal flux, is explained in detail and is used for divertor and edge plasma simulation.

6.3   CENTORI for the core

CENTORI, as previously mentioned, is a 3D 2-fluid electromagnetic core plasma turbulence code developed at CCFE [30] in 2012 by Peter Knight, et al. It has been benchmarked for reproduction of various linear and non-linear instabilities, including NTMs, kinks, and sawteeth.

6.3.1   Physics model

The CENTORI physics model is a set of equations for both ions and electrons (2-fluid) that uses a unique closure developed specifically for plasma simulations to act as both closure and large eddy dissipation [30], as discussed and analysed in chapter 4. The equations are derived by taking the first 3 moments of the Vlasov-Fokker-Plank (VFP) equation and using Maxwell's equations, a process described in chapter 1. All CENTORI equations are written using Gauss-cgs units.

The zeroth moment of the VFP equation is the mass continuity equation.

$$\frac{\partial \rho}{\partial t} + \vec{\nabla} \cdot (\rho \vec{v}_i) = S_n \tag{6.1}$$

where ρ is the ion mass density, $\vec{v}_i$ is the ion velocity, and S_n is the particle source rate. The first moment of the VFP equation is the momentum equation.

$$\rho \left(\frac{\partial \vec{v}_i}{\partial t} + \vec{W} \times \vec{v}_i \right) = \frac{\vec{J} \times \vec{B}}{c} - \nabla \left(p_i + p_e \right) - \frac{\rho}{2} \nabla \left(\vec{v}_i \cdot \vec{v}_i \right) - \rho \chi_v \left(\vec{\nabla} \times \vec{W} \right) + \vec{S}_v \tag{6.2}$$

where $\vec{W} = \vec{\nabla} \times \vec{v}_i$ is the vorticity, $\vec{J}$ is the current density, $\vec{B}$ is the magnetic field, c is the speed of light, p is the pressure, χ_v is the velocity diffusivity, and $\vec{S}_v$ is the velocity source (ie. neutral beams). This equation is cast in this particular form for ease of numerical implementation; however, it is simply a rearranged version of equation 1.6 shown in section 1.3.1. The second moment of the VFP equation gives the energy equations, one for each species:

$$\begin{aligned} \frac{3}{2} n_e \frac{\mathrm{d}T_i}{\mathrm{d}t} + p_i \vec{\nabla} \cdot \vec{v}_i &= -\vec{\nabla} \cdot \vec{q}_i + S_i \\ \frac{3}{2} n_e \frac{\mathrm{d}T_e}{\mathrm{d}t} + p_e \vec{\nabla} \cdot \vec{v}_e &= -\vec{\nabla} \cdot \vec{q}_e + S_e. \end{aligned} \tag{6.3}$$

where n is the number density (quasi-neutrality is assumed, so $n_e = n_i$), $\dfrac{\mathrm{d}}{\mathrm{d}t} = \dfrac{\partial}{\partial t} + \vec{v} \cdot \nabla$ is a convective derivative, T is the temperature, $\vec{q}$ is the heat flux for each species, and S is a source for addition heating of each species (neutral beam, ECRH, etc.). The equations are then closed using electromagnetic equations, the first of which is Faraday's law.

$$\frac{1}{c}\frac{\partial \vec{A}}{\partial t} = -\vec{E} - \nabla \phi \tag{6.4}$$

where $\vec{A}$ is the vector potential, $\vec{E}$ is the electric field, and ϕ is the electric potential. The vector potential can then be related to the magnetic field.

$$\vec{B} = \vec{\nabla} \times \vec{A} \tag{6.5}$$

Ampère's Law relates the current density to the magnetic field:

$$\vec{J} = \frac{c}{4\pi} \vec{\nabla} \times \vec{B} \tag{6.6}$$

Finally, Ohm's law defines the electric field as

$$\vec{E} = -\frac{\vec{v}_i \times \vec{B}}{c} + \frac{\vec{J} \times \vec{B}}{en_e c} + \eta \vec{J} - \frac{\nabla p_e}{en_e} \tag{6.7}$$

where e is the electron charge and η is the resistivity. In this expression the first term is due to ion motion, second term is the Hall term, the third term is resistive current, and the fourth term is due to advection by to perpendicular pressure gradient. To close the system, a few more relations must be defined. The ideal gas law is used to define the pressure

$$p_m = n_e T_m. \tag{6.8}$$

The current density is related to the relative movement of the charged species given by

$$\vec{J} = en_e \left(\vec{v}_i - \vec{v}_e \right). \tag{6.9}$$

The total electrostatic potential is defined using an adiabaticity relationship

$$\phi = \langle \phi \rangle + \langle T_e \rangle \ln \left(\frac{n_e}{\langle n_e \rangle} \right) \tag{6.10}$$

where the angled brackets denote an average over the flux surface (results in a quantity that varies with ψ only). This then relates back to the electric field through Faraday's law, equation 6.4.

6.4 Coupling method

Pairing two individual simulations together to produce a complete simulation of a domain requires that the information at the boundary be communicated. It is unclear, however, what the details of this communication should be. The two considerations for this grid set-up were:

(a) two grids that have exactly one grid spacing between them where the edge of one acts as the boundary cells for the other and vice versa

(b) two grids overlapping in a region with a weighted average of information communicated between them ("handshaking" region [130])

These two options are shown in figure 6.3. The second is more general as the first is simply a special case in which the size of the overlap region goes to zero. For this reason, the system is set-up to have an overlapping region where the simulations are performed separately for the same space. At periodic intervals the information in this region is then interpolated and weighted according to distance from the boundary, as done by Usami *et al.* in [131]. Between the exchanges of information, the boundary conditions are held constant at the value determined by previous exchange.

A cubic spline interpolation, which fits a piece-wise polynomial to go through every point in the data set and also minimise the curvature to avoid over-fitting [132], is used for the 2D slab simulations. However, upon moving to 3D toroidal geometry, the interpolation must be simplified to a linear method. A sinusoidal weighting function is used to ensure that the solution in the overlapping region is an average of the results
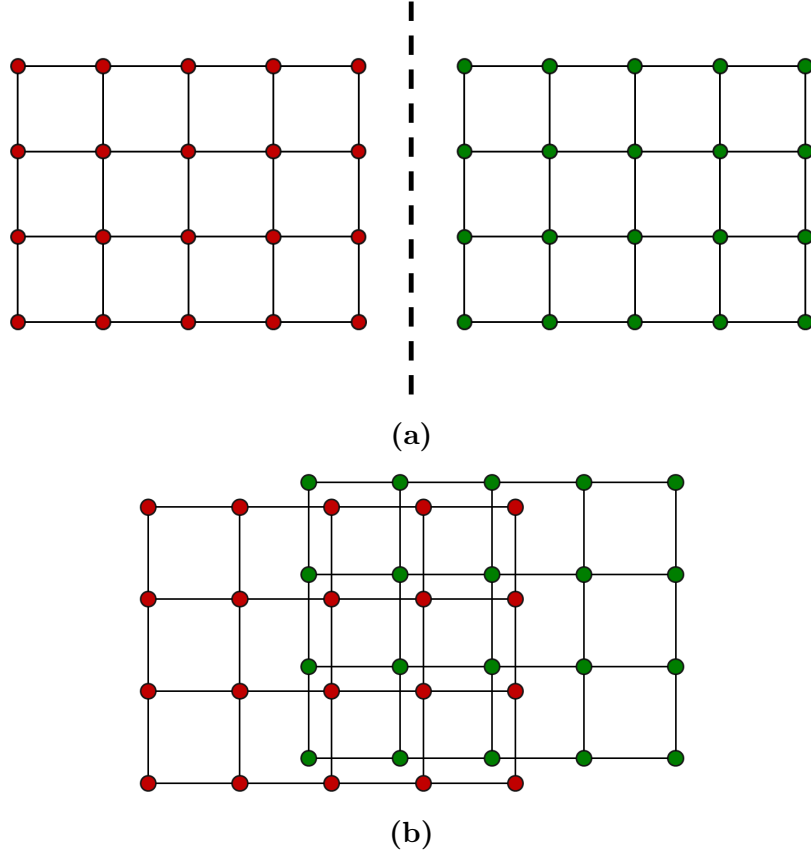
Figure 6.3: Two possible grid set-ups for coupled simulation. (a) The final grid points of each are one grid-space apart allowing them to act as the boundary cell for the other simulation. (b) The two grids overlap such that each simulation finds independent results for the same region that may differ, requiring a weighted average of data to be communicated.

from the two systems and assumes each system is less correct close to its edge. This is chosen over linear because it reduces the numerical noise from the so-called hand-shake scheme [133]. This method ensures the conservation of whatever fields are being interpolated and communicated. The weighting formula is given as

$$f_{\text{result}} = f_L \frac{1}{2} \left(1 + \cos(\pi x)\right) + f_R \frac{1}{2} \left(1 - \cos(\pi x)\right) \tag{6.11}$$

where f_{result} is the weighted average of the simulated quantity f, f_L is the quantity on the left grid, f_R is the quantity on the right grid, and x is the normalised distance along the overlapping region.

This system can easily be adapted for tokamak geometry by assuming x is the radius from the magnetic axis (still normalised over the overlapping region) and the two grids are actually inner and outer instead of left and right. In both cases the weighted average
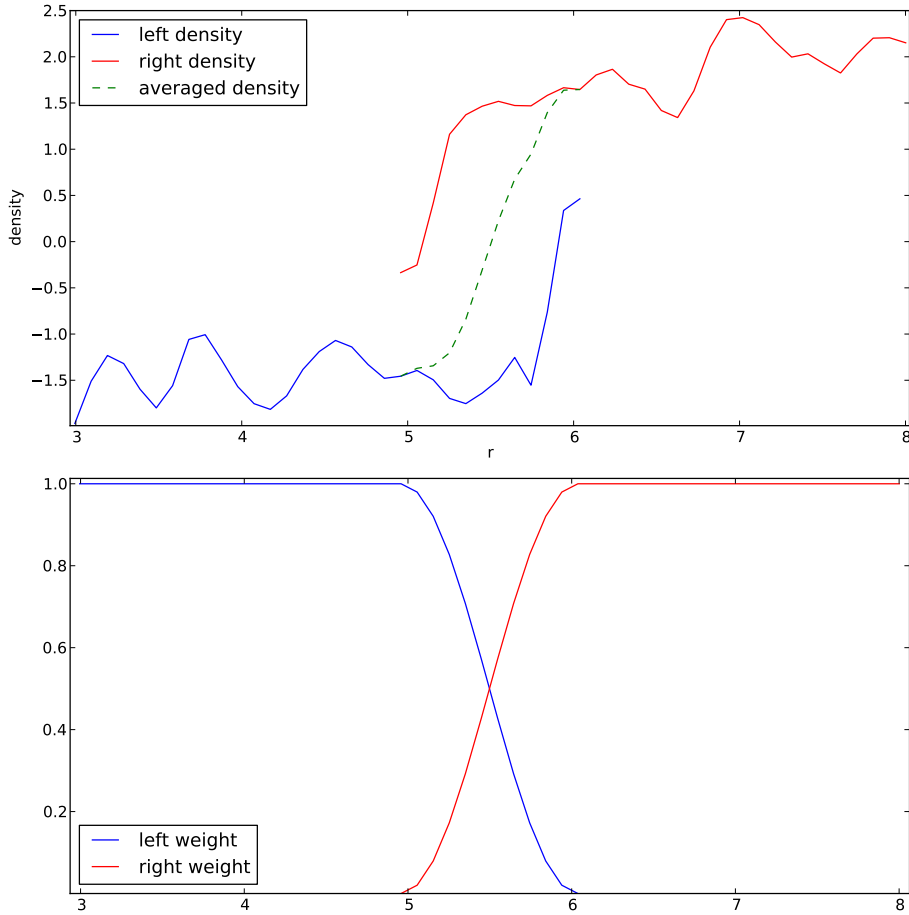
Figure 6.4: The density perturbations have been averaged in the overlapping regions using equation 6.11. The sinusoidal weight functions are shown in the lower plot.

occurs only in one dimension. Figure 6.4 shows the results of using the weighting in equation 6.11 on real simulation data. The extreme disagreement of the data in the overlapping region prior to the weighting is due to the infrequency of communication for this particular example, chosen to clearly demonstrate the weighting.

6.5   BOUT/BOUT benchmarking

As an initial step to investigate the numerical stability and accuracy of pairing codes, two BOUT++ simulations in overlapping regions were paired. This was done in BOUT++ because of the flexibility and ease of modifying the model and geometry that are simulated. This ensured that the accuracy of the coupling was the tested parameter since all other factors were equal. In all of these tests a simulation was run covering a full domain, which serves as the reference. Initially this was done in slab geometry for a simple diffusion model - the simplest possible case. The physics model and the geometry were then made more complex, in turn, to the Hasegawa-Wakatani

model and toroidal, field-aligned geometry, respectively. The amount of overlap and the time between communications are parameters whose effects are investigated in both the slab and toroidal regimes. For the coupled simulations, the domain is divided into two overlapping regions, each of which is simulated individually with boundary updates on regularly spaced time intervals. For the torus, this division is radial corresponding to core/edge coupling. These tests and their results are laid out in the next few sections.

6.5.1   Slab Diffusion

The slab geometry simulated is two-dimensional in the plane perpendicular to the magnetic field with periodic boundary conditions. A simple density diffusion equation is used in the slab geometry,

$$\frac{\partial n}{\partial t} = D_n \nabla^2 n \tag{6.12}$$

where D_n is a diffusion constant set to 0.1 in this case. Given an initial perturbation this system will eventually equilibrate to an isotropic slab of constant density. The results shown in figure 6.5 show that the coupled simulations are within 1% of the simulation over the full domain. This is encouraging, but must be examined in more detail with a more complex system before any conclusions on the stability of the coupling can be drawn.

6.5.2   Slab Hasegawa-Wakatani

The HW model was discussed and utilised in section 4.2, and is again used here for benchmarking purposes. The system is composed of two equations:

$$\begin{aligned} \frac{\partial \xi}{\partial t} &= -\{\phi, \xi\} + \alpha \left(\phi - n\right) + \nu_\xi \nabla^2 \xi \\ \frac{\partial n}{\partial t} &= -\{\phi, n\} + \alpha \left(\phi - n\right) - \kappa \frac{\partial \phi}{\partial y} + \nu_n \nabla^2 n \end{aligned} \tag{6.13}$$

with vorticity $\xi = \nabla^2 \phi$, number density n, plasma electric potential ϕ, adiabaticity parameter $\alpha = \dfrac{T_e \nabla_\parallel^2}{\eta n_0 \omega_{ci} e^2}$, drive coefficient $\kappa = -\dfrac{\partial}{\partial x} \ln(n_0)$, and viscosities ν_ξ and ν_n.

This system produces turbulence assuming $\kappa \neq 0$, giving more complex behaviour to
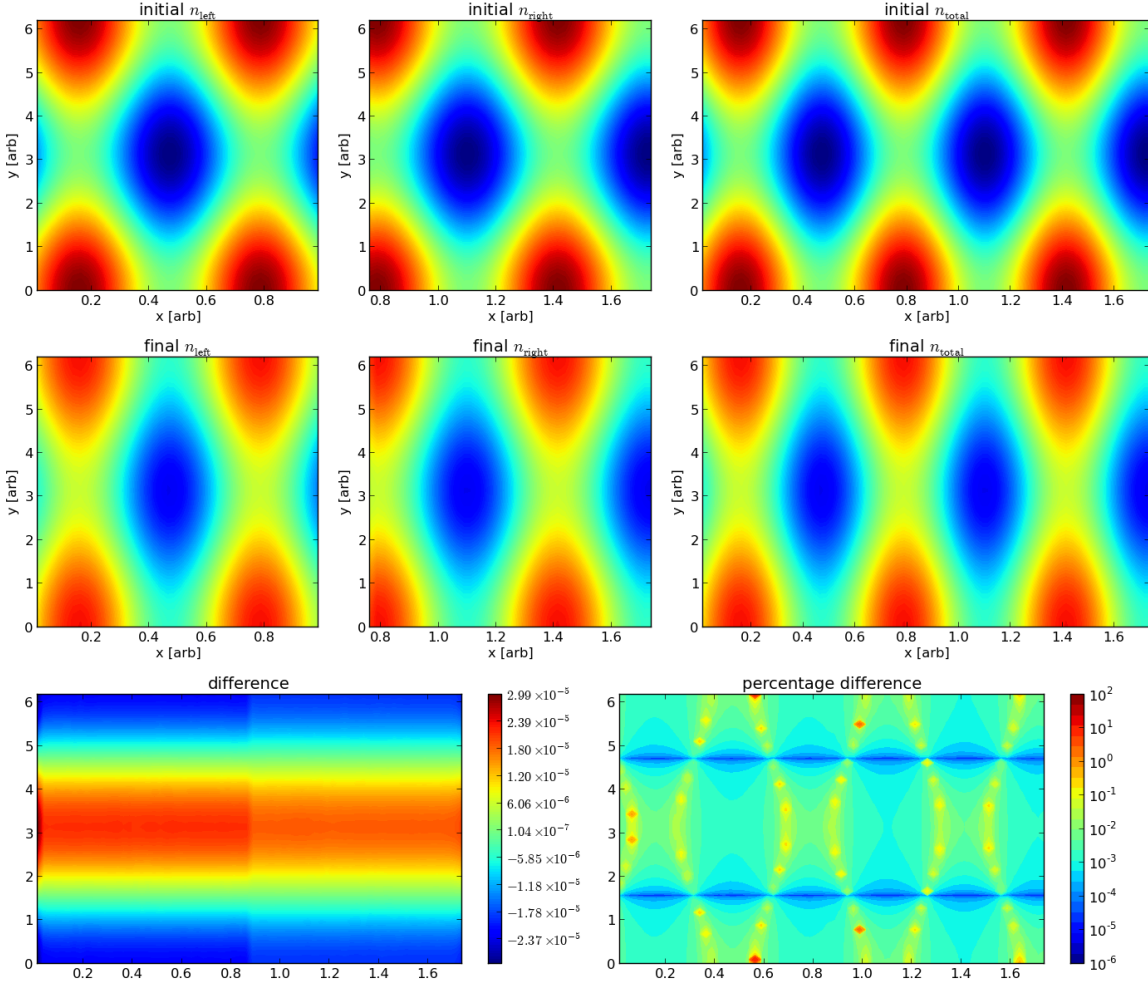
147

Figure 6.5: The results of the diffusion example indicate that the couple simulations and the full simulation show visually identical results at varying points in time. The left grid (left) and right grid (middle) are spliced to make the total grid (right). The results are shown at the initial and an arbitrary final time steps. The absolute difference (bottom left) and percentage difference (bottom right) between the combined solution and the total simulation show that the average error is < 1% and the maximum error is ~ 2%.

test the coupled system. The equations are normalised to the ion cyclotron frequency, ω_{ci}, so the time interval between sharing the data, τ_i, could be set to an actual physically meaningful quantity. What this quantity should be, however, was unknown so a scan was performed to determine the ideal time. It was hypothesised that more frequent sharing would provide more accurate results because as $\tau_i \to 0$ the simulations become a single simulation instead of two separate ones. However, as the data are exchanged more frequently the runtime for the simulation should also increase. Just as in the LES, then, this requires a balance between speed and accuracy.

The amount of overlap can also be adjusted as a free parameter to determine the ideal overlap amount. It is supposed that more overlap should lead to more accurate
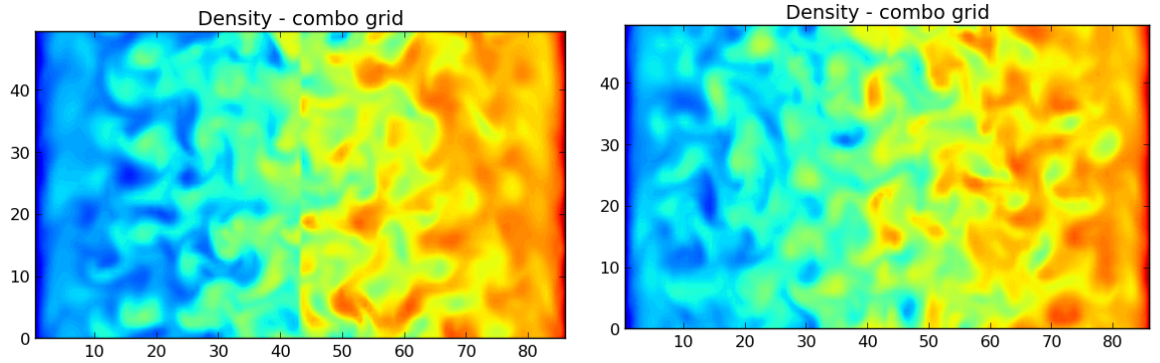
(a)

(b)
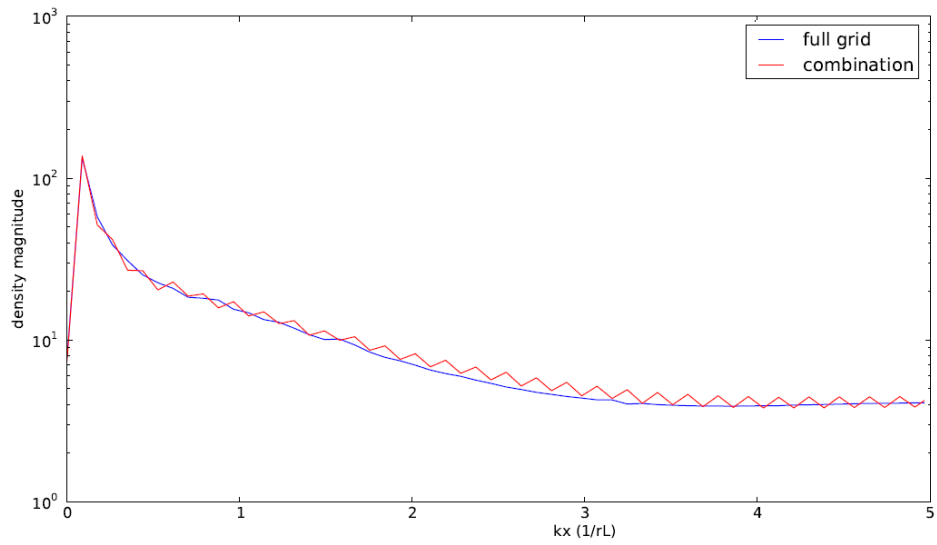
(c)
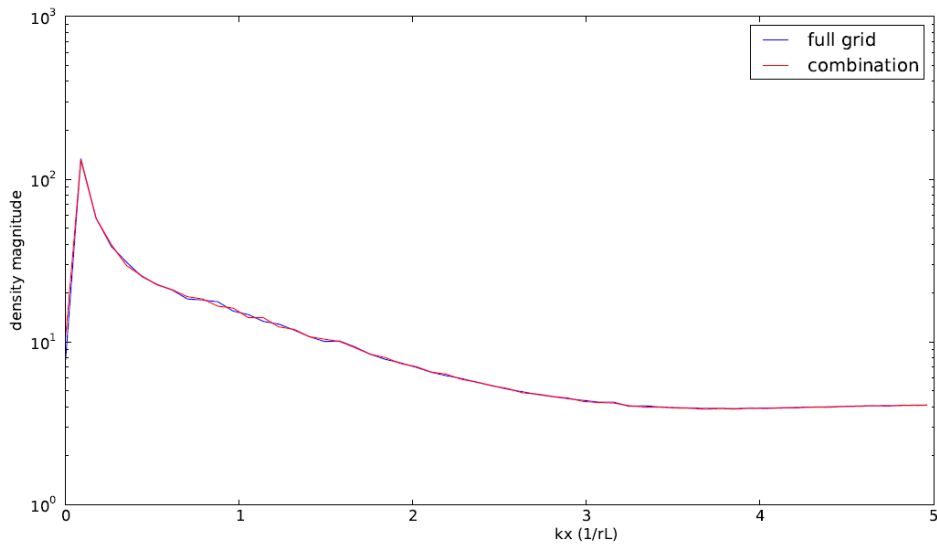
(d)

Figure 6.6: The results from coupling two Hasegawa-Wakatani simulations in slab geometry. All figures are a snapshot in time after turbulent saturation ($t=2048\omega_{ci}$). (a) shows the density contours when the overlap data were shared every $1024\omega_{ci}$. (b) shows the density contours when the overlap data were communicated every $32\omega_{ci}$. (c) is the radial (perpendicular to the coupling interface) Fourier spectrum of the data in (a), and (d) is the radial Fourier spectrum for (b).

results or the same accuracy with less boundary sharing required. Since the system is normalised to the ion larmor radius, ρ_i, the overlap amount is also measured in this quantity. For this coupled simulation, the grid points overlap exactly in real space, so interpolation is not required, though the handshake scheme is.

Figure 6.6 shows results for two different sharing frequencies both with the same amount of overlap ($25\rho_i$). A clear discontinuity can be seen at the centre of the domain in figure 6.6a because the overlapping data have been shared too infrequently. The effects of this infrequency are seen in the radial spectrum (figure 6.6b) in the jagged, alternating mode structure in the tail. The spectrum shows the reference simulation results, as well, which does not demonstrate this sawtooth behaviour.

The effect of sharing more frequently is immediately obvious when looking at figures 6.6c and 6.6d as they do not show the discontinuity or rough features seen in the previous case. One can conclude, then, that more frequent communication does indeed increase the accuracy of the simulation, as expected. How frequent this communication must be, however, requires a more detailed study of the results.

Figure 6.7 shows the result of scanning $\tau_i \in \left[2\omega_{ci}^{-1}, 1024\omega_{ci}^{-1}\right]$ for three values of overlap width: $12.5\rho_i$, $25\rho_i$, and $37.5\rho_i$. The RMSE depicted in these plots is the root mean square error of the density spatial spectra of the coupled simulation as compared to the reference full simulation. The clear trend is that more overlap and more frequent sharing both increase accuracy, as expected since both of these in their extreme limits are equivalent to a single full simulation. It is of note that the error appears to asymptote to a minimum value, likely limited by the chaotic nature of the turbulence. A similar asymptotic behaviour is noticed in the overlap size since the distance between the error is decreasing as overlap increases. Lastly, the run time significantly increases once the time between shares falls below $100\omega_{ci}^{-1}$. This is specific to this model since there are only two variables to communicate - the interpolation time and communication time are a flat overhead per variable, so the run time will likely be higher for a coupled run containing the full physics.
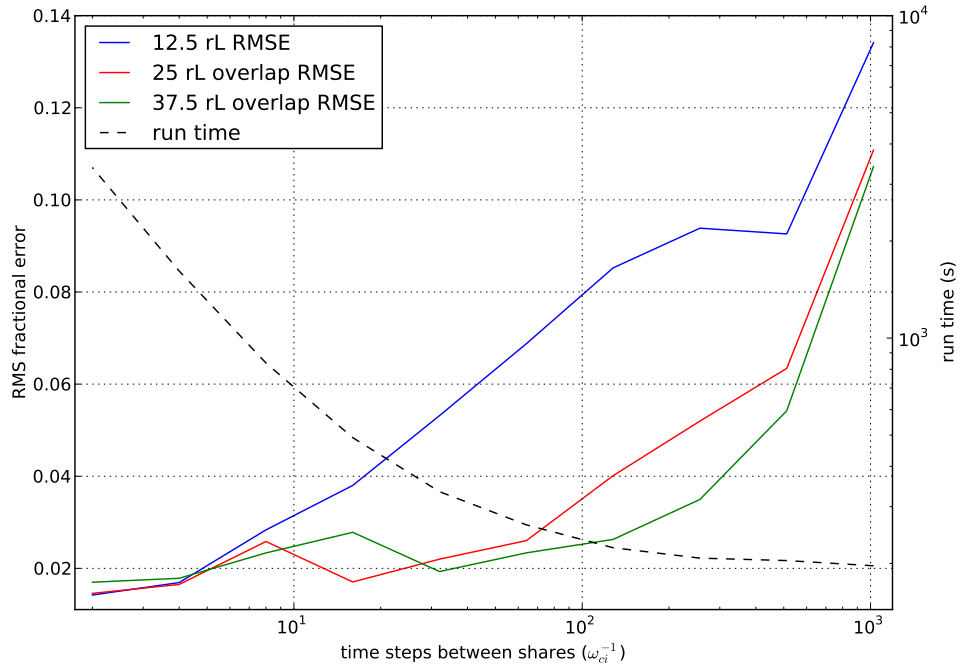
Figure 6.7: The error is depicted as a function of time between overlap data sharing, τ_i, for three different amounts of overlap. The run time (dotted black) is also shown to increase with frequency of communication and amount of overlap.

6.5.3 Toroidal Hasegawa-Wakatani

The HW system is also run in a toroidal geometry in which the coordinates are field aligned, as detailed in section 5.1.1. This 3-dimensional geometry now requires the interpolation to be less accurate (linear), and the grid points will likely no longer be aligned, so the interpolation will play a much larger role in the accuracy than it did in the slab geometry case. The same weighting given by equation 6.11 is used for the toroidal case. The torus used is a circular cross-section with minor radius $r_0 = 0.5$m and major radius $R_0 = 2$m. In an effort to approximate tokamak H-mode pedestal, there is a steep background density profile just inside the minor radius, as shown in figure 6.8, and the q-profile is linearly increasing across the domain.

In the final coupled code, the edge simulation will cover the range $\psi_N \in [0.9, 1.1]$ (normalised flux coordinate) and the core will cover $\psi_N \in [0, 0.95]$. To make this test as relevant as possible the overlap region is inside the minor radius (what would be the last closed flux surface).

The results, shown in figure 6.9, indicate that the coupling can produce very accu-
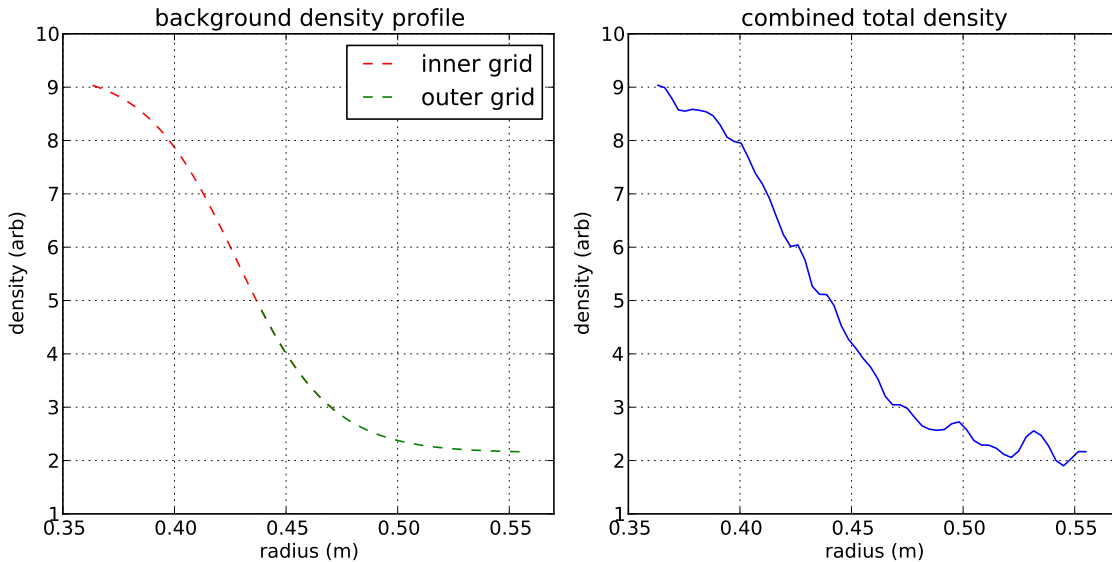
Figure 6.8: The background density profile (left) for the total and coupled grids is steep inside the minor radius (0.5m) to approximate the pedestal region. The density perturbations (right) lie on top of this background density profile.

rate results when compared to the full grid simulation. The spectra of the coupled simulations are within 0.1% (RMSE) of the full simulation - a fact that is reassuring because the interpolation scheme is less accurate for the toroidal case than it has been previously for the slab cases. It is apparent that the actual density perturbations are not identical between the two cases, a fact which is expected because the behaviour is very non-linear: even small differences in initial conditions will produce different final results. It is for this reason that the spectra are compared instead of the actual densities themselves. It is sufficient to say that if the reference spectrum is reproduced within error then the turbulent behaviour is accurately simulated.

A scan in τ_i reveals that the accuracy of these results is strongly dependent on the time between communication of the boundary. This behaviour, shown in figure 6.10, is very similar to the slab case. Again, the accuracy appears to flatten to a constant value at and below $100\omega_{ci}^{-1}$, indicating that there is no need to share more often than this for slab or toroidal geometry. Importantly, the grid points on the two grids do not line up exactly, but are shifted such that interpolation was required.
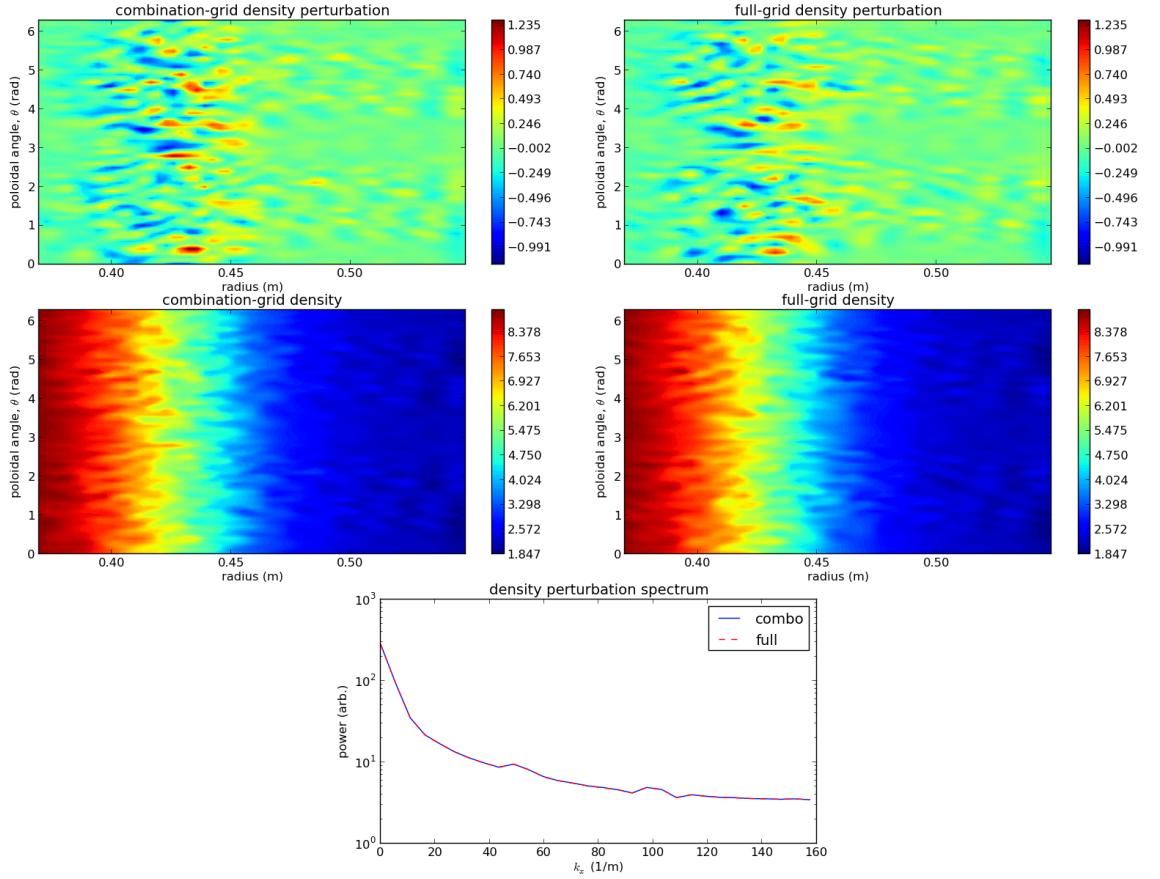
Figure 6.9: The coupled and full Hasegawa-Wakatani results are shown, both the perturbations and the total density. The radial spatial spectrum is shown to agree for both cases with an average error of 0.01% and a maximum error of 1.2%

6.6 CENTORI/BOUT++ benchmarking

In pairing BOUT++ and CENTORI there is a limit to the simplicity of the model that can be simulated. For testing purposes, initial tests were run in the simplest possible case - circular cross-section, toroidal device, with a very basic toroidal advection physics model in the edge and core. The complexity was then increased to include parallel flows and perpendicular diffusion. The physics model was then finally increased to its full complexity including electromagnetic effects. Lastly, the geometry is then extended to shaped and diverted plasmas to perform full, realistic simulations of the entire plasma. Each of these will be explored in the following sections.

The circular cross-section geometry is used in all but the final test, so it is important to describe it in some detail. The major radius $R_0 = 2$m and the minor radius $r_0 = 0.5$m, as before in the Hasegawa-Wakatani torus test case. However, though the edge simulation uses field-aligned coordinates, CENTORI in the core uses the stan-
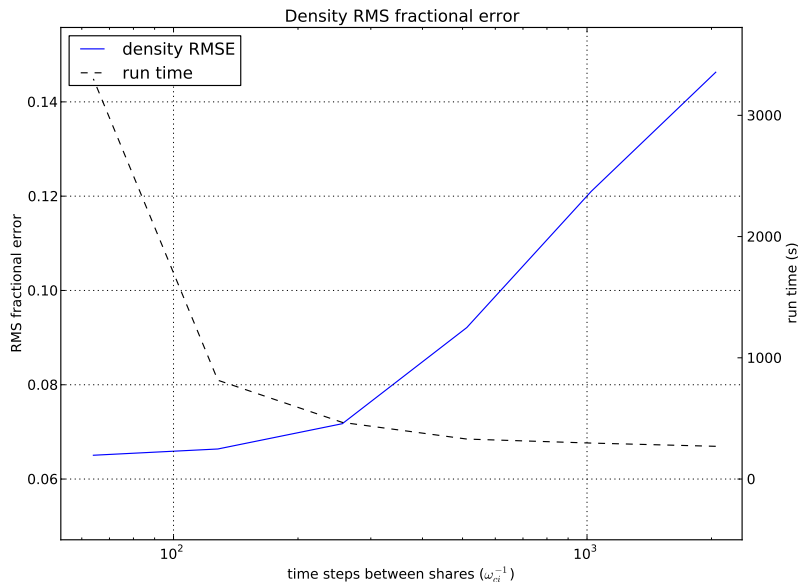
Figure 6.10: The root mean square error and the run-time as a function of time between communication of boundaries.

dard tokamak coordinates (r, θ, ϕ) to form its grid. Therefore, the combined grid is very irregular, as shown in figure 6.11.

6.6.1 Toroidal advection in simple geometry

A realistic aspect ratio, circular cross-section plasma is simulated using BOUT++ for the edge and CENTORI for the core. The physics simulated, however, is a very simple advection equation given by

$$\frac{\partial n}{\partial t} = v_\phi \cdot \nabla n \tag{6.14}$$

where v_ϕ is a constant toroidal velocity and n is the plasma density. An initial perturbation sinusoidal in toroidal angle is therefore expected to simply flow around the torus without any radial or poloidal motion. The velocity is constant across the entire torus, so as the blob flows there is a shear due to the circular path around the torus - the inner portion of the blob has a shorter distance to travel around the torus than that on the outer edge. This shearing can be seen in the results in figure 6.12.

The velocity, v_ϕ, is initialised to $0.1v_A$ - one-tenth of the Alfvén speed. The boundary data were communicated between edge and core every $5r_0/v_a$. In the total time
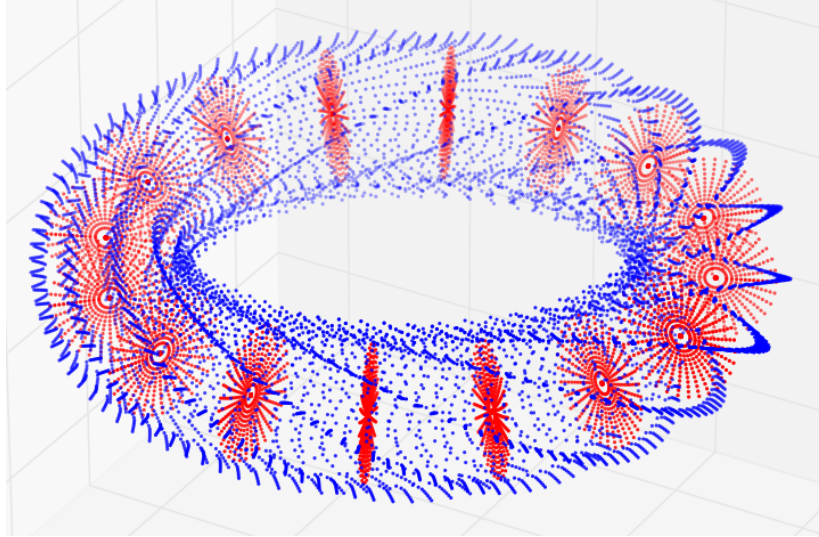
Figure 6.11: The BOUT++ edge simulation uses a field-aligned grid (blue) and the CEN-TORI core simulation uses a standard tokamak grid (red).

of the simulation, $75r_0/v_a$, the centre of the blob travelled slightly more than once around the torus. Qualitatively this result is exactly what was expected from this trivial experiment. Analytically, the path length of a blob on the inner edge of the torus is calculated to be 66% longer (for a torus with $R_0 = 4r_0$). When the inner edge of the blob has made one full revolution, as in figure 6.12c, the outer edge of the blob should be only 2/3 of the way around the torus. This result, though the physics is very simple, serves to confirm the functionality of the inner workings of TEACUP, which are intricate. The normalisations between the codes, geometries, coordinate systems, coupling mechanisms, and initialisations are all verified by the success of this example. It is with confidence, then, that the complexity of the physics model can be increased progressing into the next section.

6.7 Full TEACUP simulations

The final step in pairing the two codes was to increase the core physics to include the full set of equations in section 6.3 and the edge physics to the SimCat model described in section 5.5.2. However, the time scales in the edge are much faster than those in the core due to the open field lines making parallel transport more relevant, especially for thermal conduction. The edge, therefore, is much slower than the core simulations (by a factor of ~ 10x), so the physics in the edge is limited to only fluid flows, diffusion, conduction, and convection. The currents, both parallel and diamagnetic are disabled
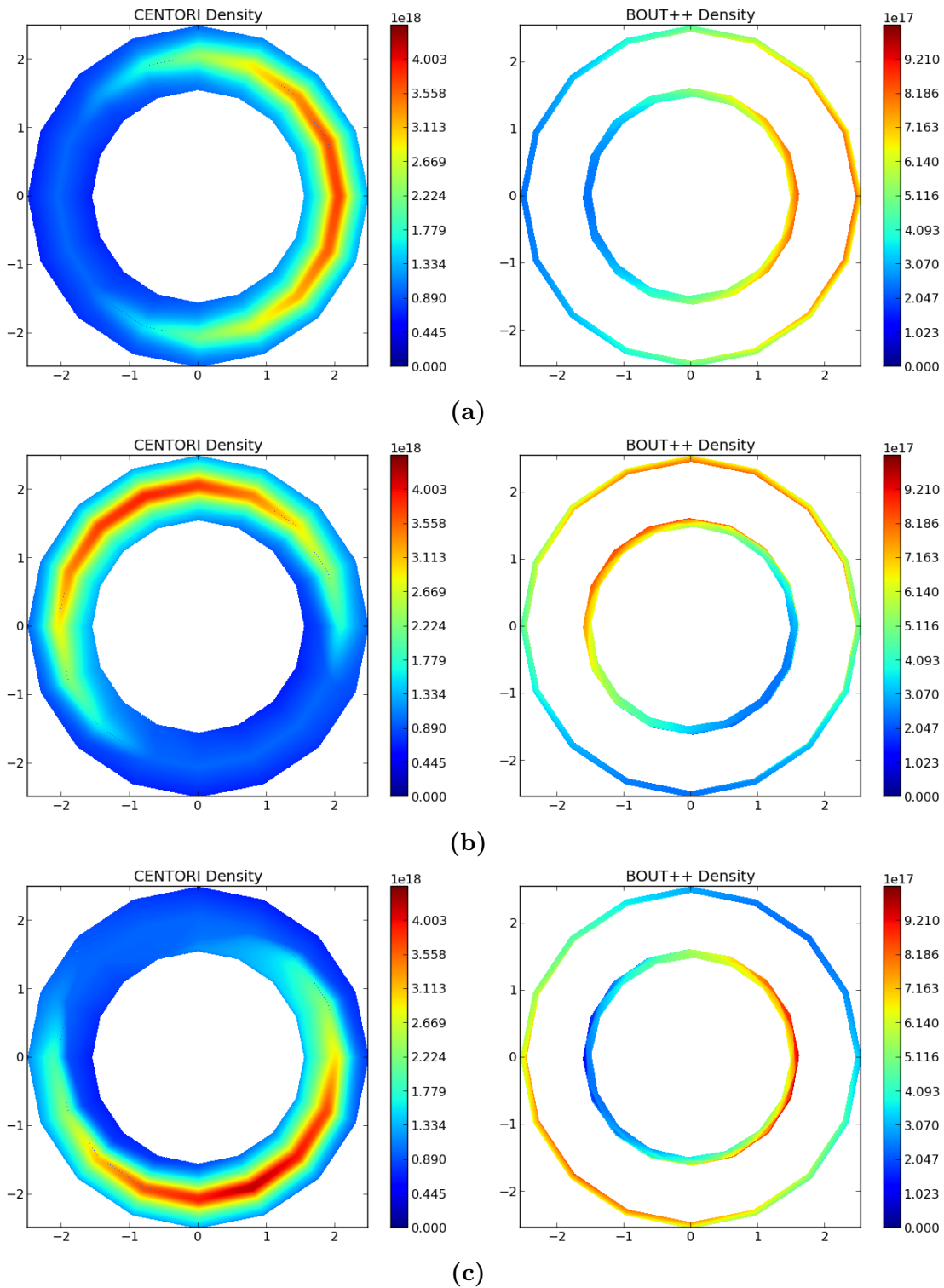
Figure 6.12: The results from coupling BOUT++ and CENTORI to perform simulations of a simple toroidal advection equation. The figures show a progression in time of a toroidally localised blob of density (top-down view of torus). (a) The blob is initialised at $\phi = 0$, which corresponds to the right-hand side of the figure. (b) As time progresses, the blob is advected counter-clockwise around the torus. (c) The difference in path lengths around the torus results in a visible shearing of the blob.

Figure 6.13: The core CENTORI (red) and edge BOUT++ (blue) grid points are shown in 3D (left) and projected onto a 2D poloidal cross-section (right).

since these are also very fast and limit the time step even further. In this way, the simulations are made to be as similar in run time as possible while including the physics essential for the basic study of profile evolution and turbulence form the core reaching the divertor.

6.7.1 Geometry

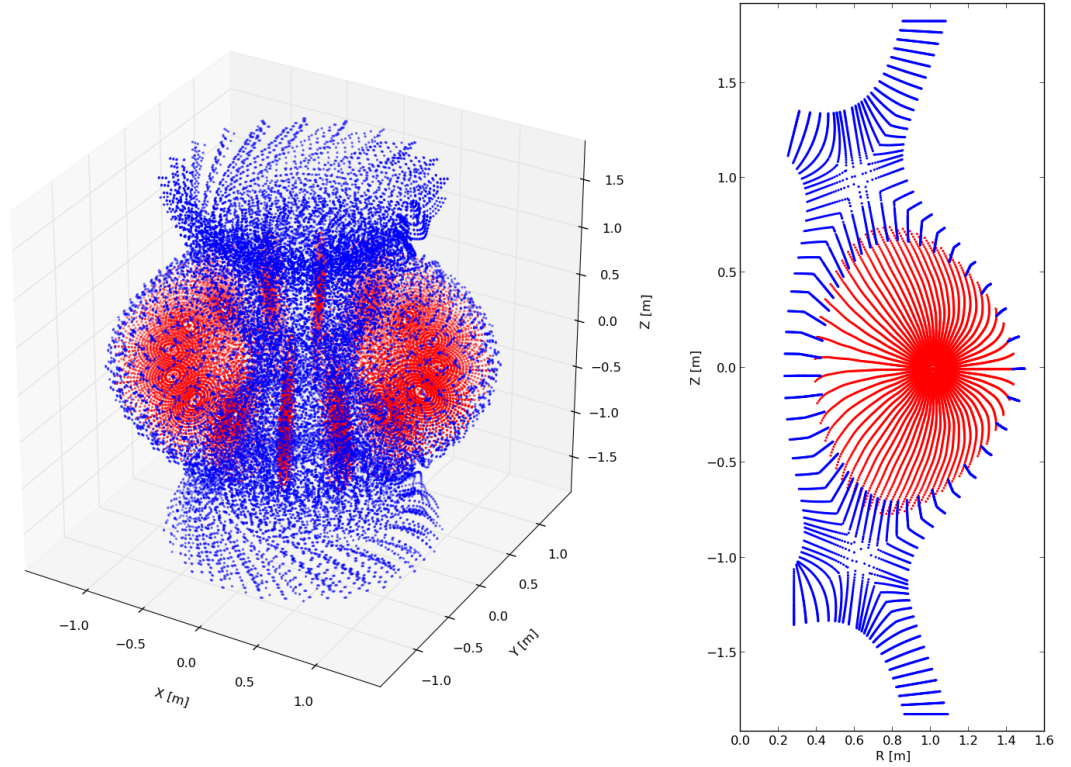A MAST geometry was chosen for simulation because the divertor legs are long and the geometry is easily changed (for simulation) since the vacuum vessel is large for divertor angle studies. Also, the plasma is very well diagnosed giving the potential opportunity for comparison with experiment. To use this geometry, the coil locations and currents are input into GRASS, the CENTORI Grad-Shafranov solver to calculate an equilibrium. This equilibrium is then used to generate core and edge grids, which are shown in figure 6.13. The overlap in this grid is $0.05\psi_N$, which varies in real length around the poloidal angle since the flux surfaces are shaped (ie. non-zero triangularity).

For the simulations on this grid, the simulation size is described by table 6.1. The distribution of the poloidal grid points for the BOUT++ edge grid is split among the
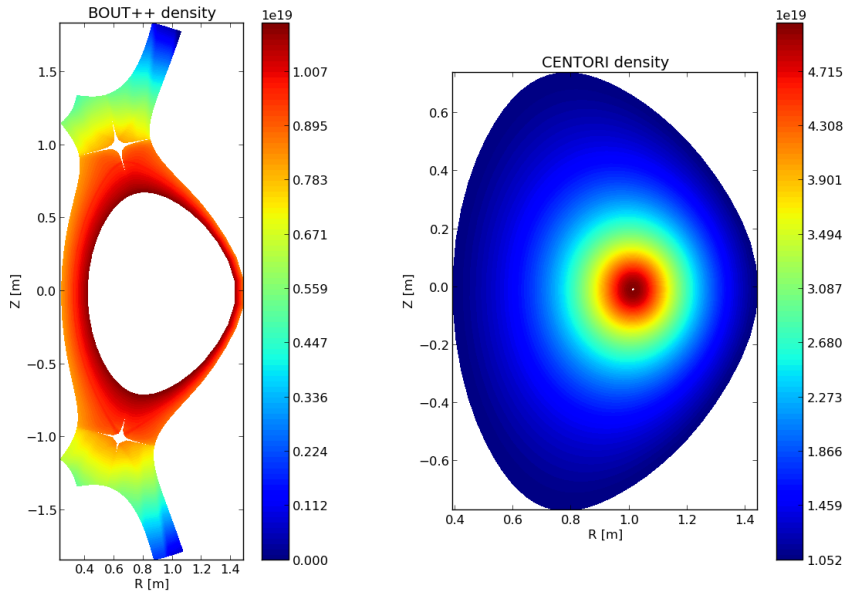
Figure 6.14: The initial conditions for BOUT++ and CENTORI density, temperature, and pressure are Gaussians with maxima on the magnetic axis. The velocity and potential are set to zero initially.

legs and outer core so that the grid spacing is relatively even throughout. This requires, from inner-lower leg around clockwise, 10-30-10-20-30-20 points, adding up to the total 120.

Table 6.1: The number of grid points for each dimension of the simulation are shown.

	N_ψ	$N_{\theta,y}$	$N_{\phi,z}$
BOUT++ edge	64	120	32
CENTORI core	128	64	32

6.7.2 Initial conditions

The initial conditions for the core are generated inside CENTORI to be Gaussians of density, temperature, and pressure with zero initial velocity and potential. These conditions are then interpolated and extrapolated to the edge grid to form the initial BOUT++ conditions. Figure 6.14 shows the initial conditions for the density for BOUT++ and CENTORI, and the pressure and temperature look the same, but with maxima of 10kPa and 1.25keV respectively.

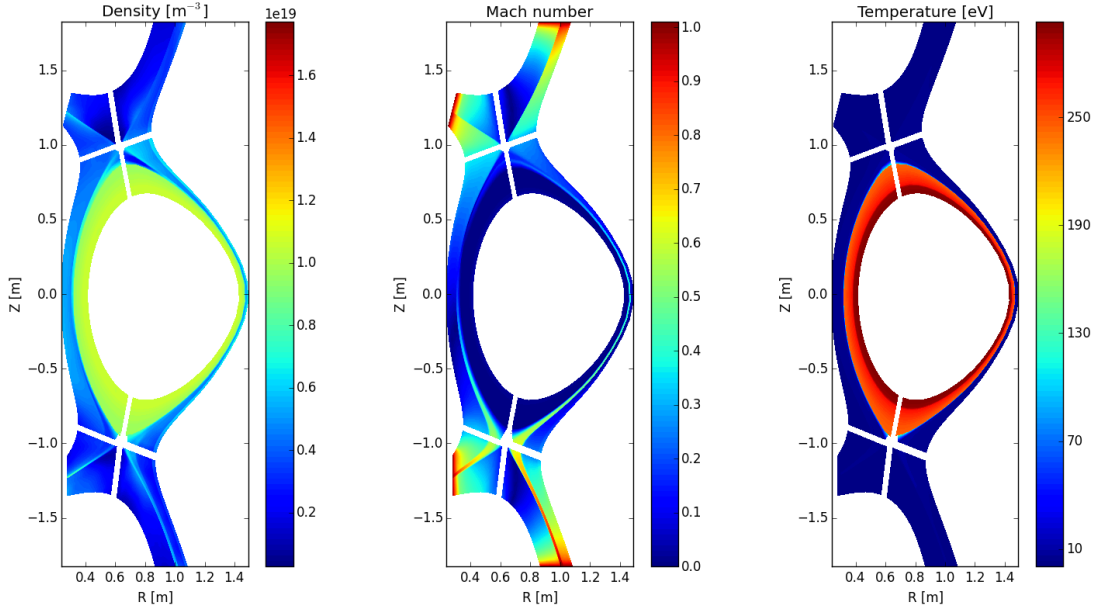**Figure 6.15:** Transport in the edge confines the plasma inside the separatrix for the density (left). The Mach number (middle) is seen to be 1 at the divertor plates, which is the proper Loizu boundary condition [128], and the flows are seen to decrease towards the core. The temperature (right) accentuates the high parallel transport due to thermal conduction as just inside the separatrix is very hot (200eV), and just outside the separatrix is very cold (15eV).

6.7.3 Communication and conservation

The system of equations being solved in the core and the edge are different, as detailed in sections 6.3 and 5.5.2. The information that must be shared between the codes is density, temperature, and parallel velocity; however, there are multiple ways to go about this. As described earlier, the handshake scheme conserves the shared quantities, so the ion flux and pressure were shared instead of the velocity and temperature, forcing these quantities to be conserved throughout the interpolation and weighting. With flux and pressure conserved, the energy is also conserved, which is a linear combination of these two quantities.

6.7.4 Results

The coupled simulation was run for $10^4\omega_{ci}^{-1}$. The final state of the edge fields is shown in figure 6.15, where the transport to the divertor is clearly shown in the scrape-off layer. Figure 6.16 shows the turbulent fluctuations in density, temperature, and velocity in the core.

The core evolves the full set of CENTORI electromagnetic 2-fluid equations, and tur-
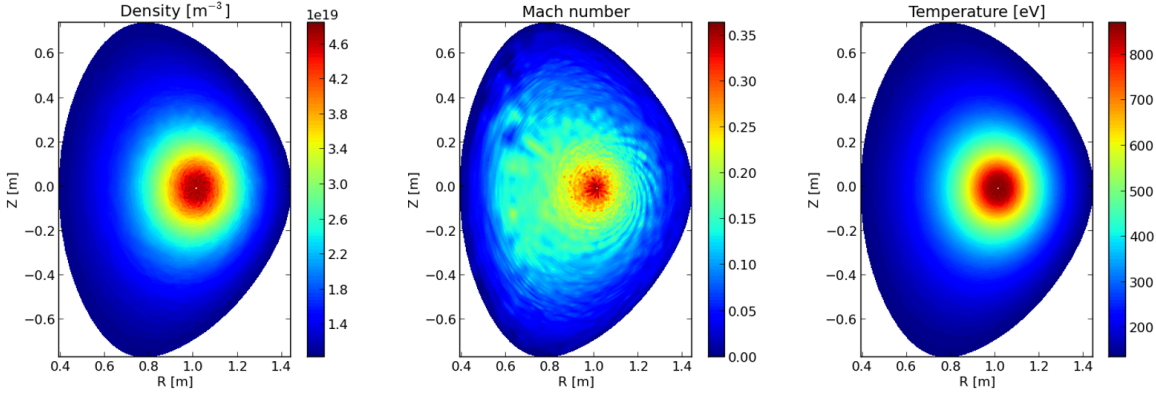
Figure 6.16: Turbulent fluctuations can be seen in the density (left), mach number (middle) and temperature (right) for the core simulations after $4000\omega_{ci}^{-1}$.

bulence is seen to develop. The edge contains only the transport equations, so no turbulence is generated self-consistently in the edge; however, figure 6.17 shows that turbulent density fluctuations are interpolated from the core to the edge, as expected. The edge grid is field-aligned, so the structures that appear poloidally elongated are actually along the field-line. These density fluctuations are calculated by subtracting the axisymmetric component of the density. A time trace of the density fluctuations shows the evolution of the plasma from the initial conditions to a nearly steady state, in figure 6.18. Each plot shows the evolution of three particular locations within the tokamak: the blue and green lines are both at the outboard mid-plane, with the blue just inside the separatrix and the green just outside. The red line shows the evolution just outside the separatrix at the divertor plate. The density and temperature are both very well confined, and the flows are very small inside the separatrix (blue). Outside the separatrix, the density is seen to decrease at the mid-plane as it streams down the field line towards the divertor plate where the density rises. The flows are non-zero at the outboard mid-plane outside the separatrix due to the lower double null MAST configuration, which favours the lower x-point. The flows reach Mach 1 by the time the plasma reaches the divertor plate. The temperature outside the separatrix decreases rapidly due to parallel thermal conduction, but there is still a higher temperature at the mid-plane than at the divertor plate, as is predicted by the two-point model.
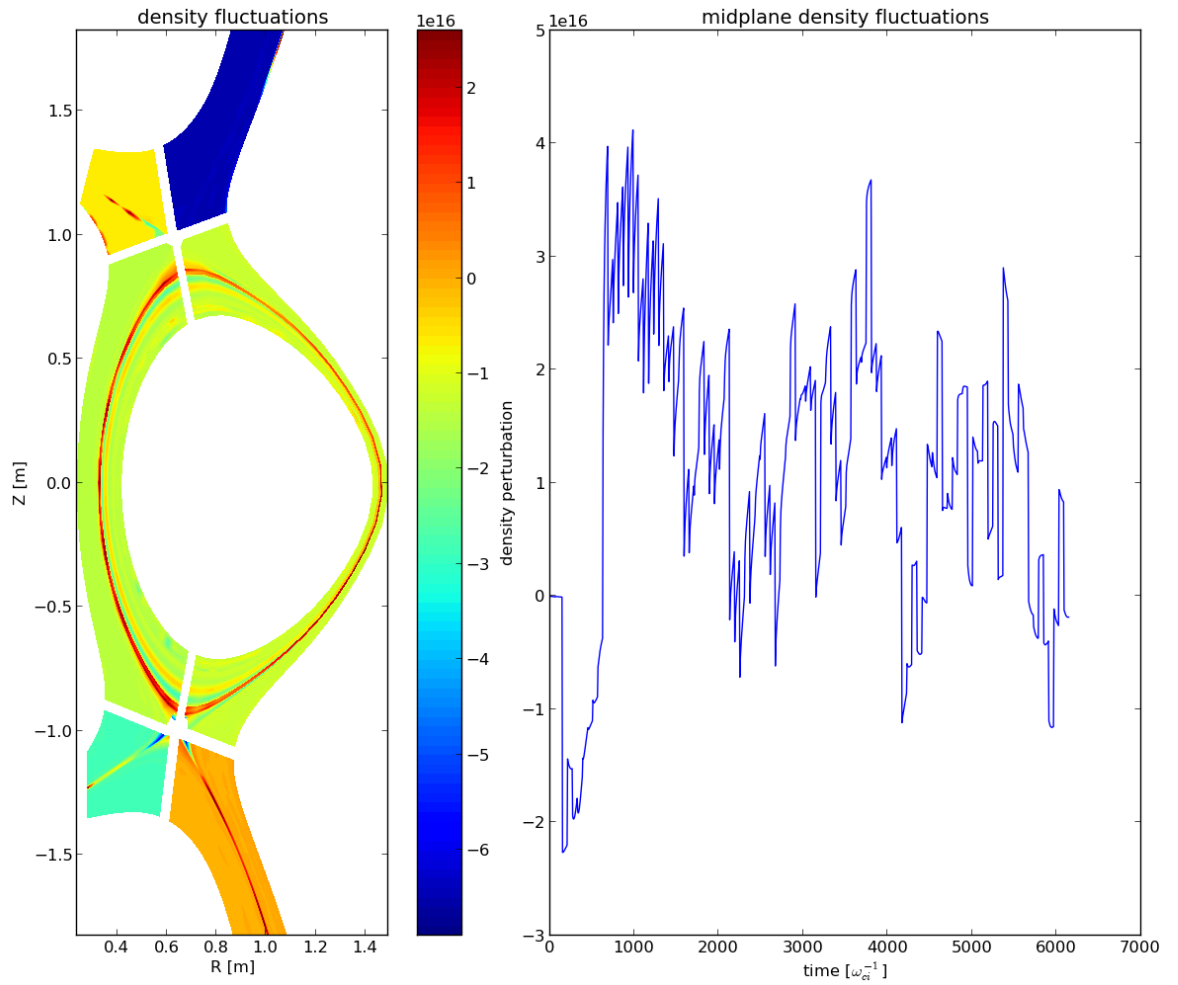
Figure 6.17: The tokamak edge contains fluctuations elongated along the field lines (left). A time trace of the density at a point just inside the separatrix at the outboard mid-plane shows these fluctuations in more detail.
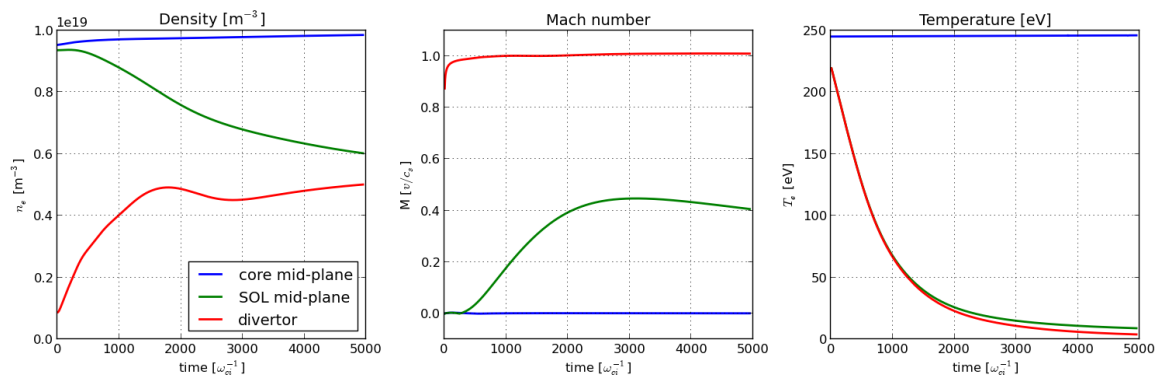

Figure 6.18: Each of the plots has three lines which correspond to a different location within the tokamak. .

6.8 Conclusion

In the effort to develop an integrated core and edge code, many tests and trials were performed to optimise the process of communicating between the two simulations. To pair the codes, the boundary information has to be shared and interpolated at regular intervals. The methods for this sharing, interpolation, and grid initialisation were explored explicitly throughout this chapter. First, the BOUT++ code was paired with itself in two overlapping domains to determine the optimal amount of overlap and time between sharing of boundary information. A slab diffusion and Hasegawa-Wakatani test gave insight into these areas demonstrating that 10-20 ρ_i is a reasonable amount of overlap and that the boundaries should be shared on the order of once every $100\omega_{ci}^{-1}$. The complexity of the system was then increased to toroidal geometry in which the grid points no longer lay in the exact same place in real space, allowing 3D interpolation methods to be tested for accuracy, which showed error less than 1% from the reference case. Finally, after testing the methods exhaustively, BOUT++ was paired with CENTORI, in toroidal and field-aligned (core and edge, respectively) geometries, and a simple physics model was run to demonstrate that the full coupled infrastructure was functioning as intended. Lastly, the physics models were increased to full complexity and a proof-of-concept simulation was run in full MAST geometry that shows correct qualitative behaviour in core and edge.

Chapter 7

Summary and Future Work

7.1 Summary

A novel, three-dimensional two-fluid turbulence simulation suite has been developed to address the upcoming challenges of ITER scenario development and plasma performance prediction. In the process of this development, multiple physics and computational studies were undertaken and completed.

Firstly, an analytic investigation of the validity of drift-reduced plasma fluid models found that only some regions of parameter space are properly described by these models. Most of the disagreement lies outside of tokamak relevant regimes or outside of the applicability of fluid models. This analysis was applied to Thomson scattering data from the JET tokamak and subtleties emerged. In general both drift-reduced and full velocity models are acceptable for modelling the edge plasma, while gyrofluid or gyrokinetic models are more accurate in the core.

Edge fluid simulations are more computationally intensive than core due to the complex geometry and high collisionality. Drift-reduced fluid models aid in the speed of such simulations, but more can be done to increase the speed, but at the cost of some accuracy, using large eddy dissipation models. Instead of resolving the full turbulent cascade from Kolmogorov micro-scale to the injection scale, these LES models approximate the dissipation that occurs at small scales without the need to actually resolve them in the simulation. Therefore, the resolution requirements are relaxed, but the

qualitative and quantitative features of the turbulence can be reproduced to a certain degree of accuracy depending on the LES model and resolution used. Four LES dissipation models were tested for their accuracy in reproducing the turbulent characteristics of a reference, high resolution case, all simulated with the BOUT++ framework. The four models (viscosity, hyperviscosity, Smagorinsky, and CENTORI) performed fairly equally overall, but with different specific system features reproduced better for each model. Importantly, all the LES models help to recover accuracy lost from low resolution.

When simulating the edge plasma, efficiency can also be gained by adopting a field-aligned coordinate system since the perturbations in the parallel direction have long wavelengths reducing the required resolution. However, the standard field-aligned systems have drawbacks which mean the x-point is not well resolved and the divertor geometry cannot be matched by the simulation grid. A novel coordinate system is introduced that enables any smooth geometry to be matched in the poloidal plane, which solves both of these issues. To implement the new system in BOUT++, the metric tensors and new boundary conditions were derived, and the whole system was verified using the method of manufactured solutions. Fluid simulations were then run in MAST geometry to investigate how the heat loads on the divertor had changed with the introduction of a more resolved x-point and divertor, showing that the old system had been over-estimating the heat flux to the divertor plate. Finally, simulations on an isolated divertor leg were run with fluid neutrals to explore the onset of detachment as upstream density was changed.

With the edge model and geometry optimised, the core and edge were ready to be coupled. The method for pairing the two codes required investigation, which was carried out by pairing BOUT++ with itself making use of its flexibility. The required domain overlap and frequency of communication between the codes was investigated to determine the ideal value for each parameter. Complexity in the simulations was incrementally increased, culminating in the full tokamak geometry for MAST with 3D electromagnetic turbulence in the core and 3D transport in the edge. The results of this coupled simulation are promising and demonstrate the stability of TEACUP to be

used for physics studies in the future.

7.2 Future work

The work from each chapter (3-6) could be extended, so each is addressed in turn. Chapter 3 discusses the validity of drift-reduced fluid models for use in tokamak simulations. This work could be continued in regards to fluid models to look at how finite compressibility affects the linear growth rates. Finally, the linear behaviour describes the early evolution and stability of the turbulence, but later in the non-linear phase this can become irrelevant. Simulations of full velocity and drift-reduced models could be carried out to compare the spectra and time-dependent features of the resulting turbulence.

The large eddy simulation work in chapter 4 could be extended to include more complex models, like those mentioned in section 4.3.2, that attempt to predict the dissipation constant empirically. Probably the most important work that could be conducted in the LES domain for plasma turbulence is the development of a new model that reproduces both the standard and the inverse energy cascades so that zonal flows can self-consistently develop. This is a feature that turbulence simulations may need to include for H-mode to spontaneously evolve without forcing lower transport in the edge, etc. as done in JINTRAC [72].

Detachment and divertor simulations remain a large focus for the progression of simulation towards predictive modelling for ITER and other future devices. The work in chapter 5 can be extended and continued to fully develop three-dimensional plasma simulations with turbulence and neutrals. Since the plasma interaction with neutrals and plasma turbulence are the two dominate mechanisms for heat spreading in the divertor, this could lead to predictive models of heat flux profiles on the divertor plates. In addition to this, the fluid neutral model could be extended to include more impurity species and atomic processes to truly model experimentally relevant conditions since tungsten, beryllium, and nitrogen (seeded) are often found in the divertor plasma.

The extensions of the final chapter on edge and core integrated modelling are many, and mostly include applications of such a simulation to explore tokamak physics such as the L-H transition, core/edge turbulence propagation, GAM/zonal flow development, the effects of detachment on core profiles, and more. These are all important questions in plasma physics that need to be understood better for the development of operational scenarios for ITER that will not lead to unacceptable disruption. In addition to these physics concerns, the development of the code could also be improved. Firstly, the communication should be made more amenable for supercomputer use with communication via memory instead of hard disk. Also, migration from IDL to python would make the code more universally usable, but this requires Hypnotoad (the BOUT++ grid generator) to be rewritten in python. The code could also be improved through the inclusion of more physics, for example neutrals in the edge (fluid via BOUT++ or kinetic with EIRENE [70]), impurities in the core, pedestal stability calculations (via ELITE [134, 135]), and neutral beam and radio frequency heating and current drive. Predictive modelling is necessary for future fusion devices like ITER because they will be too expensive and the plasma too energetic to experimentally "try new things" without first having simulated them rigorously and developed are large amount of confidence that the machine will not be destroyed. Improvements and developments toward full tokamak integrated modelling are vital as it will provide the foundation for this predictive modelling.

Bibliography

[1] J. Leddy, B. Dudson, M. Romanelli, and JET Contributors. On the validity of drift-reduced fluid models for tokamak plasma simulation. *Plasma Physics and Controlled Fusion*, 57(12):125016, 2015.

[2] Fusion for Energy. Annual Report 2011, 2011.

[3] David MacKay. *Sustainable Energy - without the hot air*. UIT Cambridge, 2008.

[4] International Energy Agency. Key World Energy Statistics, 2012.

[5] British Petroleum. BP Statistical Review of World Energy June 2015. (June):48, 2015.

[6] United Nations. World Population To 2300. *New York*, 18:553–561, 2004.

[7] A Einstein. Does the inertia of a body depend upon its energy-content? (Ist die Trägheit eines Körpers von seinem Energieinhalt abhängig?). *Annalen der Physik*, pages 1–3, 1905.

[8] Lorenzo Torrisi. Ion Acceleration and D-D Nuclear Fusion in Laser-Generated Plasma from Advanced Deuterated Polyethylene. *Molecules*, 19:17052–17065, 2014.

[9] A A Harms, D R Kingdon, K F Schoepf, and G K Miley. *Principles of fusion energy: an introduction to fusion energy for students of science and engineering.* World Scientific, Singapore, 2000.

[10] Y. Horibe and N. Ogura. Deuterium content as a parameter of water mass in the ocean. *Journal of Geophysical Research*, 73(4):1239–1249, 1968.

[11] Y. Wu and the FDS Team. Conceptual design and testing strategy of a dual functional lithium-lead test blanket module in iter and east. *Nuclear Fusion*, 47(11):1533, 2007.

[12] L. Giancarli, V. Chuyanov, M. Abdou, M. Akiba, B.G. Hong, R. Lässer, C. Pan, and Y. Strebkov. Breeding blanket modules testing in iter: An international program on the way to demo. *Fusion Engineering and Design*, 81(17):393 – 405, 2006.

[13] J. Meyer-ter Vehn. Fast ignition of icf targets: an overview. *Plasma Physics and Controlled Fusion*, 43(12A):A113, 2001.

[14] E.I. Moses, R.E. Bonanno, C.A. Haynam, R.L. Kauffman, B.J. MacGowan, R.W. Patterson Jr., R.H. Sawicki, and B.M. Van Wonterghem. The national ignition facility: Path to ignition in the laboratory. *J. Phys. IV France*, 133:57, 2006.

[15] O. Hurricane, D. Callahan, . Casey, P. Celliers, C. Cerjan, E. Dewald, . Dittrich, T. Döppner, D. Hinkel, B. Hopkins, J. Kline, S. Le Pape, T. Ma, A. MacPhee, J. Milovich, A. Pak, H. Park, P. Patel, B. Remington, J. Salmonson, P. Springer, and R. Tommasini. Fuel gain exceeding unity in an inertially confined fusion implosion. *Nature*, 506:343–8, 2014.

[16] R.W. Moir. *Standard mirror fusion reactor design study.* Jan 1978.

[17] B. Dudson. Magnetic confinement fusion lectures. University of York, 2011.

[18] F. Chen. *Introduction to Plasma Physics and Controlled Fusion*, volume 1. 2nd edition, 1974.

[19] K. Ikeda, C. Gormezano, A.C.C. Sips, T.C. Luce, S. Ide, A. Becoulet, X. Litaudon, A. Isayama, J. Hobirk, M.R. Wade, T. Oikawa, R. Prater, A. Zvonkov, B. Lloyd, T. Suzuki, E. Barbato, P. Bonoli, C.K. Phillips, V. Vdovin, E. Joffrin, T. Casper, J. Ferron, D. Mazon, D. Moreau, R. Bundy, C. Kessel, A. Fukuyama, N. Hayashi, F. Imbeaux, M. Murakami, A.R. Polevoi, and H.E. St John. Progress in the iter physics basis - chapter 6: steady state operation. *Nuclear Fusion*, 47(6), 2007.

[20] Max-Plank-Institut füi Plasmaphysik IPP. Tokamak. http://www.ipp.mpg.de/14869/tokamak, 2015.

[21] Y. Klimontovich. The statistical theory of non-equilibrium processes in a plasma. Pergamon, London, 1967.

[22] A. Vlasov. Many-particle theory and its application to plasma. translated from the russian. gordon and breach science publishers. *Inc., New York*, 1961.

[23] J. Wesson and D. Campbell. *Tokamaks.* International Series of Monographs on Physics. OUP Oxford, 2011.

[24] S. Braginskii. Transport Processes in a Plasma. *Reviews of Plasma Physics*, 1:205–311, 1965.

[25] R. Fitzpatrick. *The Physics of Plasmas.* Lulu, 2008.

[26] H. Grad. On the kinetic theory of rarefied gases. *Communications on Pure and Applied Mathematics*, 2:331–407, 1949.

[27] L. D. Landau and L.P. Pitaevskii. *Course of theoretical physics - Physical Kinetics*, volume 10. Butterworth Heinemann, 1997.

[28] A. Mikhailovskii and V. Tsypin. Transport equations and gradient instabilities in a high pressure collisional plasma. *Plasma Physics*, 13(9), 1971.

[29] R. Courant, K. Friedrichs, and H. Lewy. On the Partial Difference Equations of Mathematical Physics. *IBM Journal of Research and Development*, 11(2):215–234, 1967.

[30] P.J. Knight, A. Thyagaraja, T.D. Edwards, J. Hein, M. Romanelli, and K.G. McClements. CENTORI: A global toroidal electromagnetic two-fluid plasma turbulence code. *Computer Physics Communications*, 183(11):2346–2363, November 2012.

[31] R. Goldston and P. Rutherford. *Introduction to plasma physics.* Institute of Physics Publishing, Bristol and Philadelphia, 1995.

[32] R. Hazeltine and J. Meiss. *Plasma confinement.* Addison-Wesley, Redwood City, 1992.

[33] P. Liewer. Measurements of microturbulence in tokamaks and comparisons with theories of turbulence and anomalous transport. *Nuclear Fusion*, 25:543–621, 2011.

[34] J. F. Drake, N. T. Gladd, C. S. Liu, and C. L. Chang. Microtearing modes and anomalous transport in tokamaks. *Physical Review Letters*, 44(15):994–997, 1980.

[35] A. J. Wootton, B. A. Carreras, H. Matsumoto, K. McGuire, W. A. Peebles, Ch. P. Ritz, P. W. Terry, and S. J. Zweben. Fluctuations and anomalous transport in tokamaks. *Physics of Fluids B: Plasma Physics*, 2(1990):2879, 1990.

[36] B. Carreras. Progress in anomalous transport research in toroidal magnetic confinement devices. *IEEE Transactions on Plasma Science*, 25(6):1281–1321, 1997.

[37] J. Conner and H. Wilson. Survey of theories of anomalous transport. *Plasma Physics and Controlled Fusion*, 36:719–795, 1999.

[38] A. M. Dimits, T. J. Williams, J. A. Byers, and B. I. Cohen. Scalings of ion-temperature-gradient-driven anomalous transport in tokamaks. *Physical Review Letters*, 77:71, 1996.

[39] T. Stoltzfus-dueck. *Tokamak Edge Turbulence and the Approach to Adiabatic Response.* PhD thesis, 2009.

[40] R. Kraichnan. Eddy viscosity in two and three dimensions. *Journal of the Atmospheric Sciences*, 33:1521–1536, 1976.

[41] J. Hunt and D. Williams. Turbulence and stochastic processes: Kolmogorov's ideas 50 years on. *Journal of Fluid Mechanics*, 275, 1994.

[42] S. Camargo, D. Biskamp, and B. Scott. Resistive drift-wave turbulence 85748. *Physics of Plasmas*, 2(1):48–62, 1995.

[43] P. Diamond, S. Itoh, K. Itoh, and T. Hahm. Zonal flows in plasma - a review. *Plasma Physics and Controlled Fusion*, 47(5):R35–R161, May 2005.

[44] K. Itoh, S. Itoh, P. Diamond, T. Hahm, A. Fujisawa, G. Tynan, M. Yagi, and Y. Nagashima. Physics of zonal flows. *Physics of Plasmas*, 13(5):055502, 2006.

[45] P. Diamond, A. Hasegawa, and K. Mima. Vorticity dynamics, drift wave turbulence, and zonal flows: a look back and a look ahead. *Plasma Physics and Controlled Fusion*, 53(12):124001, December 2011.

[46] J. Connor and H. Wilson. A review of theories of the L-H transition. *Plasma Physics and Controlled Fusion*, (42), 2000.

[47] I. Shesterikov, Y. Xu, C. Hidalgo, M. Berte, P. Dumortier, M. Van Schoor, M. Vergote, and G. Van Oost. Direct evidence of eddy breaking and tilting by edge sheared flows observed in the TEXTOR tokamak. *Nuclear Fusion*, 52(4):042004, April 2012.

[48] F Ryter, M Cavedon, RM McDermott, T Pütterich, M Willensdorfer, R Fischer, B Kurzan, G Tardini, E Viezzer, ASDEX Upgrade Team, et al. Key role of edge ion heat flux and neoclassical radial electric field in the lh transition physics. In *42nd EPS Conference on Plasma Physics*, 2015.

[49] GR Tynan, I Cziegler, PH Diamond, M Malkov, A Hubbard, JW Hughes, JL Terry, and JH Irby. Recent progress towards a physics-based understanding of the h-mode transition. *Plasma Physics and Controlled Fusion*, 58(4):044003, 2016.

[50] ITER Confinement Database and Modelling Group. Fusion energy (proc. 16th int. conf. montreal, 1996). Vienna: IAEA, 1997.

[51] J Hugill. Edge turbulence in tokamaks and the L-mode to H-mode transition. *Plasma Physics and Controlled Fusion*, (42), 2000.

[52] S. Lisgo, L. Giancarli, R. Pitts, S. Putvinski, and J. Snipes. ITER Status and Challenges. (March):1–57, 2012.

[53] G. Piazza, G.F. Matthews, J. Pamela, H. Altmann, J.P. Coad, T. Hirai, A. Lioure, H. Maier, Ph. Mertens, V. Philipps, V. Riccardo, M. Rubel, and E. Villedieu. R&D on tungsten plasma facing components for the JET ITER-like wall project. *Journal of Nuclear Materials*, 367-370:1438–1443, August 2007.

[54] Eurofusion. The plasma edge - research for tomorrow's energy supply. https://www.euro-fusion.org/fusion/spot-on-jet-operations/maintaining-the-plasma/plasma-edge/, 2015.

[55] C. Pitcher and P. Stangeby. Experimental divertor physics. *Plasma Physics and Controlled Fusion*, 39:779–930, 1999.

[56] L. Spitzer and R. Härm. Transport phenomena in a completely ionized gas. *Physical Review Letters*, 89:977–980, 1953.

[57] P. Stangeby. *The plasma boundary of magnetic fusion devices*. Institute of Physics Pub., 1 edition, 2000.

[58] A. Loarte, R. Monk, J. Martín-Solís, D. Campbell, A. Chankin, S. Clement, S. Davies, J. Ehrenberg, S. Erents, H. Guo, P. Harbour, L. Horton, L. Ingesson, H. Jäckel, J. Lingertat, C. Lowry, C. Maggi, G. Matthews, K. McCormick, D. O'Brien, R. Reichle, G. Saibene, R. Smith, M. Stamp, D. Stork, and G. Vlases. Plasma detachment in JET Mark I divertor experiments. *Nuclear Fusion*, 38(3):331–371, 2002.

[59] J. Harrison. *Characterisation of detached plasmas on the MAST tokamak*. PhD thesis, University of York, 2010.

[60] D. Clery. ITER's 12 Billion Gamble. *Science*, 314(5797):238–242, 2006.

[61] D. Maisonnier, I. Cook, S. Pierre, B. Lorenzo, D. Luigi, Giancarli Luciano, N. Prachai, P. Aldo, and the PPCS Team. Demo and fusion power plant conceptual studies in europe. *Fusion Engineering and Design*, 81(8), 2006.

[62] Eurofusion. Comparison of jet and iter. https://www.euro-fusion.org/2014/01/comparison-of-jet-and-iter/, 2015.

[63] T. Eich, A.W. Leonard, R.A. Pitts, W. Fundamenski, R.J. Goldston, T.K. Gray, A. Herrmann, A. Kirk, A. Kallenbach, O. Kardaun, A.S. Kukushkin, B. LaBombard, R. Maingi, M.A. Makowski, A. Scarabosio, B. Sieglin, J. Terry, A. Thornton, ASDEX Upgrade Team, and JET EFDA Contributors. Scaling of the tokamak near the scrape-off layer h-mode power width and implications for iter. *Nuclear Fusion*, 53(9):093031, 2013.

[64] R.J. Goldston. Heuristic drift-based model of the power scrape-off width in low-gas-puff h-mode tokamaks. *Nuclear Fusion*, 52(1):013009, 2012.

[65] ITER. International Tokamak Physics Activity (ITPA). *http://www.iter.org/org/team/fst/itpa*, 2013.

[66] Martin Greenwald. Density limits in toroidal plasmas. *Plasma Physics and Controlled Fusion*, 44(8):R27, 2002.

[67] R. Simonini, G. Corrigan, G. Radford, J. Spence, and A. Taroni. Models and numerics in the multi-fluid 2-d edge plasma code edge2d/u. *Contributions to Plasma Physics*, 34(2-3):368–373, 1994.

[68] B.D. Dudson, M.V. Umansky, X.Q. Xu, P.B. Snyder, and H.R. Wilson. BOUT++: A framework for parallel plasma fluid simulations. *Computer Physics Communications*, 180(9):1467–1480, September 2009.

[69] J. Candy and R.E. Waltz. An Eulerian gyrokinetic-Maxwell solver. *Journal of Computational Physics*, 186(2):545–581, 2003.

[70] D. Reiter, M. Baelmans, and P. Börner. The eirene and b2-eirene codes. *Fusion Science and Technology*, 47(2):172–186, 2005.

[71] Eurofusion. The integrated tokamak modelling task force. http://portal.efda-itm.eu/itm/portal/, 2015.

[72] M Romanelli, G Corrigan, V Parail, S Wiesen, R Ambrosino, P da Silva Aresta Belo, L Garzotti, D Harting, F Köchl, T Koskela, et al. Jintrac: a system of codes for integrated simulation of tokamak scenarios. *Plasma Fusion Res*, 9:34030231–4, 2014.

[73] G. Cenacchi and A. Taroni. Jetto: A free-boundary plasma transport code. *JET-IR (88)*, 3, 1988.

[74] B. Braams. Radiative divertor modelling for ITER and TPX. *Contributions to Plasma Physics*, 36:276–281, 1996.

[75] D. Coster, X. Bonnin, and M. Warrier. Extensions to the SOLPS edge plasma simulation code to include additional surface interaction posibilities. *Physica Scripta*, T124:9–12, 2006.

[76] D. Coster. Detachment physics in SOLPS simulations. *Journal of Nuclear Materials*, 415(1):S545–S548, 2011.

[77] H.Y. Guo, S. Zhu, and J. Li. B2/Eirene modeling of EAST divertor target power loading with enhanced wall carbon source and additional neon injection. *Journal of Nuclear Materials*, 363-365:162–166, 2007.

[78] A. Chankin, D. Coster, R. Dux, C. Fuchs, G. Haas, A. Herrmann, L. Horton, A. Kallenbach, M. Kaufmann, C. Konz, K. Lackner, C. Maggi, H. Muller, J. Neuhauser, R. Pugno, M. Reich, and W. Schneider. SOLPS modelling of AS-DEX upgrade H-mode plasma. *Plasma Physics and Controlled Fusion*, 48:839–868, 2006.

[79] A. Chankin, D. Coster, R. Dux, C. Fuchs, G. Haas, A. Herrmann, L. Horton, A. Kallenbach, B. Kurzan, H. Müller, R. Pugno, M. Wischmeier, and E. Wolfrum. Simulation of ASDEX Upgrade Ohmic plasmas for SOLPS code validation. *Nuclear Fusion*, 49:015004, 2008.

[80] A. S. Kukushkin, H. D. Pacher, V. Kotov, G. W. Pacher, and D. Reiter. Finalizing the ITER divertor design: The key role of SOLPS modeling. *Fusion Engineering and Design*, 86(12):2865–2873, 2011.

[81] J. Cary, A. Hakim, M. Miah, S. Kruger, A. Pletzer, S. Shasharina, S. Vadlamani, R. Cohen, T. Epperly, T. Rognlien, A. Pankin, R. Groebner, S. Balay, L. McInnes, and H. Zhang. Facets - a framework for parallel coupling of fusion components. *2010 18th Euromicro Conference on Parallel, Distributed and Network-based Processing*, pages 435–442, 2010.

[82] X. Xue-qiao. The BOUT Project; Validation and Benchmark of BOUT Code and Experimental Diagnostic Tools for Fusion Boundary Turbulence. *Plasma Science and Technology*, 3:959–964, 2001.

[83] G. Byrne and A. Hindmarsh. Pvode, an ode solver for parallel computers. *Int. J. High Perform. Comput. Appl.*, 13(4):354–365, November 1999.

[84] B. Dudson, X. Xu, M. Umansky, H. Wilson, and P. Snyder. Simulation of edge localized modes using bout++. *Plasma Physics and Controlled Fusion*, 53(5):054005, 2011.

[85] P. Popovich, M. V. Umansky, T. A. Carter, and B. Friedman. Analysis of plasma instabilities and verification of the bout code for the large plasma device. *Physics of Plasmas*, 17(10), 2010.

[86] M. V. Umansky, P. Popovich, T. a. Carter, B. Friedman, and W. M. Nevins. Numerical simulation and analysis of plasma turbulence the Large Plasma Device. *Physics of Plasmas*, 18(2011):055709, 2011.

[87] E. M. Davis, M. Porkolab, P. Ennever, N. Tsujii, J. W. Hughes, and X. Q. Xu. Edge turbulence studies in alcator c-mod with phase contrast imaging and bout++. In *APS Meeting Abstracts*, page 9008P, 2011.

[88] B. Shanahan, B. Dudson, and P. Hill. Modelling of turbulence in x-point configurations with bout++. In *APS Meeting Abstracts*, page 3003, 2014.

[89] J. R. Angus, M. Umansky, and S. I. Krasheninnikov. 3D Blob Modelling with BOUT++. *Contributions to Plasma Physics*, 52(5-6):348–352, June 2012.

[90] N. Walkden, B. Dudson, and G. Fishpool. Characterization of 3D filament dynamics in a MAST SOL flux tube geometry. *Plasma Physics and Controlled Fusion*, 55:105005, 2013.

[91] L. Easy, F. Militello, J. Omotani, B. Dudson, E. Havlickova, P. Tamain, V. Naulin, and A. Nielsen. Three dimensional simulations of plasma filaments in the scrape off layer : A comparison with models of reduced dimensionality. *Physics of Plasmas*, 21:122515, 2014.

[92] X. Q. Xu, B. Dudson, P. B. Snyder, M. V. Umansky, and H. Wilson. Nonlinear Simulations of Peeling-Ballooning Modes with Anomalous Electron Viscosity and their Role in Edge Localized Mode Crashes. *Physical Review Letters*, 105(October):175005, 2010.

[93] T. Y. Xia and X. Q. Xu. Five-field simulations of peeling-ballooning modes using BOUT++ code. *Physics of Plasmas*, 20(2013):052102, 2013.

[94] T. Y. Xia and X. Q. Xu. Six-field two-fluid simulations of peeling-ballooning modes using BOUT++. *Nuclear Fusion*, 53(073009):052102, 2013.

[95] M. Kim, M.J. Choi, J. Lee, G.S. Yun, W. Lee, H.K. Park, C.W. Domier, N.C. Luhmann Jr, X.Q. Xu, and the KSTAR Team. Comparison of measured 2d elms with synthetic images from bout++ simulation in kstar. *Nuclear Fusion*, 54(9):093004, 2014.

[96] K. Salari and P. Knupp. Code Verification by the Method of Manufactured Solutions. *Sandia National Laboratories*, (Technical Report SAND2000-1444), 2000.

[97] A. Gray, M. Ashworth, J. Hein, F. Reid, and M. Weiland. A Performance Comparison of HPCx and HECToR. *HPCx Technical Report*, 2008.

[98] J. R. Robinson, B. Hnat, A. Thyagaraja, K. G. McClements, P. J. Knight, and A. Kirk. Global two-fluid simulations of geodesic acoustic modes in strongly shaped tight aspect ratio tokamak plasmas. *Physics of Plasmas*, 20(2013):052302, 2013.

[99] B. Scott. Computation of turbulence in magnetically confined plasmas. *Plasma Physics and Controlled Fusion*, 48:B277–B293, 2006.

[100] E. Frieman and L. Chen. Nonlinear gyrokinetic equations for low-frequency electromagnetic waves in general plasma equilibria. *Physics of Fluids*, 25(1982):502–508, 1982.

[101] G. Hammett and F. Perkins. Fluid moment models for Landau damping with application to the ion-temperature-gradient instability. *Physical Review Letters*, 64(25):3019–3022, 1990.

[102] B. Scott. Drift wave versus interchange turbulence in tokamak geometry: Linear versus nonlinear mode structure. *Physics of Plasmas*, 12(6):062314, 2005.

[103] A. N. Simakov and P. J. Catto. Drift-ordered fluid equations for modelling collisional edge plasma. *Contributions to Plasma Physics*, 44(1):83–94, 2004.

[104] R. Pasqualotto, P. Nielsen, C. Gowers, M. Beurskens, M. Kempenaars, T. Carlstrom, D. Johnson, and JET-EFDA Contributors. High resolution thomson scattering for joint european torus (jet). *Review of Scientific Instruments*, 75(10), 2004.

[105] D. L. Brower, W. A. Peebles, N. C. Luhmann, and R. L. Savage. Multichannel Scattering Studies of the Spectra and Spatial Distribution of Tokamak Microturbulence. *Physical Review Letters*, 54(7):689–692, 1985.

[106] B. Scott. Self-Sustained Collisional Drift-Wave Turbulence in a Sheared Magnetic Field. *Physical Review Letters*, 65(26), 1990.

[107] P. Saugaut. Large-eddy simulation: state-of-the-art. presented at GTP workshop. Boulder, Colorado., 2013.

[108] G. Erlebacher, M. Y. Hussaini, C. G. Speziale, and T. A. Zang. Toward the large-eddy simulation of compressible turbulent flows. *Journal of Fluid Mechanics*, 238:155–185, 1992.

[109] B. Galperin and S. Orszag. *Large eddy simulation of complex engineering and geophysical flows.* Cambridge University Press, 1993.

[110] C. Meneveau and P. Sagaut. *Large Eddy Simulation for Incompressible Flows: An Introduction.* Scientific Computation. Springer Berlin Heidelberg, 2006.

[111] J. Smagorinsky. General Circulation Experiments with the Primitive Equations. *Monthly Weather Review*, 91(3), 1963.

[112] S. A. Smith and G. W. Hammett. Eddy viscosity and hyperviscosity in spectral simulations of 2D drift wave turbulence. *Physics of Plasmas*, 4(4):978, 1997.

[113] M. Germano, U. Piomelli, P. Moin, and W. Cabot. A dynamic subgrid scale eddy viscosity model. 1760(1991), 2015.

[114] P. Morel, A. Banon Navarro, M. Albrecht-Marc, D. Carati, F. Merz, T. Gorler, and F. Jenko. Gyrokinetic large eddy simulations. *Physics of Plasmas*, 18(7):072301, 2011.

[115] S. Ghosal, T. S. Lund, P. Moin, and K. Akselvoll. A dynamic localization model for large-eddy simulation of turbulent flows. *Journal of Fluid Mechanics*, 297:402, 1995.

[116] S. Stolz and N. A. Adams. An approximate deconvolution procedure for large-eddy simulation. *Physics of Fluids*, 11(1999):1699–1701, 1999.

[117] T. Hughes, L. Mazzei, and K. Jansen. Large Eddy Simulation and the variational multiscale method. *Computing and Visualization in Science*, 3:47–59, 2000.

[118] M. Wakatani and A. Hasegawa. A collisional drift wave description of plasma edge turbulence. *Physics of Fluids*, 27(3):611, 1984.

[119] R. Numata. Bifurcation in Resistive Drift Wave Turbulence. 2007.

[120] S. Sukoriansky and A. Chekhlov. Large eddy simulation of two-dimensional isotrpic turbulence. 1976.

[121] A. Yoshizawa, S. Itoh, K. Itoh, and N. Yokoi. Turbulence theories and modelling of fluids and plasmas. *Plasma Physics and Controlled Fusion*, 43(3):R1–R144, March 2001.

[122] K. Chung and R. Bengtson. Simultaneous measurement of viscosity and flow velocity in Texas Experimental Tokamak-Upgrade (TEXT-U) edge plasmas by using a Visco-Mach probe. *Physics of Plasmas*, 4(8):2928, 1997.

[123] A. Savitzky and M. J. E. Golay. (36).

[124] G. Boffetta, A. Celani, and M. Vergassola. Inverse energy cascade in two-dimensional turbulence: Deviations from Gaussian behavior. *Physical Review E*, 61(1):R29–R32, 2000.

[125] W. Haeseleer et al. *Flux coordinates and magnetic field structure: a guide to a fundamental tool of plasma structure.* Springer-Verlag, 1991.

[126] B. Dudson, D. Dickinson, L. Easy, P. Hill, J. Madsen, and J. Omotani. Verification of bout++ using the method of manufactured solutions. In *BOUT++ Workshop 2015*, 2015.

[127] L.L. Lao, H. John, R.D. Stambaugh, A.G. Kellman, and W. Pfeiffer. Reconstruction of current profile parameters and plasma shapes in tokamaks. *Nuclear Fusion*, 25(11):1611–1622, 1985.

[128] J. Loizu, P. Ricci, F. D. Halpern, and S. Jolliet. Boundary conditions for plasma fluid models at the magnetic presheath entrance. *Physics of Plasmas*, 19(2012), 2012.

[129] S. Togo, M. Nakamura, Y. Ogawa, and K. Shimizu. Effects of Neutral Particles on the Stability of the Detachment Fronts in Divertor Plasmas. *The Japan Society of Plasma Science and Nuclear Fusion Research*, 8:1–4, 2013.

[130] F. F. Abraham, J. Q. Broughton, and E. Kaxiras. Spanning the length scales in dynamic simulation. *Computational Physics*, 12(6):538–546, 1998.

[131] S. Usami, R. Horiuchi, H. Ohtani, and M. Den. Development of multi-hierarchy simulation model with non-uniform space grids for collisionless driven reconnection. *Physics of Plasmas*, 20(2013), 2013.

[132] W. Press, S. Teukolsky, W. Vetterling, and B. Flannery. *Numerical Recipes 3rd Edition: The Art of Scientific Computing*. Cambridge University Press, New York, NY, USA, 3 edition, 2007.

[133] S. Usami, H. Ohtani, and R. Horiuchi. Development of Multi-hierarchy Simulation Model for Studies of Magnetic Reconnection y x. *Communications in Computational Physics*, 4(SEPTEMBER):537–544, 2008.

[134] P. B. Snyder, H. R. Wilson, J. R. Ferron, L. L. Lao, A. W. Leonard, T. H. Osborne, A. D. Turnbull, D. Mossessian, M. Murakami, and X. Q. Xu. Edge localized modes and the pedestal: A model based on coupled peeling ballooning modes. *Physics of Plasmas*, 9(5):2037, 2002.

[135] H. R. Wilson, P. B. Snyder, G. T. A. Huysmans, and R. L. Miller. Numerical studies of edge localized instabilities in tokamaks. *Physics of Plasmas*, 9(2002):1277, 2002.